The role of electronic correlations in scanning tunneling spectroscopy of adatoms

Dissertation

zur Erlangung des Doktorgrades der Naturwissenschaften
(Dr. rer. nat.)

der

Naturwissenschaftlichen Fakultät II
Chemie, Physik und Mathematik

der Martin-Luther-Universität
Halle-Wittenberg

vorgelegt von

Herrn Sebastian Frank
geb. am 01.01.1986 in Eisenach

Gutachter
Prof. Dr. Eberhard K. U. Gross
Prof. Dr. Giorgio Sangiovanni
Prof. Dr. Ingrid Mertig

Verteidigung am 08.06.2020

Contents

1 Introduction

In the past decades, electronic devices have become cheaper, more widespread and influence increasingly more aspects of people's lives. This has only been made possible due to constant technological progress in the field of electronics. Moore's law states that the number of transistors that can be fit on a piece of silicon grows exponentially[1], although the speed of growth has recently been slowing down[2]. The ultimate step of miniaturization is the atomic limit, where single atoms or molecules are used as building blocks for electronic circuits. This is often referred to as molecular electronics[3]. Many single-molecule or single-atom devices have already been realized in the laboratory[4;5], like wires[6], switches[7;8], transistors[9;10] and rectifiers[11;12;13], and the goal is to create complete circuits based on atoms and molecules[14]. The advantages are evident: the smaller size leads to lower material and power consumption and allows the fabrication of smaller and faster devices. Due to the small size, quantum effects are dominant, and a wealth of quantum phenomena such as quantum interference[15;16;17] and conductance quantization[18;19] can be observed. The additional spin degree of freedom also allows the development of exciting spintronic applications[20], like the magnetoresistive random access memory (MRAM)[21], which combines the speed of the charge-based conventional RAM and the non-volatility of conventional magnetic storage devices. If these quantum phenomena can be reliably controlled, they open up a wealth of possibilities for the development of new molecular devices.

On the other hand, the small scale introduces additional complications. The fabrication of structures on the nanoscale becomes increasingly more complex and requires more advanced machinery, leading to more expensive production facilities[22]. While individual components have already been realized on the molecular scale, their combination is far from trivial. When contacting molecules, the exact contact geometry can play a very crucial role on the local electronic structure and the resulting transport properties[23], particularly when connecting molecules to metallic electrodes[23]. One possible solution for the creation of supramolecular structures might be self-assembly[24;25]. Furthermore, the theoretical description of molecular electronics is also considerably more complex than that of classical circuits.

A milestone in the understanding of atomic and molecular systems was the invention of scanning tunneling microscopy (STM). It was originally invented by Binnig and Rohrer[26], who were awarded the Nobel prize in physics in 1986[27]. A metallic tip is placed on top of a surface, a voltage applied and the tunneling current measured. The latter depends exponentially on the distance of tip and surface, making it possible to directly probe the topographic structure of surfaces with atomic resolution. An extension of STM is scanning tunneling spectroscopy (STS)[28], which will be a central focus of this work. In STS, the STM tip is typically kept static at a specific location of the sample and the applied voltage is varied. The slope of the acquired current curve is directly proportional to the density of states of the probed material. The development of STM and STS opened up unprecedented possibilities in the area of surface science: they make it possible to study individual atoms and molecules placed on top of a surface, and directly probe their local electronic structure. This also made it possible for the first time to locally measure the Kondo effect, which was achieved by Li *et al.*[29] and Madhavan *et al.*[30] in 1998. Since then, STS has become a standard tool to probe the Kondo effect of magnetic atoms and molecules placed on top of metallic substrates[31;32;33;34;35;36;37;38].

The Kondo effect was first observed during resistivity measurements of non-magnetic metals with magnetic impurities[39;40]. At low temperatures, an unexpected increase in resistance was observed. This was later explained by Jun Kondo[41] to be caused by an an antiferromagnetic coupling between the impurity spin and the surrounding conduction electrons, leading to the formation of the Kondo state, which acts as an additional scatterer at low temperatures.

The Kondo effect can be seen as an effect of so-called strong electronic correlation, which refers to systems where the Coulomb interaction is strong, and can typically not be theoretically treated with conventional mean-field methods. A typical example are the unfilled d and f shells of transition metals and lanthanides, respectively. Due to their higher localization, the electrons in these orbitals are more confined and the Coulomb interaction is strong. The phenomenon of strong electronic correlation is not exclusive to metals, and can for example also occur in conjugated organic systems[42]. It can lead to many other fascinating phenomena[43], for instance in Mott-Hubbard insulators[44;45], heavy fermion materials[46] and high-temperature superconductors[47;48;49].

Recent technologies facilitated the study of the Kondo effect in many other nanosystems, for instance in quantum dots[50;51], in carbon nanotubes[52;53], in break-junction experiments[54], and, as mentioned before, in the context of STS. Increasingly more complex situations can be investigated: the Kondo effect in multimers on surfaces[55], in organometallic molecules[37;56], the interplay of Kondo effect and magnetic anisotropy[57] and the Kondo effect in topological insulators[58;59;60].

At the same time, there were considerable advances in the theoretical description of correlated systems, where particularly the combination of density functional theory (DFT) and dynamical mean field theory (DMFT) stands out[61], which made it possible to study strong electronic correlations in real materials.

This thesis focuses on the theoretical description of electronic transport in an STS situation when strong electronic correlations are present, and will combine DFT and the one crossing approximation (OCA) impurity solver. The system of choice is a single magnetic Co atom placed on a non-magnetic Cu(001) or Cu(111) surface, respectively, probed by a Cu STM tip. This system was chosen for two reasons: firstly, it is relatively simple. Strong electronic correlations are present only in the d shell of the Co atom, while the rest of the system can be well described on a mean-field level. At low temperatures, the Kondo effect is the dominant feature, and there are no competing effect on the same energy scale, making it an ideal system to systematically study. Secondly, the system has been studied extensively in the past[32;38;62;63;64;65;66;67;68;69;70], and a wealth of experimental and theoretical results are readily available, making it an ideal testbed to study novel theoretical and computational methods.

This thesis is organized as follows: first, chapter 2 introduces the methods and theoretical concepts used throughout, namely DFT, Green's function based electron transport, the Landauer formalism, the Kondo effect and the Anderson impurity model (AIM). In chapter 3, the relation between the symmetry of the orbital containing the sharp Kondo resonance and the resulting line shape will be systematically studied. To this end, individual d orbitals are correlated and the corresponding transport properties calculated. Chapter 4 focuses on the computation of the partially screened Coulomb interaction U. To this end, the constrained random phase approximation (cRPA) will be introduced, and the effect of different DFT functionals and differently sized polarization regions will be studied. Possible extensions to the RPA in order to increase the size of the polarization region are presented. In chapter 5, the complete d shell of the Co adatom will be correlated, and the correlated transmission computed. This will be done on different levels of self-consistency, starting with a one-shot calculation, and proceeding to include the charge feedback and lastly the computation of U in the self-consistency cycle. The final chapter 6 concludes this work with a final discussion of the results and gives perspectives and ideas how this work can be extended in the future.

2 Theoretical background

The quantum-mechanical many-body problem is exceedingly complicated, and its solution requires the use of various strategies and approximations. The starting point is the many-body Schrödinger equation[71], here in its time-independent formulation:

$$\begin{aligned}\hat{H}\Psi(\vec{x}_1,...,\vec{x}_N) &= E\,\Psi(\vec{x}_1,...,\vec{x}_N)\\ (\hat{T}+\hat{U}+\hat{V})\Psi(\vec{x}_1,...,\vec{x}_N) &= E\,\Psi(\vec{x}_1,...,\vec{x}_N)\\ \left(-\frac{\hbar^2}{2m}\sum_{i=1}^{N}\nabla_i^2+\frac{1}{2}\sum_{\substack{i,j=1\\ i\neq j}}^{N}\frac{e^2}{|\vec{r}_1-\vec{r}_2|}-\sum_{i=1}^{N}\sum_{k=1}^{N_k}\frac{Z_k e^2}{|\vec{r}_i-\vec{R}_k|}\right)\Psi(\vec{x}_1,...,\vec{x}_N) &= E\,\Psi(\vec{x}_1,...,\vec{x}_N),\end{aligned} \tag{1}$$

where the many-body wave function Ψ depends on the spatial and spin coordinates $\vec{x}_i = (\vec{r}_i, \sigma_i)$ of all electrons, and E is the total energy. The many-body Hamiltonian $\hat{H}$ consists of the kinetic energy $\hat{T}$, electron-electron interaction $\hat{U}$ and electron-nuclei interaction $\hat{V}$. Equation 1 uses the Born-Oppenheimer approximation[72], which separates the motion of electrons and the much heavier nuclei. The nuclear coordinates R_k enter the wave function Ψ, energy E and all other observables only parametrically. This assumption will be used and be valid for all situations considered in this work.

Various methods to approximately solve the many-body problem have emerged, and are usually a compromise between accuracy and computational feasibility, where the choice of method heavily depends on the size of the system and the type of physical effect which is investigated. In this thesis, the system in question is a typical scanning tunneling microscope (STM) setup: a magnetic adatom is placed on a non-magnetic surface. A non-magnetic STM tip is placed on top of the surface (see Fig. 1).

In order to describe this system, a combination of various methods is necessary, which will be introduced in the following sections. First, the electronic structure of this infinite, non-periodic system will be determined on a mean-field level, making use of DFT, the Green's function (GF) formalism and the partitioning of the system into device and lead regions. Afterwards, the Landauer theory of transport will be introduced. The subsequent section is devoted to the Anderson impurity model in order to describe strong electronic correlations and Kondo physics, which cannot be treated by conventional perturbation theory.

2.1 Density functional theory

The many-body wave function Ψ from Eq. 1 is a mathematically complex quantity, depending on the spatial and spin coordinates $\vec{x}_i = (\vec{r}_i, \sigma_i)$ of all electrons. One is typically interested in quantities of less variables, like the one-body electron density $n(\vec{r})$ and pair correlation functions $g(\vec{r}, \vec{r}')$, which can be obtained by integration or summation of all other coordinates. The one-electron spin density $n_\sigma(\vec{r})$ can for example be obtained by integration of the squared

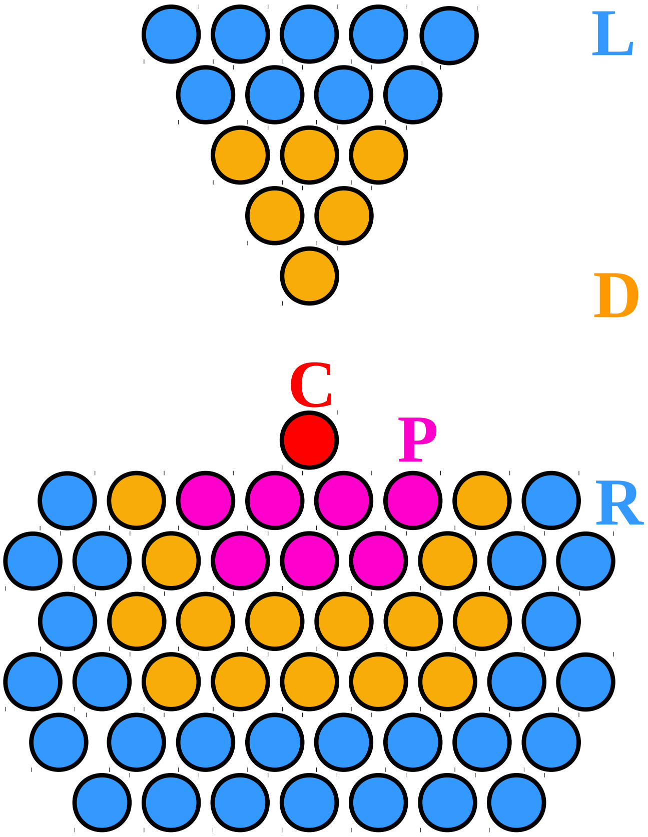

Figure 1: Schematic of the investigated system. An atom is placed on top of a metal surface, and an STM tip is placed directly above the adatom. The adatom contains correlated levels C, in this case due to a partially filled $3d$ shell. The device region is labeled D. It is connected to the semi-infinite leads L and R. The polarization region P will be used to compute the screened Coulomb interaction.

many-body wave function Ψ:

$$n_\sigma(\vec{r}) = N_\sigma \sum_{\sigma_2 \ldots \sigma N} \int \mathrm{d}^3 r_2 \ldots \mathrm{d}^3 r_N \, |\Psi(\vec{x}, \vec{x}_2, \ldots \vec{x}_N)|^2. \tag{2}$$

The total electron density $n(\vec{r})$ is the sum of the spin densities:

$$n(\vec{r}) = \sum_{\sigma=\uparrow,\downarrow} n_\sigma(\vec{r}). \tag{3}$$

The electron density is much easier to grasp than the many-body wave function, particularly for big systems with many electrons. An electronic structure theory based on the electron density $n(\vec{r})$ instead of the wave function Ψ as its central variable is therefore highly desirable. First attempts were made by Thomas and Fermi in 1927[73;74] shortly after the initial publication of the Schrödinger equation. Although their theory manages to describe certain qualitative trends, for instance for the total energy of atoms, it is incapable of treating valence electrons and does not lead to a chemical bond[75].

2.1.1 The Hohenberg-Kohn theorems

The Hohenberg-Kohn theorems provide the mathematical foundation of modern density functional theory, and were proposed and proven by Pierre Hohenberg and Walter Kohn in 1964[76]:

1. *The full many-particle non-degenerate ground state is a unique functional of the electron density* $n(\vec{r})$*.*

2. *The exact ground state density* $n(\vec{r})$ *minimizes the total energy functional.*

Additional proves have been put forward, for instance by Levy and Lieb[77;78]. The Hohenberg-Kohn theorems show that the many-body wave function can be written as a functional of the electron density,

$$\Psi = \Psi[n], \tag{4}$$

and therefore all other observables, especially the total energy, also become functionals of the electron density:

$$E[n] = \langle \Psi[n] | \hat{H} | \Psi[n] \rangle = \langle \Psi[n] | \hat{T} + \hat{U} + \hat{V} | \Psi[n] \rangle = T[n] + U[n] + V[n]. \tag{5}$$

The Hohenberg-Kohn-theorem has since been extended for many other situations, for example non-degenerate ground states[79], spin-dependency[80;81] and time-dependent systems[82]. While the Hohenberg-Kohn theory proves the existence of the one-to-one mapping between electron density and many-body wave function, it does not make any statement about how this mapping can be obtained. A direct variation of Eq. 5 with respect to the density is not possible, since the functional form of $T[n]$ and $U[n]$ is not known. The following section presents a practical scheme to determine total energy and electron density.

2.1.2 The Kohn-Sham equations

The Kohn-Sham (KS) equations go back to Walter Kohn and Lu Jeu Sham[83]. The formulation including spin of Ref. [80] will be used. The basic idea is to map the fully interacting system onto a system of non-interacting electrons, where the non-interacting system is chosen in a way to yield the same electron density as the interacting system. To that end, a fictitious system of non-interacting electrons with spin σ is defined, which move within KS potentials v_σ^{KS} and obey the one-body Schrödinger equation:

$$\left(-\frac{\hbar^2}{2m}\nabla^2 + v_\sigma^{\mathrm{KS}}(\vec{r})\right)\phi_{i\sigma} = \epsilon_{i\sigma}\phi_{i\sigma}, \tag{6}$$

where $\phi_{i\sigma}$ are KS orbitals and $\epsilon_{i\sigma}$ the corresponding KS eigenvalues. The KS potentials have to be chosen such that the electron density of the non-interacting fictitious system equals the electron density of the full interacting system. The density is then obtained by summation over the KS orbitals:

$$n(\vec{r}) = \sum_{\uparrow,\downarrow}\sum_{i=1}^{N_\sigma} |\phi_{i\sigma}(\vec{r})|^2. \tag{7}$$

In the following, a connection between the non-interacting KS system and the fully interacting system is established. To that end, we re-write the total energy of the full system as:

$$E = -\frac{\hbar^2}{2m}\sum_{\uparrow,\downarrow}\sum_{i=1}^{N_\sigma}\langle\phi_{i\sigma}|\nabla^2|\phi_{i\sigma}\rangle + \frac{e^2}{2}\int\int \mathrm{d}^3r\,\mathrm{d}^3r'\,\frac{n(\vec{r})n(\vec{r}')}{|\vec{r}-\vec{r}'|} + \int \mathrm{d}^3r\,n(\vec{r})v(\vec{r}) + E_{\mathrm{xc}}[n_\uparrow, n_\downarrow]. \tag{8}$$

The first term is the kinetic energy of a system of non-interacting electrons, the second term the classic Coulomb interaction of two charge distributions, also known as the Hartree term, and the third term the interaction between the electrons and the atomic cores. The quantity $E_{\mathrm{xc}}[n_\uparrow, n_\downarrow]$ is the so-called exchange-correlation potential and contains all missing physical effects,

$$\begin{aligned} E_{\mathrm{xc}}[n_\uparrow, n_\downarrow] = \quad & T[n_\uparrow, n_\downarrow] + \frac{\hbar^2}{2m}\sum_{\sigma=\uparrow,\downarrow}\sum_{i=1}^{N_\sigma}\langle\phi_{i\sigma}|\nabla^2|\phi_{i\sigma}\rangle \\ & + U[n_\uparrow, n_\downarrow] - \frac{e^2}{2}\int\int \mathrm{d}^3r\,\mathrm{d}^3r'\,\frac{n(\vec{r})n(\vec{r}')}{|\vec{r}-\vec{r}'|}, \end{aligned} \tag{9}$$

namely the exchange interaction due to the Pauli exclusion principle and the electron correlation. The Hohenberg-Kohn variational principle can now be applied to Eq. 8, by directly applying the functional derivative with respect to the electron density $n(\vec{r})$. By comparison with the fictitious, non-interacting system of Eq. 6, the KS potentials can be determined:

$$v_\sigma^{\mathrm{KS}}(\vec{r}) = v(\vec{r}) + v_{\mathrm{H}}(\vec{r}) + v_{\mathrm{xc},\sigma}[n_\uparrow, n_\downarrow](\vec{r}). \tag{10}$$

The KS potentials $v_\sigma^{\mathrm{KS}}(\vec{r})$ consist of the atomic core potential $v(\vec{r})$, the Hartree potential $v_{\mathrm{H}} = \int d^3r'\frac{n(\vec{r}')}{|\vec{r}-\vec{r}'|}$ and the exchange-correlation potential $v_{\mathrm{xc},\sigma}$. The latter is defined as the functional derivative of the exchange correlation energy $E_{\mathrm{xc}}[n_\uparrow, n_\downarrow]$ with respect to the respective spin density $n_\sigma(\vec{r})$:

$$v_{\mathrm{xc},\sigma}([n_\uparrow, n_\downarrow], \vec{r}) = \frac{\delta E_{\mathrm{xc}}[n_\uparrow, n_\downarrow]}{\delta n_\sigma(\vec{r})}. \tag{11}$$

All many-body effects, and the full complexity of the many-body Schrödinger equation, are contained within the local, multiplicative exchange correlation potential $v_{\mathrm{xc},\sigma}[n_\uparrow, n_\downarrow](\vec{r})$, whose exact form is unknown. For practical applications, approximate forms of the exchange-correlation energy $E_{\mathrm{xc}}[n_\uparrow, n_\downarrow]$ have to be found and the corresponding $v_{\mathrm{xc},\sigma}[n_\uparrow, n_\downarrow](\vec{r})$ have to be determined. The next chapter will discuss possible approximations for the exchange-correlation energy.

2.1.3 Exchange-correlation functionals

The local spin density approximation: The simplest approximation of $E_{\mathrm{xc}}[n_\uparrow, n_\downarrow]$ is the local spin density approximation (LSDA), and its non-spin polarized version, the local density approximation (LDA). It was first proposed by Kohn and Sham in Ref. [83]. The LSDA assumes that the exchange-correlation energy per particle at point $\vec{r}$ is given by that of a homogeneous electron gas with the same density as the local density $n(\vec{r})$. E_{xc} is then obtained by integration:

$$E_{\mathrm{xc}}^{\mathrm{LSDA}}[n_\uparrow, n_\downarrow] = \int \mathrm{d}^3 r \, n(\vec{r}) \epsilon_{\mathrm{xc}}(n_\uparrow(\vec{r}), n_\downarrow(\vec{r})). \tag{12}$$

The exchange-electron energy per particle $\epsilon_{\mathrm{xc}}(n_\uparrow(\vec{r}), n_\downarrow(\vec{r}))$ does not have a functional dependence of the spin densities, just from their value at location $\vec{r}$, which is a considerable simplification. The exchange component $\epsilon_x(n_\uparrow, n_\downarrow)$ can be computed analytically,

$$\epsilon_{\mathrm{x}}(n_\uparrow, n_\downarrow) = -\frac{3e^2}{4\pi}(6\pi^2)^{\frac{1}{3}} \frac{1}{n}(n_\uparrow^{\frac{4}{3}} + n_\downarrow^{\frac{4}{3}}), \tag{13}$$

while the correlation component $\epsilon_c(n_\uparrow, n_\downarrow)$ can be determined from Monte-Carlo simulations[84]. In this work, the Slater-Vosko-Wilk-Nusair (SVWN) parametrization of the LSDA[85;86] will be used. Albeit simple, the LSDA has been very successful, remarkably accurate and is still widely used in solid state physics. Its success can be attributed to the fact that it does obey certain sum rules and scaling properties[87]. It is exact for a uniform density and almost exact for slowly varying densities, and therefore yields an accurate description of simple crystalline metals. It does fail in the description of strongly correlated systems, for instance for strongly localized d and f electrons, and in the description of non-local phenomena like charge-transfer excitations and polarizabilities[88], which can be traced back to the self-interaction error and the lack of a derivative discontinuity.

Generalized gradient approximations: Generalized gradient approximations (GGAs) improve on the LSDA by including gradient corrections to the exchange-correlation energy,

$$E_{\mathrm{xc}}^{\mathrm{GGA}}[n_\uparrow, n_\downarrow] = \int d^3 r \, f\left(n_\uparrow(\vec{r}), n_\downarrow(\vec{r}), \vec{\nabla} n_\uparrow(\vec{r}), \vec{\nabla} n_\downarrow(\vec{r})\right), \tag{14}$$

where f is a function depending on the spin densities and their gradient, therefore incorporating non-local effects into E_{xc}. There are two basic approaches to determine the function f: it can be constructed in a way to fulfill as many exact conditions of E_{xc} as possible, as has been done for the PBE functional[89]. Alternatively, f can be determined empirically, by adjusting fit parameters such that the resulting functional yields reasonable results for a broad spectrum of test systems, like the BLYP functional[90;91].

GGA functionals typically outperform the LSDA when calculating binding lengths and dissociation energies, and also yield a more reliable description of the spin state of transition metals. GGAs still suffer from the same formal deficiencies as the LSDA and are therefore incapable of describing strongly localized and strongly non-local phenomena.

Note that a direct expansion of the LSDA, by adding a systematic correction for slowly-varying densities, has not been successful, because it is not directly derived from a physical system and does not fulfill certain exact properties of E_{xc} that the LSDA does fulfill[87].

KS DFT beyond LSDA and GGA: It is possible to include increasingly more non-local effects into E_{xc}, at increasingly higher costs. A way to judge the complexity of different approximations of E_{xc} is Jacob's ladder[92], which sorts DFT functionals into rungs. The lowest two rungs are the LSDA and GGAs, respectively. Meta-GGAs include terms containing occupied orbitals, hyper-GGAs the exact exchange energy density. The topmost rung are functionals containing effects of occupied and unoccupied orbitals. Here, the exact exchange functional, which fully removes the one-electron self interaction, has to be mentioned[88]. Note that KS DFT treats exact exchange very differently from the Hartree-Fock approximation (HFA), where an identical term occurs. While the HFA leads to a non-local potential, KS DFT requires the potential to be local, and it has to be obtained by using the Optimized Effective Potential (OEP) method[93;94].

Hybrid functionals and the generalized Kohn-Sham scheme: Higher-level DFT functionals of the previous paragraph usually come at a very high computational cost and are often not implemented in standard DFT codes. Hybrid functionals can be seen as a pragmatic approach to improve the description of the electronic structure of materials where local and semi-local functionals fail. The idea of a hybrid functional was first proposed in Ref. [95]. Motivated by the coupling constant integration[87], a functional is defined which mixes exact exchange with (semi-)local exchange, and adding (semi-)local correlation:

$$E_{\mathrm{xc}}^{hyb} = b\, E_{\mathrm{x}}^{\mathrm{exact}} + (1-b) E_{\mathrm{x}}^{\mathrm{sl}} + E_{\mathrm{c}}^{\mathrm{sl}}. \tag{15}$$

Hybrid functionals can be based on different semi-local functionals and have varying percentages b of exact exchange. Variations with three parameters have also been proposed[96]. The most notable ones are the one-parameter PBE0 functional[97;98], based on the PBE DFT functional with 25% of exact exchange, its range-separated version HSE[99], and the three-parameter

B3LYP functional[100], based on the BLYP DFT functional, mixed with 20% of exact exchange. The share of exact exchange b can be estimated from the adiabatic connection theorem, but is typically determined by fitting test data sets and strongly depends on the underlying semi-local functional[97;101].

The important difference to the orbital functionals mentioned in the previous paragraph is the treatment within the generalized Kohn-Sham (GKS) scheme[102]. In the GKS scheme, the exact exchange component is not treated within DFT (what would require the OEP method mentioned in the previous paragraph), but within Hartree-Fock theory, yielding the non-local Fock operator. While still covered by the Hohenberg-Kohn theorem, hybrid functionals are therefore outside of the realm of KS DFT, and assume an auxiliary system of interacting electrons which can be represented as a Slater determinant. Since both Hartree-Fock theory and DFT are typically included in electronic structure codes, hybrid functionals can be implemented with relative ease.

While Hybrid functionals partially remove the self-interaction error inherent in local and semi-local functionals, their success is mostly due to their treatment within the GKS scheme[88]. Although originally fitted to mostly organic systems, they can yield reasonable structural and optical properties of solid state systems as well, even for localized $4f$ electrons in CeO_2 and Ce_2O_3[103] and for $3d$ electrons in strongly correlated materials like NiO[104].

LDA+U: A typical deficiency of local and semi-local functionals lies in the treatment of strongly-localized orbitals, often associated with d and f electrons, present in transition metals and lanthanides. This can be traced back to the self-interaction error present in LSDA and typical GGAs and becomes particularly apparent in transition metal oxides like NiO, whose band gaps are severely underestimated[43]. The LDA+U approach[105;106;107;108] tackles this issue by explicitly adding a Hubbard-like correction term to those states where the pure DFT functional fails,

$$\mathcal{H}^U = \frac{1}{2} \sum_{\substack{i,j,k,l \\ \sigma,\sigma'}} U_{ik;jl} c^\dagger_{i\sigma} c^\dagger_{j\sigma'} c_{l\sigma'} c_{k\sigma} \tag{16}$$

where $c^\dagger_{i\sigma}$ and $c_{i\sigma}$ are creation and annihilation operators, respectively, and $U_{ik;jl}$ is an effective Coulomb interaction which already takes into account screening due to all non-localized orbitals. This effective interaction will be discussed in more detail in chapter 4. The introduction of the correction term leads to improved band gaps and the appearance of Hubbard bands[43], which cannot be captured with local and semi-local DFT functionals.

The originally proposed LDA+U scheme[105;106] uses a strongly simplified Coulomb interaction, only accounting for the averaged direct U and exchange J interactions:

$$E^U = \frac{U}{2} \sum_{i,j,\sigma} n_i^\sigma n_j^{-\sigma} + \frac{U-J}{2} \sum_{\substack{i,j,\sigma \\ i\neq j}} n_i^\sigma n_j^\sigma . \tag{17}$$

Different, more sophisticated, formulations of the LDA+U exist, taking into account more elements of the Coulomb interaction U, accounting for rotational covariance[107], and including a double-counting correction E^{DCC}, which subtracts the part of E^{U} already contained in E^{LDA}. The exact expression for E^{DCC} is not known and various approximations exist. The double-counting problem will be discussed in more detail in Sec. 2.4.

The total energy functional of the LDA+U then becomes

$$E^{LDA+U} = E^{LDA} + E^{U} - E^{DCC}. \tag{18}$$

Similar to the hybrid functionals of the previous paragraph, the LDA+U functional is orbital-dependent by virtue of the orbital occupations n_i^σ, and is not treated within conventional KS-DFT (requiring the aforementioned OEP method), but within the HFA. Note that while the method is often called LDA+U, it is typically based on the spin-dependent LSDA instead of the LDA. It can also be combined with semi-local GGA functionals and is then denoted GGA+U, or more general, DFT+U.

2.1.4 Interpreting KS orbitals

The KS eigenvalues $\epsilon_{i\sigma}$ and KS orbitals $\phi_{i\sigma}$ in Eq. 6 were introduced as auxiliary quantities in order to generate the spin densities. They do, however, carry some physical meaning themselves, although their interpretation is less straightforward than that of density and total energy[88]. The highest occupied molecular orbital (HOMO) can be assigned a rigorous physical meaning: it is the chemical potential of the system[109]. The other occupied KS orbitals can be assigned some physical meaning as well[110;111], but they have to be interpreted more carefully.

In practice, KS eigenvalues and KS orbitals are often used as if they were quasi-particle excitations. Although there is no rigorous justification to do so, this approach has been shown to yield accurate results for the exact exchange-correlation functional not too far away from the Fermi level[88]. Even local- and semi-local functionals can yield reliable eigenvalue spectra, particularly for systems with non-localized KS orbitals and therefore small one-electron self interaction. For the description of localized orbitals, functionals free of one-electron self interaction[112;113] and hybrid functionals treated within the GKS scheme[113] can provide a reliable eigenvalue spectrum. Although often used interchangeably, the relationship between localization and self-interaction is not straightforward[114].

The Kondo effect is due to localized electrons, and cannot be described by local and semi-local functionals, partially due to their lack of a derivative discontinuity[43]. Several approaches have been made to treat the Kondo effect within (TD)DFT[115;116;117]. This thesis follows another route, though: local and semi-local functionals describe the weakly correlated part of the system and serve as a starting point for more advanced calculations, employing model Hamiltonians. The effects of strong electronic correlation due to the partially filled d shell will be included later via a self-energy in the DFT-based transport calculation (see section 2.4).

2.2 Partitioning and Green's functions

2.2.1 One-body non-interacting Green's functions

In this section, the concept of time-independent one-body Green's functions (GFs), which will be used frequently in this work, will be introduced[118]. In general, GFs are a mathematical tool to solve inhomogeneous, differential equations. In the context of quantum mechanics, the one-body GF operator $\hat{G}(z)$ is defined as

$$\left(z - \hat{H}\right)\hat{G}(z) = \hat{1}, \tag{19}$$

where $\hat{H}$ is a one-body Hamiltonian and z a complex number. The GF can be either directly inverted, or expressed in terms of the eigenvectors $|\phi_k\rangle$ and eigenvalues ϵ_k of the Hamiltonian,

$$\hat{G}^0(z) = (z - \hat{H})^{-1} = \sum_k \frac{|\phi_k\rangle\langle\phi_k|}{z - \epsilon_k}, \tag{20}$$

where $\hat{H}|\phi_k\rangle = \epsilon_k|\phi_k\rangle$. The GF has poles at the eigenvalues $z = \epsilon_k$ of the system along the real axis, or a branch cut for the continuous part of the eigenvalue spectrum. Due to that, in order to define a GF along the real axis, a limiting procedure is necessary. The retarded GF (also called resolvent operator) $\hat{G}^{0,R}(\omega)$, henceforth called $\hat{G}^0(\omega)$, is defined as:

$$\hat{G}^0(\omega) = \lim_{\eta\to 0}\left(\omega + \mathrm{i}\eta - \hat{H}\right)^{-1}. \tag{21}$$

The corresponding advanced Green's function can be obtained by Hermitian conjugation, approaching the real axis from below:

$$\hat{G}^{0A}(\omega) \equiv [\hat{G}^0(\omega)]^\dagger := \lim_{\eta\to 0}\left(\omega - \mathrm{i}\eta - \hat{H}\right)^{-1}. \tag{22}$$

The GF contains all information about the one-body system given by the one-body Hamiltonian $\hat{H}$, namely the eigenenergies (poles on the real axis) and eigenvectors (residues of the poles). The density of states can also be extracted directly from the GF:

$$\mathcal{D}(\omega) = -\frac{1}{\pi}\mathrm{Im}\left[\mathrm{Tr}[\hat{G}^0(\omega)]\right] \equiv \sum_k \delta(\omega - \epsilon_k). \tag{23}$$

For later use, we also define the spectral function $\hat{A}(\omega)$:

$$\hat{A}(\omega) := \mathrm{i}\left(\hat{G}^0(\omega) - \hat{G}^{0\dagger}(\omega)\right) = \sum_k \delta(\omega - \epsilon_k)|\phi_k\rangle\langle\phi_k|. \tag{24}$$

In this work $\hat{G}^0(\omega)$ will be computed by direct inversion of Eq. 20, which can be advantageous, since it does not require the explicit calculation of the eigenstates. This can be done in any basis set and for a fixed value of z. The starting point is the KS Hamiltonian (see notes on the use of KS orbitals in section 2.1.4). Note that this work uses Gaussian basis sets, which are non-orthogonal. This has to be taken into account, and will lead to modified equations including the overlap matrix S and modified operator representations[119]. Particular care has to be taken when projecting onto subspaces[70]. For the sake of clarity, the basis will be assumed to be orthogonal in the main text. The corresponding basic equations for a non-orthogonal basis sets are presented in Appendix B.

2.2.2 Many-body Green's functions

For later use, the concept of many-body Green's functions is presented in this section. Details about this concept can be found in many-body textbooks[120;121]. The single-particle many-body Green's functions, which are also called single-particle propagators, describe the elementary response of a many-body system[121]. They can be seen as a generalization of the one-body GF from the previous sections to the case of interacting electrons:

$$G_{\alpha\alpha'}(t,t') = -\left\langle \mathcal{T}_t[c_\alpha(t), c^\dagger_{\alpha'}(t)]\right\rangle, \tag{25}$$

where $\mathcal{T}_t$ is the time-ordering operator, c_α and $c^\dagger_{\alpha'}$ are annihilation and creation operators in the Heisenberg picture which obey the fermionic anti-commutation relation $\{c_\alpha, c^\dagger_{\alpha'}\} = \delta_{\alpha\alpha'}$. To study finite-temperature effects like the Kondo effect, the above concept can be easily generalized to finite temperatures. The quantum-mechanical partition function can be interpreted as the time-evolution operator in imaginary time[121]:

$$\mathrm{e}^{-\beta\hat{H}} = \hat{U}(-\mathrm{i}\hbar\beta), \tag{26}$$

with the time-evolution operator $\hat{U} = \mathrm{e}^{\frac{\mathrm{i}}{\hbar}\hat{H}t}$, $\beta = 1/k_BT$ and the Boltzmann constant k_B. The single-particle finite-temperature or Matsubara GF is then defined as:

$$G_{\alpha\alpha'}(\tau,\tau') = -\left\langle \mathcal{T}_\tau[c_\alpha(\tau), c^\dagger_{\alpha'}(\tau')]\right\rangle, \tag{27}$$

where $\mathcal{T}_\tau$ is the time-ordering operator in imaginary time τ. A Fourier transformation with respect to imaginary time τ of the Matsubara GF yields the Matsubara GF for imaginary frequencies:

$$G_{\alpha\alpha'}(\mathrm{i}\omega_n) = \int_0^\beta \mathrm{d}\tau\, \mathrm{e}^{\mathrm{i}\omega_n\tau} G_{\alpha\alpha'}(\tau,0). \tag{28}$$

Note that the finite range of integration (from 0 to β) leads to the discrete Matsubara frequencies

$$\begin{aligned} \nu_n &= \quad 2n \quad \pi k_BT \quad \text{bosons} \\ \omega_n &= (2n+1)\pi k_BT \quad \text{fermions,} \end{aligned} \tag{29}$$

and the inverse relation features a sum over the Matsubara frequencies instead of a continuous integral:

$$G_{\alpha\alpha'}(\tau) = \frac{1}{\beta}\sum_n G_{\alpha\alpha'}(\mathrm{i}\omega_n)\mathrm{e}^{-\mathrm{i}\omega_n\tau}. \tag{30}$$

The retarded single-particle GF $G^R_{\alpha\alpha'}(\omega)$ can be obtained from the Matsubara GF by analytical continuation:

$$G^R_{\alpha\alpha'}(\omega) \equiv G_{\alpha\alpha'}(\mathrm{i}\omega_n \to \omega + \mathrm{i}\eta). \tag{31}$$

The interacting Green's function reduces to the non-interacting Green's function in the absence of interactions, and they can be related to each other by the following Dyson equation:

$$G(\omega) = G^0(\omega) + G^0(\omega)\Sigma(\omega)G(\omega). \tag{32}$$

$\Sigma(\omega)$ is the irreducible self energy and contains the effects of strong electronic correlations which cannot be captured by standard KS-DFT. In this work, interactions beyond mean-field will be taken into account for the correlated subspace C only. More details on the computation of Σ_C can be found in Sec. 2.4.

2.2.3 Partitioning into leads and device

Since we are interested in the physics close to the nanojunction, here given by the STM tip and the adatom on the surface, and not the exact electronic structure deep inside the STM tip or the surface, it is convenient to separate the system into a central device region D, a left lead L (here: the STM tip) and a right lead R (here: the surface far away from the central region). Left and right lead are chosen sufficiently far apart so that their interaction can be assumed to be zero, and that the device contains sufficient portions of both leads. The device region is coupled to the respective leads by operators $\hat{V}_\mathrm{LD}$ and $\hat{V}_\mathrm{RD}$. From here on, operators will be replaced by their representation in a local basis $\mathbf{H} = \langle\alpha|\hat{H}|\beta\rangle$, which is assumed to be orthogonal in the main text. The Hamiltonian of the combined lead-device-lead system then is:

$$\mathbf{H} = \begin{pmatrix} \mathbf{H}_\mathrm{L} & \mathbf{V}_\mathrm{LD} & \mathbf{0}_\mathrm{LR} \\ \mathbf{V}_\mathrm{DL} & \mathbf{H}_\mathrm{D} & \mathbf{V}_\mathrm{DR} \\ \mathbf{0}_\mathrm{RL} & \mathbf{V}_\mathrm{RD} & \mathbf{H}_\mathrm{R} \end{pmatrix} . \tag{33}$$

Here, the previously introduced Green's function method serves as a powerful tool. Since interactions are not yet switched on, the non-interacting Green's function from Sec. 2.2.1 will be used. We write out Eq. 19 as a matrix equation, using the partitioned Hamiltonian from Eq. 33:

$$\begin{pmatrix} \omega - \mathbf{H}_\mathrm{L} & -\mathbf{V}_\mathrm{LD} & \mathbf{0}_\mathrm{LR} \\ -\mathbf{V}_\mathrm{DL} & \omega - \mathbf{H}_\mathrm{D} & -\mathbf{V}_\mathrm{DR} \\ \mathbf{0}_\mathrm{RL} & -\mathbf{V}_\mathrm{RD} & \omega - \mathbf{H}_\mathrm{R} \end{pmatrix} \begin{pmatrix} \mathbf{G}^0_\mathrm{L}(\omega) & \mathbf{G}^0_\mathrm{LD}(\omega) & \mathbf{G}^0_\mathrm{LR}(\omega) \\ \mathbf{G}^0_\mathrm{DL}(\omega) & \mathbf{G}^0_\mathrm{D}(\omega) & \mathbf{G}^0_\mathrm{DR}(\omega) \\ \mathbf{G}^0_\mathrm{RL}(\omega) & \mathbf{G}^0_\mathrm{RD}(\omega) & \mathbf{G}^0_\mathrm{R}(\omega) \end{pmatrix} = \begin{pmatrix} \mathbf{1} & \mathbf{0} & \mathbf{0} \\ \mathbf{0} & \mathbf{1} & \mathbf{0} \\ \mathbf{0} & \mathbf{0} & \mathbf{1} \end{pmatrix} . \tag{34}$$

This matrix equation can be solved for all components of the GF, but since most of the relevant physics happens inside of the device region, we only write out certain GF elements for the following derivations. The device GF $\mathbf{G}^0_\mathrm{D}(\omega)$ is

$$\begin{aligned} \mathbf{G}^0_\mathrm{D}(\omega) &= \left(\omega - \mathbf{H}_\mathrm{D} - \mathbf{V}_\mathrm{DL}\,(\omega - \mathbf{H}_\mathrm{L})^{-1}\,\mathbf{V}_\mathrm{LD} - \mathbf{V}_\mathrm{DR}\,(\omega - \mathbf{H}_\mathrm{R})^{-1}\,\mathbf{V}_\mathrm{RD}\right)^{-1} \\ &= \left(\omega - \mathbf{H}_\mathrm{D} - \mathbf{V}_\mathrm{DL} \quad \mathbf{g}^0_\mathrm{L}(\omega) \quad \mathbf{V}_\mathrm{LD} - \mathbf{V}_\mathrm{DR} \quad \mathbf{g}^0_\mathrm{R}(\omega) \quad \mathbf{V}_\mathrm{RD}\right)^{-1} \\ &= (\omega - \mathbf{H}_\mathrm{D} - \qquad \mathbf{\Sigma}_\mathrm{L}(\omega) \qquad - \qquad \mathbf{\Sigma}_\mathrm{R}(\omega) \qquad)^{-1} , \end{aligned} \tag{35}$$

where the GFs of the isolated leads $\mathbf{g}^0_\alpha = (\omega - \mathbf{H}_\alpha)^{-1}$ and the lead self energies $\mathbf{\Sigma}_\alpha = \mathbf{V}_{\mathrm{D}\alpha}\,\mathbf{g}^0_\alpha(\omega)\,\mathbf{V}_{\alpha\mathrm{D}}$ ($\alpha = \mathrm{L}, \mathrm{R}$) are introduced. $\mathbf{G}^0_\mathrm{D}(\omega)$ describes the electronic structure of the device region in the presence of the leads. The lead self energies $\mathbf{\Sigma}_\alpha(\omega)$ introduce an energy dependence, which reflects the fact that electrons do not have an infinite lifetime within the device region anymore, but can hop between device and leads. The matrix element $\mathbf{G}^0_{\mathrm{RD}}(\omega)$ will also be required later:

$$\mathbf{G}^0_{\mathrm{RD}}(\omega) = \mathbf{g}^0_{\mathrm{R}}(\omega)\mathbf{V}_{\mathrm{RD}}\mathbf{G}^0_{\mathrm{D}}(\omega). \tag{36}$$

Later in this work, the so-called coupling matrices will also be used:

$$\mathbf{\Gamma}_{\mathrm{L/R}}(\omega) := \mathrm{i}\left(\mathbf{\Sigma}_{\mathrm{L/R}} - \mathbf{\Sigma}^{\dagger}_{\mathrm{L/R}}(\omega)\right). \tag{37}$$

So far, we have not specified how to obtain the lead self energies $\mathbf{\Sigma}_{\mathrm{L/R}}$. In the system at hand, the structure of the macroscopic electrode far away from the central region is typically not known exactly. While some crystalline order will be present, the bulk electrodes are likely polycrystalline, and surface defects and impurities might also be present. Therefore a lead model is desirable which does not depend too strongly on the exact local structure, and provides a smooth lead density of states (DOS) similar to that of the bulk material.

A very simple lead model are jellium leads with a complex absorbing potential[122;123]. While computationally very cheap and providing a smooth lead DOS, they do not contain any information about the chemical composition of the lead and fail to provide important material properties, so that a distinction between different materials is not possible.

A more complex option are semi-infinite nanowire electrodes, whose electronic structure is determined from the supercell approach[124;125], typically within DFT and at the same level of approximation as the device region. However, perfectly crystalline nanowires with small cross sections have been shown to exhibit large fluctuations in transport properties, depending on lead size and orientation[126]. While nanowire electrodes are a powerful tool in the description of perfectly ordered systems like nanotubes, there are certain drawbacks for the type of system studied in this work, in addition to a relatively high computational cost[127]. In a similar spirit, the cluster can be embedded into a nanowire with infinite thickness[128]. While this does eliminate finite-size effects due to the finite thickness of the nanowire, it still assumes a perfectly ordered system and might still contain reflections on crystal planes, and is computationally demanding.

Another electrode model is a Bethe lattice[129], a tight-binding model with appropriately chosen coordination and parameters[127;130;131], which will be used in this work. It correctly captures the short-range order of the electrode, but neglects long-range order since it does not contain any closed loops. It gives a fairly accurate description of the bulk electrode DOS for commonly used metal leads, and has been studied and proven to work reasonably well in the modeling of transport situations[127;131]. Bethe lattice parameters are determined from DFT calculations[132] and have to be calculated once for each basis set. A detailed account of how to determine the Bethe lattice self energies can be found in Ref. [127]. It is important to include a large enough portion of the leads in the device, in order to make scattering at the interface between the Bethe lattice and the device region less important to the physics within the device region, since the Bethe lattice is treated at a lower level of accuracy than the device.

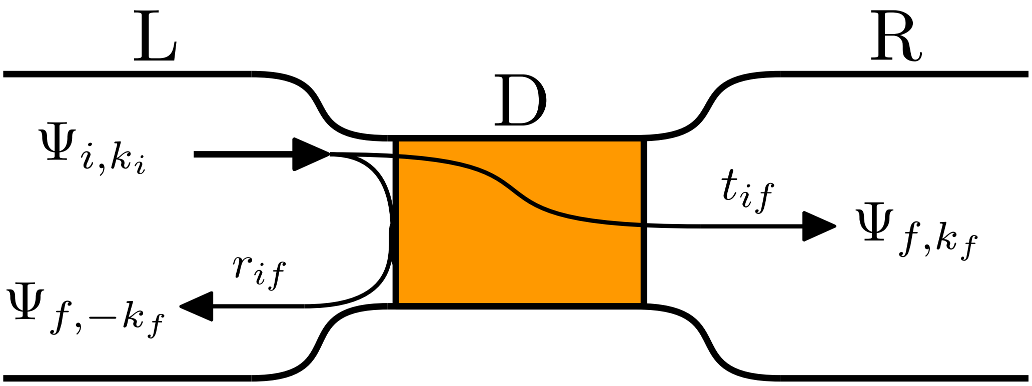

Figure 2: Basic illustration of the Landauer theory of transport. An incoming wave from the left lead Ψ_{i,k_i} is scattered at the device, and partially relfected and transmitted to final states $\Psi_{f,-k_f}$ and Ψ_{f,k_f} with reflection and transmission coefficients r_{if} and t_{if}, respectively.

So far, we reviewed on how to determine the electronic structure of the device on a mean-field level using DFT, introduced the Green's function formalism as a powerful mathematical tool, partitioned the system into a device region and two leads and discussed possible models to describe the macroscopic leads. However, so far we just described the electronic structure of the ground state and have not yet considered how to calculate transport properties like currents and conductances, which is central to the modeling of an STM setup. To that end, in the next section the Landauer theory of transport will be introduced.

2.3 Quantum transport within the Landauer formalism

The basic idea of the Landauer theory of transport[133;134;135] (later extended by M. Büttiker) is that electrons undergo an elastic scattering process when passing through the nanocontact. Landauer then relates the probability of the electron to be transmitted to the conductance of the system. A basic illustration of the Landauer formalism is shown in Fig. 2. A nanocontact D is sandwiched between two leads L and R, which are adiabatically connected to reflectionless reservoirs in thermal equilibrium, whose chemical potential is set to μ_L and μ_R, respectively. The reservoirs inject electrons into the leads with a local equilibrium distribution $f_{\mathrm{L/R}}(\omega)$, which typically is the Fermi-Dirac distribution:

$$f_{L/R}(\omega) = \frac{1}{\mathrm{e}^{(\omega-\mu_{L/R})/k_B T} + 1}. \tag{38}$$

The left reservoir injects right-moving and the right reservoir left-moving electrons into the corresponding leads, and left- and right-moving electrons are completely uncorrelated. Once injected, the electrons occupy independent channels characterized by a set of quantum numbers. Furthermore, the scattering process is assumed to be elastic, so the particle energy does not change, and coherent, such that all scattering is taking place at the nanocontact, and scattering due to lattice vibrations and other electrons can be neglected. This is a justifiable assumption if the dimensions of the nanocontact are smaller than the average coherence length of electrons in the material. Another assumption is that the system will reach an ideal steady state, and exactly one steady state solution exists.[136]

Due to their finite size, the leads limit the movement of electrons in the x-y plane, but they can propagate freely in the z direction (this condition can easily be extended to a potential periodic in the z direction, by introducing Bloch states). The corresponding Schrödinger equation deep inside the leads (here for the left lead) then is

$$\left[-\frac{\hbar^2}{2m}\nabla^2 + V_{\mathrm{L}}(\vec{r}_\perp)\right]\psi_{n,k} = E_n(k)\psi_{n,k}(\vec{r}), \tag{39}$$

where the potential $V_{\mathrm{L}}(\vec{r}_\perp)$ confines the electrons in the x-y direction. Eq.39 can be separated into a longitudinal part, describing a free particle in the z direction, and a transverse equation in the x-y plane. The general solution can then be written as

$$\psi_{n,k}(\vec{r}_\perp, z) = u_n(\vec{r}_\perp)\sqrt{\frac{1}{L_z}}\mathrm{e}^{\mathrm{i}kz}, \tag{40}$$

where $u_n(\vec{r}_\perp)$ is the solution of the transverse equation, n are all its respective quantum numbers, and L_z is a normalization length. The corresponding energies are

$$E_n(k) = \epsilon_n + \frac{\hbar^2 k^2}{2m}. \tag{41}$$

To each single particle energy ω there is a corresponding number of transport channels, given by the transverse modes, and this number is fixed for each energy[136]. We now assume that an electron from the left with an initial wavevector k_i and energy $\omega_i(k_i)$ is injected into the system and scattered at the nanojunction. While the processes close to the contact might be very complex, we can make statements about the situation deep inside the leads. Far inside of the right lead, the wave will be a linear combination of eigenstates of the right lead, with transmission coefficients $t_{if}(\omega)$:

$$\Psi^+_{i,k_i}(\vec{r}) \to \sum_{f=1}^{N^{\mathrm{R}}} t_{if}(\omega)\Psi_{f,k_f}(\vec{r}), \quad z \to +\infty. \tag{42}$$

The $+$-sign denotes that the electron has already been scattered. In the left lead, the wave function consists of the incident wave Ψ_{i,k_i} and electrons that were backscattered to the left. The latter are also eigenstates of the left lead, with reflection coefficients $r_{if}(\omega)$ and the opposite sign of the wavevector k_f:

$$\Psi^+_{i,k_i}(\vec{r}) \to \Psi_{i,k_i}(\vec{r}) + \sum_{f=1}^{N^{\mathrm{L}}} r_{if}(\omega)\Psi_{f,-k_f}(\vec{r}), \quad z \to -\infty. \tag{43}$$

We can now proceed to compute the current deep inside the leads, and start with the current density for a single scattered electron with initial state Ψ_{i,k_i},

$$j_{i,k_i}(\vec{r}) = \frac{\mathrm{i}\hbar}{2m}\left(\Psi^+_{i,k_i}(\vec{r})\frac{\partial[\Psi^+_{i,k_i}(\vec{r})]^*}{\partial z} - [\Psi^+_{i,k_i}(\vec{r})]^*\frac{\partial\Psi^+_{i,k_i}(\vec{r})}{\partial z}\right), \tag{44}$$

where transport only occurs in the z direction. To determine the current $I(\omega_i)$ due to a given initial state at energy ω_i, the corresponding current density has to be integrated over a surface perpendicular to the transport direction:

$$I(\omega_i) = e \int_{-\infty}^{\infty} \mathrm{d}x \int_{-\infty}^{\infty} \mathrm{d}y \, j_{i,k_i}(\vec{r}). \tag{45}$$

Since the system is assumed to be in a steady state, any x-y plane can be used, particularly a plane deep inside the left or deep inside the right lead, and both have to yield the same current. Carrying out the integration deep inside the left lead yields:

$$\begin{aligned} I_{\mathrm{L}}(\omega_i) &= \frac{\mathrm{i}e\hbar}{2m} \int_{-\infty}^{\infty} \mathrm{d}x \int_{-\infty}^{\infty} \mathrm{d}y \left(\Psi^{+}_{f,k_f}(\vec{r}) \frac{\partial [\Psi^{+}_{f,k_f}(\vec{r})]^*}{\partial z} - [\Psi^{+}_{f,k_f}(\vec{r})]^* \frac{\partial \Psi^{+}_{f,k_f}(\vec{r})}{\partial z} \right) \\ &= I_i(\omega_i) - \sum_{f=1}^{N_{\mathrm{L}}} |r_{if}|^2 |I_f(\omega_i)| \\ &= I_i(\omega_i) \left(1 - \sum_{f=1}^{N_{\mathrm{L}}} |r_{if}|^2 \frac{|I_f(\omega_i)|}{|I_i(\omega_i)|} \right) \\ &= I_i(\omega_i) \left(1 - \sum_{f=1}^{N_{\mathrm{L}}} R_{if}(\omega_i) \right), \end{aligned} \tag{46}$$

where we have defined the current due to the incident wave $I_i(\omega_i)$,

$$I_i(\omega_i) = \frac{\mathrm{i}e\hbar}{2m} \int_{-\infty}^{\infty} \mathrm{d}x \int_{-\infty}^{\infty} \mathrm{d}y \left(\Psi_{i,k_i}(\vec{r}) \frac{\partial [\Psi_{i,k_i}(\vec{r})]^*}{\partial z} - [\Psi_{i,k_i}(\vec{r})]^* \frac{\partial \Psi_{i,k_i}(\vec{r})}{\partial z} \right), \tag{47}$$

and correspondingly the currents reflected back into the left leads $I_f(\omega_i)$. In the simple case of electrons traveling freely in the z direction, the integration can be carried out and yields $I_{i/f}(\omega_i) = e\frac{\hbar k_{i/f}}{mL_z}$. The R_{if} are reflection probabilities for an incident wave Ψ_{i,k_i} to be reflected into Ψ_{f,k_f}. Correspondingly, we can carry out the integration in the right lead:

$$I_{\mathrm{R}}(\omega_i) = I_i(\omega_i) \sum_{f=1}^{N_{\mathrm{R}}} T_{if}(\omega_i), \tag{48}$$

with transmission probabilities $T_{if} = |t_{if}|^2 \frac{|I_f(\omega_i)|}{|I_i(\omega_i)|}$. Since the system has been assumed to reach a steady state, the currents deep inside the left and the right lead have to be identical, and the reflection and transmission probabilities can be related:

$$\sum_{f=1}^{N_{\mathrm{L}}} R_{if} + \sum_{f=1}^{N_{\mathrm{R}}} T_{if} = 1. \tag{49}$$

Eq. 49 states that the incident particle in state Ψ_{i,k_i} has to either be reflected, or transmitted. The same arguments hold true for a particle incident from the right, which is then partially backscattered into the right lead and partially transmitted into the left lead.

So far, the current due to a single incident electron was calculated. In order to obtain the total current, the currents have to be weighted by the density of states at the respective energy and summed up. The density of states in one dimension is given by $\mathcal{D}(\omega_i) = \frac{L_z}{2\pi}\frac{\mathrm{d}k_i}{\mathrm{d}\omega_i} = \frac{mL_z}{2\pi\hbar^2}\frac{1}{k_i}$, and thus the total current becomes:

$$\begin{aligned} I_{\mathrm{R}}^{total} &= \int_{-\infty}^{\mu_{\mathrm{L}}} \mathrm{d}\omega \sum_{i=1}^{N_{\mathrm{L}}} \mathcal{D}(\omega) I_{\mathrm{R}}(\omega_i) \\ &= \int_{-\infty}^{\mu_{\mathrm{L}}} \mathrm{d}\omega \sum_{i=1}^{N_{\mathrm{L}}}\sum_{f=1}^{N_{\mathrm{R}}} \mathcal{D}(\omega) I_i(\omega) T_{if}(\omega_i) \\ &= \frac{e}{h}\int_{-\infty}^{\mu_{\mathrm{L}}} \mathrm{d}\omega \sum_{i=1}^{N_{\mathrm{L}}}\sum_{f=1}^{N_{\mathrm{R}}} T_{if}(\omega_i) \\ &= \frac{e}{h}\int_{-\infty}^{\mu_{\mathrm{L}}} \mathrm{d}\omega\, \mathcal{T}(\omega), \end{aligned} \tag{50}$$

where in the last equation, the total transmission function $\mathcal{T}(\omega)$ is introduced.
The whole procedure can now be repeated for an electron coming from the right electrode and being scattered at the nanojunction, resulting in a current towards the left lead. The corresponding total current is

$$I_{\mathrm{L}} = \frac{e}{h}\int_{-\infty}^{\mu_{\mathrm{R}}} \mathrm{d}\omega\, \mathcal{T}(\omega), \tag{51}$$

with the same transmission function $\mathcal{T}(\omega)$ due to time-inversion invariance[136]. The total current is simply a sum of I_{L} and I_{R}, and non-zero only if a finite bias eV is present such that $\mu_{\mathrm{L}} \equiv \mu$ and $\mu_{\mathrm{R}} = \mu + eV$:

$$I(eV) = \frac{e}{h}\int_{\mu}^{\mu+eV} \mathrm{d}\omega\, \mathcal{T}(\omega). \tag{52}$$

The corresponding conduction is obtained by taking the derivative with respect to the voltage:

$$G(V) = \frac{\partial I}{\partial V} = \frac{e^2}{h}\mathcal{T}(eV) \tag{53}$$

We have now established a connection between the differential conductance of the system and its transmission properties. Note that $\frac{e^2}{h}$ is half the quantum of conductance $G_0 = \frac{2e^2}{h}$, because we are generally working with spin-dependent systems and the spin-degree of freedom is contained in the channel index n and has not been integrated out yet.

Transmission function: So far, we derived the Landauer formula, relating the system's conductance to the transmission properties by considering properties deep inside the leads. We have not yet made any statement about how the transmission properties can be obtained and expressed in terms of the electronic structure of the nanojunction. To that end, we proceed as follows: first, the total wave function Ψ due to an incoming wave from the left lead $\vec{\Psi}^i$ will be expressed in terms of the system's GF. Then, the density matrix $\mathbf{P}$ of the system is computed by summing up all possible incoming waves, giving us access to the total charge of the device region[137]. The total current is then obtained as the time derivative of the system's total charge.

The system's wave function can be expressed as a sum of the initial wave and the final wave after scattering of the particle:

$$\vec{\Psi} = \vec{\Psi}^i + \vec{\Psi}^f = \begin{pmatrix} \vec{\Psi}^i_\mathrm{L} \\ 0_\mathrm{D} \\ 0_\mathrm{R} \end{pmatrix} + \begin{pmatrix} \vec{\Psi}^f_\mathrm{L} \\ \vec{\Psi}^f_\mathrm{D} \\ \vec{\Psi}^f_\mathrm{R} \end{pmatrix}. \tag{54}$$

While the initial wave is non-zero only in the left lead, the scattered wave is expanded over the whole system. The total wave function Ψ obeys $\mathbf{H}\left(\vec{\Psi}^i + \vec{\Psi}^f\right) = \omega\left(\vec{\Psi}^i + \vec{\Psi}^f\right)$. By reordering and inserting the definition of the GF, one obtains

$$\begin{aligned} (\mathbf{H} - \omega)\,\vec{\Psi}^f &= (\omega - \mathbf{H})\,\vec{\Psi}^i \\ -[\mathbf{G}^0(\omega)]^{-1}\vec{\Psi}^f &= (\omega - \mathbf{H})\,\vec{\Psi}^i \\ \vec{\Psi}^f &= -\mathbf{G}^0(\omega)\,(\omega - \mathbf{H})\,\vec{\Psi}^i. \end{aligned} \tag{55}$$

Writing out the above equation , and taking into account that $\vec{\Psi}^i$ is, per definition, an eigenstate of the isolated left lead ($(\omega - \mathbf{H}_\mathrm{L})\vec{\Psi}^i_\mathrm{L} = 0$), one arrives at:

$$\begin{pmatrix} \vec{\Psi}^f_\mathrm{L} \\ \vec{\Psi}^f_\mathrm{D} \\ \vec{\Psi}^f_\mathrm{R} \end{pmatrix} = -\mathbf{G}^0(\omega) \begin{pmatrix} (\omega - \mathbf{H}_\mathrm{L})\,\vec{\Psi}^i_\mathrm{L} \\ -\mathbf{V}_\mathrm{DL}\vec{\Psi}^i_\mathrm{L} \\ \mathbf{0}_\mathrm{R} \end{pmatrix} = -\mathbf{G}^0(\omega) \begin{pmatrix} \mathbf{0}_\mathrm{L} \\ -\mathbf{V}_\mathrm{DL}\vec{\Psi}^i_\mathrm{L} \\ \mathbf{0}_\mathrm{R} \end{pmatrix} = \begin{pmatrix} \mathbf{G}^0_\mathrm{LD}(\omega) \\ \mathbf{G}^0_\mathrm{D}(\omega) \\ \mathbf{G}^0_\mathrm{RD}(\omega) \end{pmatrix} \mathbf{V}_\mathrm{DL}\vec{\Psi}^i_\mathrm{L}. \tag{56}$$

The next step is to express the density matrix $\mathbf{P}$ of the system in terms of its wave function $\vec{\Psi}$:

$$\begin{aligned} \mathbf{P} &= \sum_{i=1}^{N_\mathrm{L}} \sum_{k_i} f_\mathrm{L}(\omega_i(k_i))\vec{\Psi}_{i,k_i}\vec{\Psi}^\dagger_{i,k_i} \\ &= \int \mathrm{d}\omega\, f_\mathrm{L}(\omega) \sum_{i=1}^{N_\mathrm{L}} \sum_{k_i} \delta(\omega - \omega_i(k_i))\vec{\Psi}_{i,k_i}\vec{\Psi}^\dagger_{i,k_i}, \end{aligned} \tag{57}$$

where $f_\mathrm{L}(\omega_i(k_i))$ is the Fermi function of the left lead with chemical potential μ_L defined in Eq. 38, and $\vec{\Psi}_{i,k_i}$ is the wave function component of the system due to the initial state i with wave vector k_i. The current can then be determined as the derivative of the total charge of the device region:

$$I = \frac{\partial N_\mathrm{D}}{\partial t} = \mathrm{Tr}_\mathrm{D}\left[\frac{\partial \mathbf{P}}{\partial t}\right]. \tag{58}$$

It consists of two components, one between the left lead and the device I_L and one between the right lead and the device I_R, and the total current is given by $I = I_\mathrm{L} + I_\mathrm{R}$. In a steady-state situation (as has been assumed above), the total charge of the device region does not change, and exactly the same amount of electrons flows in from the left as flows out on the right, such that $\frac{\partial N_\mathrm{D}}{\partial t} = 0$, and correspondingly $I_\mathrm{L} = -I_\mathrm{R}$. It therefore suffices to determine either I_L or I_R.

Now the time-derivative is explicitly carried out, making use of the fact that $\vec{\Psi}_{i,k_i}$ is an eigenstate of the Hamiltonian $\mathbf{H}$:

$$
\begin{aligned}
I = \mathrm{Tr}_\mathrm{D}\left[\frac{\partial \mathbf{P}}{\partial t}\right] &= \int \mathrm{d}\omega\, f_\mathrm{L}(\omega) \sum_{i=1}^{N_\mathrm{L}} \sum_{k_i} \mathrm{Tr}_\mathrm{D}\left[\frac{\partial \vec{\Psi}_{i,k_i}}{\partial t}\left[\vec{\Psi}_{i,k_i}\right]^\dagger + \vec{\Psi}_{i,k_i}\left[\frac{\partial \vec{\Psi}_{i,k_i}}{\partial t}\right]^\dagger\right] \\
&= \int \mathrm{d}\omega\, f_\mathrm{L}(\omega) \sum_{i=1}^{N_\mathrm{L}} \sum_{k_i} \mathrm{Tr}_\mathrm{D}\left[\frac{1}{\mathrm{i}\hbar}\mathbf{H}\vec{\Psi}_{i,k_i}\left[\vec{\Psi}_{i,k_i}\right]^\dagger - \frac{1}{\mathrm{i}\hbar}\vec{\Psi}_{i,k_i}\left[\mathbf{H}\vec{\Psi}_{i,k_i}\right]^\dagger\right].
\end{aligned}
\tag{59}
$$

The trace can then be evaluated:

$$
\mathrm{Tr}_\mathrm{D}\left[\frac{1}{\mathrm{i}\hbar}\mathbf{H}\vec{\Psi}_{i,k_i}\left[\vec{\Psi}_{i,k_i}\right]^\dagger\right] = \frac{1}{\mathrm{i}\hbar}\mathrm{Tr}\left[\mathbf{V}_\mathrm{DL}[\vec{\Psi}_{i,k_i}]_\mathrm{L}[\vec{\Psi}_{i,k_i}]_\mathrm{D}^\dagger + \mathbf{H}_\mathrm{D}[\vec{\Psi}_{i,k_i}]_\mathrm{D}[\vec{\Psi}_{i,k_i}]_\mathrm{D}^\dagger + \mathbf{V}_\mathrm{DR}[\vec{\Psi}_{i,k_i}]_\mathrm{R}[\vec{\Psi}_{i,k_i}]_\mathrm{D}^\dagger\right]
\tag{60}
$$

$$
\mathrm{Tr}_\mathrm{D}\left[\vec{\Psi}_{i,k_i}\left[\vec{\Psi}_{i,k_i}\right]^\dagger\frac{1}{\mathrm{i}\hbar}\mathbf{H}\right] = \frac{1}{\mathrm{i}\hbar}\mathrm{Tr}\left[[\vec{\Psi}_{i,k_i}]_\mathrm{D}[\vec{\Psi}_{i,k_i}]_\mathrm{L}^\dagger\mathbf{V}_\mathrm{LD} + [\vec{\Psi}_{i,k_i}]_\mathrm{D}[\vec{\Psi}_{i,k_i}]_\mathrm{D}^\dagger\mathbf{H}_\mathrm{D} + [\vec{\Psi}_{i,k_i}]_\mathrm{D}[\vec{\Psi}_{i,k_i}]_\mathrm{R}^\dagger\mathbf{V}_\mathrm{RD}\right].
\tag{61}
$$

Since there is no source or sink potential within the device region, the device terms cancel out when adding up the two contributions. The remaining terms can be separated into currents at the L-D-interface I^L_{i,k_i} and currents at the D-R-interace I^R_{i,k_i}:

$$
I^\mathrm{L}_{i,k_i} = \frac{e}{\mathrm{i}\hbar}\mathrm{Tr}\left[\mathbf{V}_\mathrm{DL}[\vec{\Psi}_{i,k_i}]_\mathrm{L}[\vec{\Psi}_{i,k_i}]_\mathrm{D}^\dagger - [\vec{\Psi}_{i,k_i}]_\mathrm{D}[\vec{\Psi}_{i,k_i}]_\mathrm{L}^\dagger\mathbf{V}_\mathrm{LD}\right]
\tag{62}
$$

$$
I^\mathrm{R}_{i,k_i} = \frac{e}{\mathrm{i}\hbar}\mathrm{Tr}\left[\mathbf{V}_\mathrm{DR}[\vec{\Psi}_{i,k_i}]_\mathrm{R}[\vec{\Psi}_{i,k_i}]_\mathrm{D}^\dagger - [\vec{\Psi}_{i,k_i}]_\mathrm{D}[\vec{\Psi}_{i,k_i}]_\mathrm{R}^\dagger\mathbf{V}_\mathrm{RD}\right].
\tag{63}
$$

As stated above for the total current, and since channels are independent, either of these current components can be evaluated. We choose to evaluate I^R_{i,k_i}. To that end, we write the wave function $\vec{\Psi}_{i,k_i}$ in terms of the initial wave function $\vec{\Psi}^i_{i,k_i}$ according to Eq. 56, insert Eq. 36, Eq.37 and use the invariance of the trace to cyclic permutations:

$$
\begin{aligned}
I^\mathrm{R}_{i,k_i} &= \frac{e}{\mathrm{i}\hbar}\mathrm{Tr}\left[\mathbf{V}_\mathrm{DR}[\vec{\Psi}_{i,k_i}]_\mathrm{R}[\vec{\Psi}_{i,k_i}]_\mathrm{D}^\dagger + [\vec{\Psi}_{i,k_i}]_\mathrm{D}[\vec{\Psi}_{i,k_i}]_\mathrm{R}^\dagger\mathbf{V}_\mathrm{RD}\right] \\
&= \frac{e}{\mathrm{i}\hbar}\mathrm{Tr}\left[[\mathbf{G}^0_\mathrm{D}(\omega)]^\dagger\mathbf{V}_\mathrm{DR}\left(\mathbf{g}_\mathrm{R}(\omega) - \mathbf{g}^\dagger_\mathrm{R}(\omega)\right)\mathbf{V}_\mathrm{RD}\mathbf{G}^0_\mathrm{D}(\omega)\mathbf{V}_\mathrm{DL}\vec{\Psi}^i_{i,k_i}[\vec{\Psi}^i_{i,k_i}]^\dagger\mathbf{V}_\mathrm{LD}\right] \\
&= \frac{e}{\mathrm{i}\hbar}\mathrm{Tr}\left[[\mathbf{G}^0_\mathrm{D}(\omega)]^\dagger\left(-\mathrm{i}\mathbf{\Gamma}_\mathrm{R}(\omega)\right)\mathbf{G}^0_\mathrm{D}(\omega)\mathbf{V}_\mathrm{DL}\vec{\Psi}^i_{i,k_i}[\vec{\Psi}^i_{i,k_i}]^\dagger\mathbf{V}_\mathrm{LD}\right] \\
&= -\frac{e}{\hbar}\mathrm{Tr}\left[[\mathbf{G}^0_\mathrm{D}(\omega)]^\dagger\Gamma_\mathrm{R}(\omega)\mathbf{G}^0_\mathrm{D}(\omega)\mathbf{V}_\mathrm{DL}\vec{\Psi}^i_{i,k_i}[\vec{\Psi}^i_{i,k_i}]^\dagger\mathbf{V}_\mathrm{LD}\right].
\end{aligned}
\tag{64}
$$

By inserting this result into Eq. 59 and utilizing the definition of the spectral function from Eq. 24 and the coupling matrix from Eq. 37, the current at the D-R-interface due to injection of electrons from the left lead can be determined:

$$
\begin{aligned}
I^{(\mathrm{L})} &= -\frac{e}{\hbar}\int \mathrm{d}\omega\, f_\mathrm{L}(\omega)\sum_{i=1}^{N_\mathrm{L}}\sum_{k_i}\mathrm{Tr}_\mathrm{D}\left[[\mathbf{G}^0_\mathrm{D}(\omega)]^\dagger\mathbf{\Gamma}_\mathrm{R}(\omega)\mathbf{G}^0_\mathrm{D}(\omega)\mathbf{V}_\mathrm{DL}\vec{\Psi}^i_{i,k_i}[\vec{\Psi}^i_{i,k_i}]^\dagger\mathbf{V}_\mathrm{LD}\right] \\
&= -\frac{e}{\hbar}\int \mathrm{d}\omega\, f_\mathrm{L}(\omega)\mathrm{Tr}\left[[\mathbf{G}^0_\mathrm{D}(\omega)]^\dagger\mathbf{\Gamma}_\mathrm{R}(\omega)\mathbf{G}^0_\mathrm{D}(\omega)\mathbf{\Gamma}_\mathrm{L}(\omega)\right].
\end{aligned}
\tag{65}
$$

The derivation can be repeated for a wave incident from the right lead:

$$I^{(\mathrm{R})} = -\frac{e}{\hbar} \int \mathrm{d}\omega \, f_{\mathrm{R}}(\omega) \mathrm{Tr} \left[[\mathbf{G}^0_{\mathrm{D}}(\omega)]^{\dagger} \mathbf{\Gamma}_{\mathrm{R}}(\omega) \mathbf{G}^0_{\mathrm{D}}(\omega) \mathbf{\Gamma}_{\mathrm{L}}(\omega) \right] . \tag{66}$$

The total current is a sum over all possible incident waves from both leads:

$$I = I^{(\mathrm{L})} - I^{(\mathrm{R})} = \frac{e}{\hbar} \int \mathrm{d}\omega \, (f_{\mathrm{L}}(\omega) - f_{\mathrm{R}}(\omega)) \, \mathrm{Tr} \left[[\mathbf{G}^0_{\mathrm{D}}(\omega)]^{\dagger} \mathbf{\Gamma}_{\mathrm{R}}(\omega) \mathbf{G}^0_{\mathrm{D}}(\omega) \mathbf{\Gamma}_{\mathrm{L}}(\omega) \right] . \tag{67}$$

If both reservoirs have the same chemical potential $\mu_L = \mu_R$, the current is zero . Eq. 67 has the same form as the original Landauer formula from Eq. 50. The transmission function expressed in terms of the non-interacting device's GF $G^0_{\mathrm{D}}(\omega)$ and the coupling matrices is also known as Caroli expression[138]:

$$\mathcal{T}^0(\omega) = \mathrm{Tr} \left[[\mathbf{G}^0_{\mathrm{D}}(\omega)]^{\dagger} \mathbf{\Gamma}_{\mathrm{R}}(\omega) \mathbf{G}^0_{\mathrm{D}}(\omega) \mathbf{\Gamma}_{\mathrm{L}}(\omega) \right] . \tag{68}$$

Discussion: The description of quantum transport is, in principle, a time-dependent, non-equilibrium statistical problem[136]. Most of these aspects are too complex to be fully taken into account, and various approximations had to be made to arrive at Eq. 50 and Eq. 67. We are, for instance, not interested in the exact physical processes within the leads or chemical processes within the battery which is providing the current. This is typically a good approximation, since the transport properties are relatively insensitive to the exact details of the leads if the leads are significantly larger than the nanojunction[130].

Transport is inherently out of equilibrium, even if the system reaches a steady state, so it becomes generally necessary to determine the non-equilibrium density matrix in order to compute the system properties out of equilibrium. This is considerably more complicated and results, for instance, in a voltage-dependent transmission function $T(\omega, V)$. In this work, however, we deal with typical STM situations in the tunneling regime, where the applied bias voltage V will mostly drop between the STM tip and the substrate. We can therefore assume that the chemical potential of the surface remains at $\mu_{\mathrm{sur}} = \mu$, while that of the STM tip depends on the bias voltage V according to $\mu_{\mathrm{tip}} = \mu + eV$[127], and no full non-equilibrium calculation is necessary. This further simplifies the calculation of the differential conductance $G(V)$ for small biases and zero temperature

$$G(V) = \frac{\partial I}{\partial V} = \frac{2e^2}{h} T^0(eV), \tag{69}$$

which then only depends on the value of the transmission function at the given bias $T(eV)$.

The Landauer formula was derived for a system of non-interacting electrons. In order to describe transport of an interacting device coupled to non-interacting leads, the Meir-Wingreen formula[139] has to be used, which is considerably more complicated. It does, however, reduce to the Landauer formula under certain conditions: either if interactions beyond mean-field are switched off[136], or in the limit of zero temperature and zero bias, but using the fully interacting one-body GF. In this work, the latter will be the case: the (approximate) fully interacting GF will be used, incorporating effects of strong electronic correlations, at low temperatures and small bias voltages.

This work proceeds as follows: it first combines KS-DFT with the Landauer approach[124;125;128;131], using the one-body KS-GF as a starting point to compute the non-interacting GF $\mathbf{G}^0_D(\omega)$ and the transmission function $\mathcal{T}^0(\omega)$. As has been discussed in Sec. 2.1.4, the KS orbitals can be an appropriate approximation, particularly for non-localized orbitals and close to the Fermi level[88]. To arrive at the fully-interacting GF and in order to describe Kondo physics, correlation effects will be taken into account within the C region, by solving an Anderson impurity model to obtain the self energy Σ_C. This will be discussed in the next section.

2.4 The Kondo effect and the Anderson impurity model

If a magnetic impurity is inserted into a non-magnetic host metal, under certain circumstances a local moment can form, so that double occupation of impurity states is energetically unfavorable, and the impurity is singly occupied. First experimental evidence of that fact was found by J. de Boer[140]: a variety of transition metal oxides predicted to be conductors by band theory proved to be insulators , and N. Mott explained this anomaly by including the electron-electron interaction at the impurity[44]. Several impurity models emerged to explain the physics of local moments, namely the *s*-*d* model[141], a phenomenological model by Friedel[142] and the Anderson impurity model (AIM)[143]. The latter will play a central role in this work. The AIM Hamiltonian for a single impurity level d is:

$$H_\mathrm{sAIM} = \epsilon_d n_d + U n_{d\uparrow} n_{d\downarrow} + \sum_{k,\sigma} \epsilon_k c^\dagger_{k\sigma} c_{k\sigma} + \sum_{k,\sigma} V_k \left(d^\dagger_\sigma c_{k\sigma} + c^\dagger_{k\sigma} d_\sigma \right). \tag{70}$$

The impurity state d with energy ϵ_d is coupled to a set of conduction electrons k with energy ϵ_k by an interaction V_k. $d^\dagger_\sigma/d_\sigma$ and $c^\dagger_{k\sigma}/c_{k\sigma}$ are creation and annihilation operators of impurity and conduction electron states, respectively, while $n_{d\sigma} = d^\dagger_\sigma d_\sigma$ and $n_d = \sum_\sigma n_{d\sigma}$ are the corresponding number operators. The AIM explicitly includes the Coulomb interaction U between electrons at the impurity state d. This term favors single-occupancy of the impurity level, since adding a second electron to the impurity costs an additional energy U, which is typically high for spatially localized d states. The conduction electrons (also called bath) are assumed to be non-interacting and only contain electronic interactions on a mean-field level. This is justified because the conduction band is typically formed by more delocalized s electrons. In chapter 5, we will work with a multi-orbital Anderson model, where the full d shell of the impurity atom is included. It has the form:

$$H_\mathrm{mAIM} = \sum_i \epsilon_{d_i} n_{d_i} + \sum_{\substack{ijkl \\ \sigma,\sigma'}} U_{ik;jl} d^\dagger_{i\sigma} d^\dagger_{j\sigma'} d_{l\sigma'} d_{k\sigma} + \sum_{k,\sigma} \epsilon_k c^\dagger_{k\sigma} c_{k\sigma} + \sum_{k,i,\sigma} V_{ki} \left(d^\dagger_{i\sigma} c_{k\sigma} + c^\dagger_{k\sigma} d_{i\sigma} \right). \tag{71}$$

Once a local moment has formed, it is possible for the Kondo effect to occur. When the temperature is reduced, an antiferromagnetic coupling between the impurity and the conduction

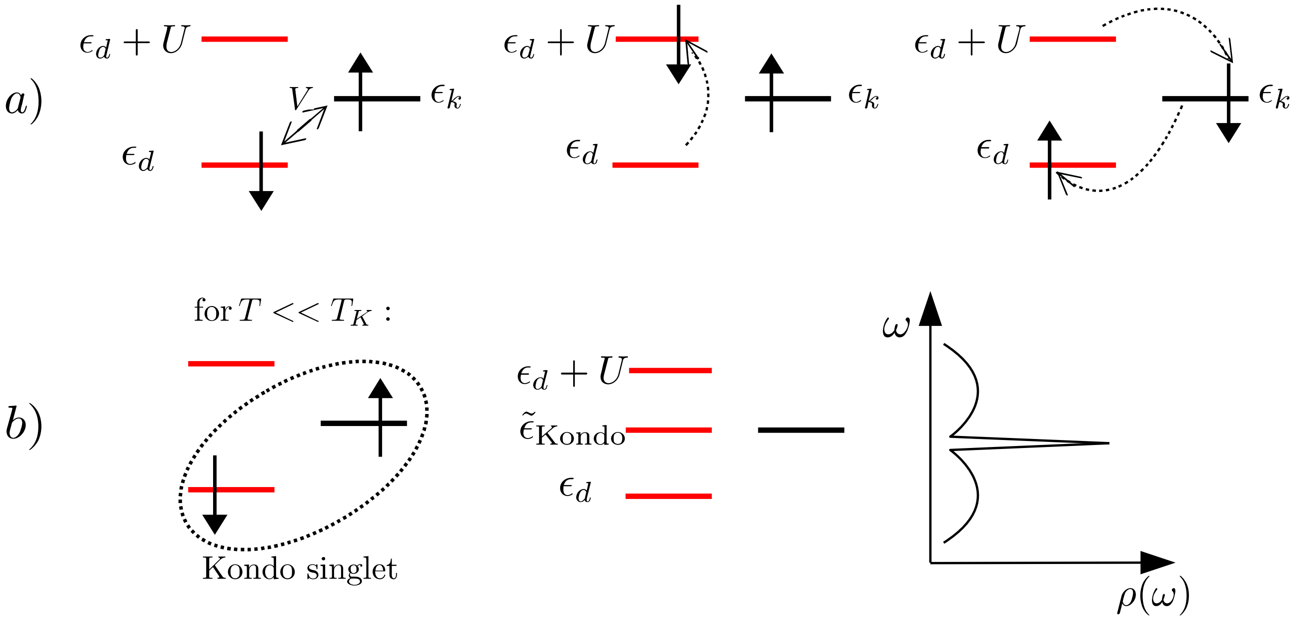

Figure 3: a) Typical spin flip processes between impurity and conduction electrons. b) At low temperatures, the spin-flip processes lead to the formation of the Kondo singlet. An additional narrow level close to the Fermi level develops and manifests itself as the Kondo resonance in the density of states.

electrons can develop, quenching the impurity spin and forming a spin singlet $S = 0$, and a narrow resonance close to the Fermi level (see Fig. 3). The first manifestation of the Kondo effect was observed in 1934 in low-temperature resistance measurements of gold samples which contained iron impurities[39]. The resistance did not decrease monotonically when the temperature was lowered, but reached a resistance minimum at a finite temperature. In 1964, Jun Kondo explained this anomaly[41] by employing the s-d model[141], also called Kondo model,

$$H_{s-d} = -\sum_{k,k'} J_{k,k'}(\Psi_k^\dagger S \Psi_{k'}) \cdot (\Psi_d^\dagger S \Psi_d) + \sum_{k\sigma} \epsilon_{k\sigma} c_{k\sigma}^\dagger c_{k\sigma}, \qquad (72)$$

where $J_{k,k'}$ is a Heisenberg exchange interaction between the conduction electrons and the magnetic impurity[144]. At sufficiently low temperatures, the localized impurity spin interacts antiferromagnetically ($J < 0$) with the conduction electron spins of the conduction electrons. Using third-order perturbation theory in the coupling J, Kondo derived a $\ln T$ dependence of the resistivity, explaining the resistance minimum of Ref. [39].

The s-d model can be obtained from the AIM by the Schrieffer-Wolff transformation[145], which perturbatively diagonalizes the system's Hamiltonian and is often used to project out high-energy states in order to obtain an effective low-energy model, and can be seen as the strong-coupling limit of the AIM. The transformation also shows that the coupling between impurity and conduction electrons becomes antiferromagnetic at low temperatures.

Since the s-d model cannot describe all aspects of the Kondo effect, the AIM will be the central focus of this section.

2.4.1 Extracting AIM parameters from DFT-based transport calculations

The AIM is a model Hamiltonian, and conceptually distinct from DFT[43]. While model Hamiltonians are typically used to describe a certain physical aspect at low energies and require various input parameters, DFT is an *ab initio* method, not requiring any free parameters (knowledge of the exact functional and a complete basis set provided), and yielding the full energy spectrum of the system. In realistic situations, however, approximations for the exchange-correlation functional have to be made. Typical local and semi-local functionals fail to describe more complex physical effects, like strong electronic correlations, which are a central focus of this work.

One possible solution to that problem is to combine both methods: the *ab initio* method is used as a starting point, giving a reliable description of the major part of the system where it is sufficient to treat electronic correlations on a mean-field level. The mean-field result is then used to extract the parameters of the model Hamiltonian, which is subsequently solved to obtain the physics that the *ab initio* method fails to describe. Even if the *ab initio* method fails to reproduce the low-energy physics of the system, it still can give appropriate values for the parameters of the model Hamiltonian[43]. Also note that the model Hamiltonian parameters are typically determined by the high-energy part of the spectrum and cannot be determined from within the model itself. The model Hamiltonian can then be solved in order to give a more reliable description of the low-energy physics[121]. A detailed account of the possible connections between DFT and model Hamiltonians can be found in the review by K. Capelle[43].

As a first step, the correlated region has to be defined. In this work, it is the partially filled $3d$ shell of the Co adatom (see Fig. 1), but can more generally be the open d or f shells of transition metal and rare earth atoms, quantum dots weakly coupled to leads[146] or the correlated orbitals of certain organic molecules[147]. The central requirement is that the Coulomb interaction U within the orbital is strong compared to the coupling Γ to the rest of the system[70].

Many AIM parameters can be extracted directly from the DFT-based transport calculation. The energy of the correlated level(s) is given by the diagonal elements of the KS-Hamiltonian in the C subspace $\epsilon_{d_i}^{\mathrm{KS}}$. The Coulomb interaction has been taken into account on a mean-field level in the DFT calculation already. In order to not include the Coulomb interaction twice, a double-counting term has to be added:

$$\epsilon_{d_i} = \epsilon_{d_i}^{\mathrm{KS}} - V_i^{\mathrm{DCC}}. \tag{73}$$

Unfortunately, the double counting correction (DCC) is not known exactly for DFT, and several different approximations exist[43;148]. This work uses two versions of the fully-localized limit (FLL)[149] DCC, namely the conventional (isotropic) version

$$(V_{FLL}^{\mathrm{DCC}}) = U\left(N_{\mathrm{C}} - \frac{1}{2}\right) - \frac{1}{2}J_H\left(N_{\mathrm{C}} - 1\right), \tag{74}$$

and its generalized version for the case of an anisotropic Coulomb repulsion[150],

$$(V_{aFLL}^{\mathrm{DCC}})_{ii} = \sum_j U_{ii;jj}\left(n_j - \frac{1}{2M_{\mathrm{C}}}\right) - \frac{1}{2}J_H(N_{\mathrm{C}}-1), \tag{75}$$

where U is the orbital-averaged Coulomb repulsion, J_H the orbital-averaged Hund's rule coupling, n_j is the occupation of orbital j, N_{C} the total occupation of the correlated subspace and M_{C} its dimension. Note that U_{ijkl} appearing in Eq. 70 is not the bare Coulomb interaction (which is trivial to compute), but an effective Coulomb interaction that already contains all screening effects from outside of the correlated subspace. While it is often fitted to experimental values or estimated, it is desirable to determine U_{ijkl} *ab initio*, and different methods to approximately compute it exist. This will be discussed separately in chapter 4.

The couplings V_k can be determined from the so-called hybridization function $\mathbf{\Delta}(\omega)$, which describes the coupling of the correlated subspace C to the conduction electrons. The non-interacting Green's function of the correlated subspace can be obtained by projection of the non-interacting device GF from Eq. 35 (henceforth labeled G_D^0), and can be expressed as:

$$\mathbf{G}_{\mathrm{C}}^0(\omega) = \hat{P}_{\mathrm{C}}\mathbf{G}_{\mathrm{D}}^0\hat{P}_{\mathrm{C}} = (\omega + \mu - \mathbf{H}_{\mathrm{C}} - \mathbf{\Delta}_{\mathrm{C}}(\omega))^{-1}. \tag{76}$$

The hybridization function $\mathbf{\Delta}_{\mathrm{C}}(\omega)$ is the difference between the inverse of the GF of the isolated correlated region and the GF of the correlated region obtained by projection:

$$\mathbf{\Delta}_{\mathrm{C}}(\omega) = \omega + \mu - \mathbf{H}_{\mathrm{C}} - [\mathbf{g}_{\mathrm{C}}^0(\omega)]^{-1}. \tag{77}$$

To obtain the couplings V_k appearing in Eq. 70, the hybridization function can be written as

$$\mathbf{\Delta}_{\mathrm{C}}(\omega) = \sum_k \frac{|V_k|^2}{\omega - \epsilon_k}. \tag{78}$$

Note that the hybridization function is a self energy in the same spirit as the lead self energies $\Sigma_{\mathrm{L/R}}$ from Eq. 35, but typically labeled Δ_{C} in the context of AIMs.

After we have established how to obtain AIM parameters from the DFT-based transport calculation, the next section will discuss how to solve the AIM.

2.4.2 Solving the AIM

Conventional many-body perturbation theory typically uses the non-interacting solution as a starting point and treats the Coulomb interaction as perturbation to the system. This is not possible for strongly correlated materials, though, since the Coulomb interaction U is strong compared to the single-particle coupling and cannot be treated perturbatively. Alternative approaches are therefore necessary, typically using the diagonalized impurity Hamiltonian as a starting point[70].

Several methods to solve the AIM have been developed. It can be solved exactly by Numerical Renormalization group calculations[151;152]. Unfortunately, the numerical effort increases exponentially with the number of impurities, and currently a maximum of two impurities can be treated. It was also shown that the symmetric Anderson model is completely integrable using a Bethe Ansatz[153;154] (the same technique was successfully applied to the *s*-*d* model[155;156]). The Continuous-Time Quantum Monte Carlo method (CTQMC)[157] is numerically exact, but only gives results on the Matsubara axis, which then have to be analytically continued to real energies. This analytical continuation is a considerable problem and may lead to artifacts in the spectra. CTQMC is also limited to relatively high temperatures and therefore suboptimal to study low-temperature phenomena like the Kondo effect.

Several approximate techniques to solve the AIM exist as well. The basic idea of the Exact Diagonalization method is to approximate the continuous bath, represented by the hybridization function $\mathbf{\Delta}(\omega)$, by a finite number of discrete bath levels which interact with the impurities[158]. This system is then diagonalized. Since the size of the many-body space grows exponentially with every bath level included, this method is limited to relatively few bath levels, which poses a severe limitation[159] and leads to artifacts in the spectrum[70]. One possibility to increase the number of bath levels which can be treated is the Lanczos diagonalization scheme[160]. Another option is to randomly generate a set of bath levels representing the continuous bath, perform an exact diagonalization and afterwards average the obtained self energies for all random configurations, as it is done in the Distributional Exact Diagonalization method[161;162]. Several ideas of how to describe Kondo physics within TDDFT exist as well[43;115;116;117].

2.4.3 The non-crossing and the one-crossing approximations

This work uses the one-crossing approximation (OCA)[163], an extension of the non-crossing approximation (NCA)[164;165], both diagrammatic expansions around the atomic limit, where only a certain infinite subset of diagrams is taken into account. The basic idea is to include the Coulomb interaction exactly and treat the hybridization $\mathbf{\Delta}_C(\omega)$ as a perturbation to the exact solution in the atomic limit. To this end, an exact diagonalization of the isolated correlated subspace is performed, yielding the many-body eigenstates $|m\rangle$ of the isolated correlated subspace,

$$\hat{H}_{\mathrm{C}} = \sum_{i} \epsilon_{d_i} n_{d_i} + \sum_{\substack{ijkl \\ \sigma,\sigma'}} U_{ik;jl} d^{\dagger}_{i\sigma} d^{\dagger}_{j\sigma'} d_{l\sigma'} d_{k\sigma} \overset{\mathrm{diag}}{=} \sum_{m} \epsilon_m |m\rangle\langle m|, \tag{79}$$

which serve as the starting point.

It is convenient to rewrite the d electron operators in terms of pseudoparticle (PP) creation $a^{\dagger}_m$ and annihilation a_m operators. Each PP corresponds to an impurity state, and $a^{\dagger}_m$ creates the state $|m\rangle$ from the PP vacuum $|\mathrm{PPV}\rangle$[166]:

$$a^{\dagger}_m |\mathrm{PPV}\rangle \equiv |m\rangle. \tag{80}$$

The a_m are either bosonic or fermionic, depending whether the state $|m\rangle$ has an even or odd number of electrons. Note that it is mathematically possible to create several pseudo-particles at the same time, which would be unphysical. Due to the completeness of the impurity eigenstates, the system has to be in either of the physical states, or a mix thereof,

$$Q = \sum_m a_m^\dagger a_m = 1, \tag{81}$$

where Q is the PP charge. The physical operators can be expressed in terms of the PP operators

$$d_{i\sigma} = \sum_{m,n} F_{i\sigma}^{mn} a_n^\dagger a_m, \tag{82}$$

with matrix elements $F_{i\sigma}^{mn} = \langle m|d_{i\sigma}|n\rangle$. The Hamiltonian of the mAIM from Eq. 71 can then be rewritten in terms of the PPs, including the constraint from Eq. 81 by means of a Lagrange multiplier λ which can be interpreted as the chemical potential of the PPs[166]:

$$\hat{H}_{\text{AIM}} = \sum_m \epsilon_m a_m^\dagger a_m + \sum_{k,\sigma} \epsilon_k c_{k\sigma}^\dagger c_{k\sigma} + \sum_{\substack{k,i,\sigma \\ m,n}} V_{k,i} \left(a_m^\dagger F_{i\sigma}^{mn} a_n c_{k\sigma} + c_{k\sigma}^\dagger a_m^\dagger F_{i\sigma}^{mn} a_n \right). \tag{83}$$

The PP operators obey commutation (bosons) or anticommutation (fermions) relations, Wick's theorem is therefore applicable and a perturbation expansion in the hybridization strength, making use of the PP operators, becomes possible. The corresponding propagators are:

$$G_m(\omega_n) = \frac{1}{\omega - \epsilon_m - \lambda - \Sigma_m(\omega)}. \tag{84}$$

The self-energies $\Sigma_f(\omega)$ describe the interaction between different PPs. So far, the mAIM has only been rewritten, and no approximations have been made. The next step is to expand $\Sigma_m(\omega)$ into diagrams, and choose a certain subset of diagrams.

The NCA is the expansion in the hybridization strength to lowest order, and describes processes where a single electron hops from the impurity to the bath (creating a state with $N-1$ particles) or from the bath to the impurity (creating a state with $N+1$ particles). It includes an infinite resummation of diagrams where conduction electron lines do not cross (see Fig. 4). The fermionic self-energies depend on the dressed bosonic propagators, while the bosonic self energies depend on the dressed fermionic propagators, so the NCA equations have to be solved self-consistently. The OCA is obtained analogously, but by including second-order diagrams where two conduction electron lines cross (see Fig. 4). After the NCA or the OCA equations have been solved, the PP self energies are known. To obtain results for real particles on the real energy axis, the real operators can be expressed in terms of the PP operators. After some algebra, the GF of the interacting subspace $\mathbf{G}_\text{C}(\omega)$ is obtained. The algebraic expressions for NCA[167] and OCA[163] can be found in the literature.

Once the GF of the interacting subspace is known, the correlated self energy $\mathbf{\Sigma}_\text{C}$ can be obtained, making use of the non-interacting GF of the C subspace from Eq. 76:

$$\hat{\mathbf{\Sigma}}_\text{C}(\omega) = [\hat{\mathbf{G}}_\text{C}^0(\omega)]^{-1} - [\hat{\mathbf{G}}_\text{C}(\omega)]^{-1}. \tag{85}$$

An advantage of NCA and OCA is that all physical quantities are computed directly on the real energy axis, so that no analytical continuation from the Matsubara to the real axis, which

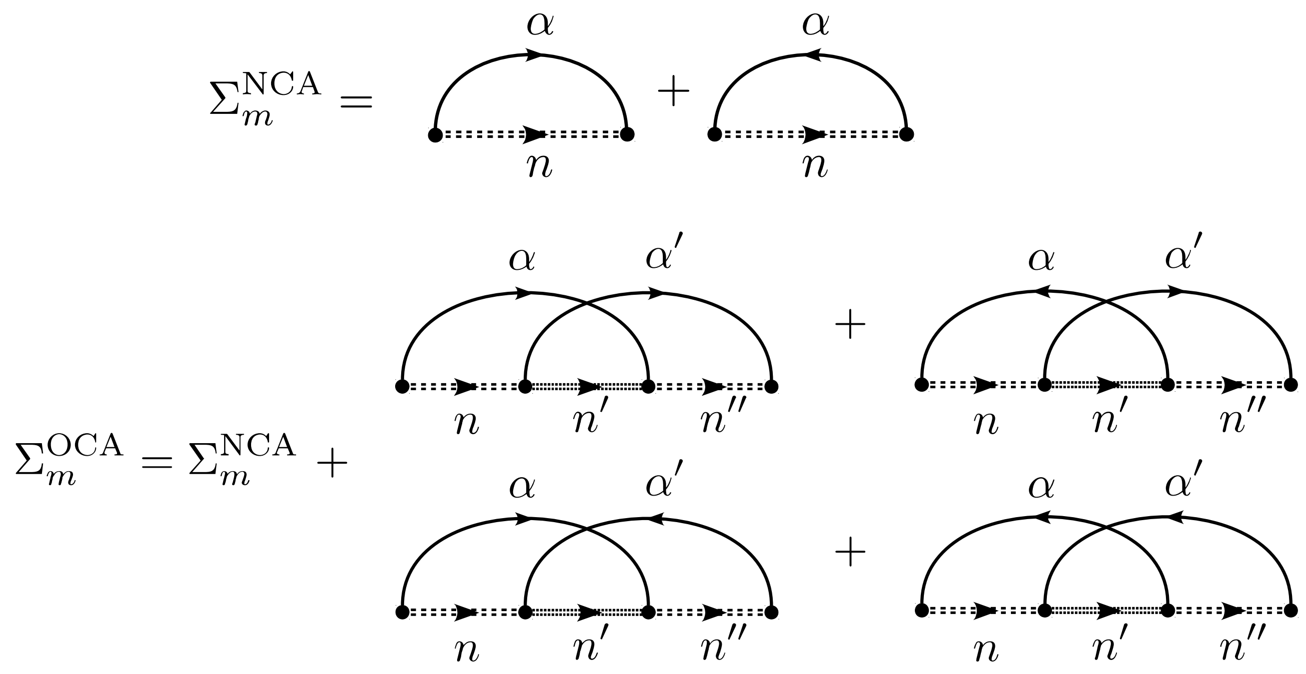

Figure 4: Self-energy diagrams for pseudoparticles m in the NCA and the OCA. Double-dashed lines correspond to the full pseudoparticle propagators, while single continuous lines correspond to conduction electron propagators.

would introduce artifacts in the spectrum, is necessary. It is computationally feasible to treat the full d or f shell of transition metal and Lanthanide atoms within NCA and OCA, while taking into account the complete energy dependence of the bath, albeit perturbatively. Being approximations, NCA and OCA have certain deficiencies: for too low temperatures (below the Kondo temperature T_K for the NCA and one to two orders below T_K for the OCA[70]) both methods fail to capture Fermi liquid behavior and result in an overestimation of the height of the Kondo peak and artifacts like an unphysical self-energy with positive imaginary part in the spectra in the zero-temperature limit[168]. Ref. [169] points out some deficiencies of the OCA in the description of the Mott transition in comparison to CTQMC. Ref. [170] showed that NCA and OCA violate certain sum rules, and that the deviation from the sum rule gives an estimate of the reliability of the approximation, with larger deviations occurring for multiple orbitals, away from particle-hole symmetry and for low correlation strengths. It was also shown that the OCA is considerably more reliable than the NCA.

Overall, the combination of the OCA with DFT-based transport calculations has been successfully applied to various systems[70;171], and is a reliable way to study Kondo physics in realistic materials.

2.4.4 Including AIM results in transport calculation

After solving the AIM, the results can now be fed back to the transport calculation. The self energy $\mathbf{\Sigma}_{\text{C}}(\omega)$ is added to the non-interacting GF $\mathbf{G}^0_{\text{D}}(\omega)$, where V_{DCC} is the double-counting correction within the C subspace:

$$\begin{aligned}\mathbf{G}_D(\omega) &= \left((\mathbf{G}^0_\mathrm{D}(\omega))^{-1} - (\mathbf{\Sigma}_\mathrm{C}(\omega) - V_\mathrm{DCC})\right)^{-1} \\ &= (\omega - \mathbf{H}_\mathrm{D} - \mathbf{\Sigma}_\mathrm{L}(\omega) - \mathbf{\Sigma}_\mathrm{R}(\omega) - (\mathbf{\Sigma}_\mathrm{C}(\omega) - V_\mathrm{DCC}))^{-1}\,.\end{aligned} \tag{86}$$

The interacting device GF $\mathbf{G}_\mathrm{D}(\omega)$ now contains the strong electronic correlations within the C subspace.

The current through a strongly-interacting device coupled to non-interacting leads is described by the Meir-Wingreen formula[139], which is considerably more complex than the Landauer formula, and would require the impurity problem to be solved out of equilibrium, which has only be achieved for non-realistic test systems and model Hamiltonians[172;173;174]. However, even when strong electronic correlations are present, the Meir-Wingreen formula can be approximated by the Landauer formula in the limit of low temperatures and low bias (also see the more detailed discussion in Sec. 2.3). The transmission function, including electronic correlations, is

$$\mathcal{T}(\omega) = \mathrm{Tr}\left[[\mathbf{G}_\mathrm{D}(\omega)]^\dagger \mathbf{\Gamma}_\mathrm{R}(\omega)\mathbf{G}_\mathrm{D}(\omega)\mathbf{\Gamma}_\mathrm{L}(\omega)\right]. \tag{87}$$

It resembles Eq. 68, but uses the interacting GF in equilibrium $\mathbf{G}_\mathrm{D}(\omega)$.

It is also possible to compute an updated charge density from the interacting device's GF $\mathbf{G}_\mathrm{D}(\omega)$:

$$\mathbf{P}_\mathrm{D} = -\frac{1}{\pi}\mathrm{Im}\int_{-\infty}^{0} \mathrm{d}\omega\,\mathbf{G}_\mathrm{D}(\omega + \mathrm{i}\eta). \tag{88}$$

This charge density can then be used to determine a new KS Hamiltonian, new AIM parameters can be extracted, and the updated AIM can be solved. This charge-density cycle will be used in chapter 5, where in the last part of the chapter, the Coulomb interaction within the correlated subspace U will also be computed self-consistently. The computation of U will be discussed in more detail in chapter 4.

3 Orbital signatures of Fano-Kondo line shapes in STM adatom spectroscopy

When studying Kondo physics in the context of STM adatom spectroscopy, a so-called zero-bias anomaly (ZBA) is observed in the tunnel spectrum. It is caused by the Kondo effect and manifests itself in the local DOS of the probed atom or molecule. The ZBA can range from peaks, asymmetric line shapes to dips and is typically well-described by a Fano line shape. Some works explain the occurrence of Fano line shapes in STS as an interference process between different tunneling paths[68;175;176], one directly into the substrate, the other into the strongly correlated orbital bearing the Kondo resonance. Other works explain the occurring line shapes as a result of tunneling into the surface alone[62;63;64;177;178], where the Kondo resonance is not involved in the tunneling process itself and only indirectly affects the conduction electrons which are probed by the STM tip. This chapter will shed more light on this question, by studying the influence of various parameters on the resulting line shapes, and by providing a simple model to explain the results. Furthermore, up to now the connection between the symmetry of the orbital carrying the Kondo effect and the resulting Fano line shape has not been systematically studied. This question will also be answered in this chapter (also see Ref. [179]). To this end, an individual d orbital will be selected and an ab-initio transport calculation will be performed, where only the selected d orbital is correlated. There is merit to that: While it is in principle necessary to correlate the complete $3d$ shell (as will be done in chapter 5), the Kondo resonance can often be attributed to an individual orbital. Even if there are multiple orbitals exhibiting Kondo physics, one d orbital will often be the more dominant in the tunnel spectrum due to different Kondo scales and higher tunneling matrix elements. The focus of this chapter is not to provide a complete ab initio description, though. Each of the orbitals will be correlated, and the resulting line shapes will be compared. This will be done for both Co@Cu(001) and Co@Cu(111), and only the tunneling regime will be considered.

This chapter is structured as follows: first, the concept of Fano line shapes is introduced, followed by details about the computational scheme used in this chapter. Results are presented for Co@Cu(001) and Co@Cu(111), investigating the influence of orbital symmetry, Coulomb interaction U, occupation (controlled by the level position ϵ_d) and temperature T on the resulting line shapes. A simple model is introduced in order to predict line shapes controlled by a few parameters only.

3.1 Fano line shapes

Fano line shapes or Fano resonances were first described in the context of autoionization and elastic electron scattering by helium[180], but can generally arise in scattering processes, due to quantum interference between a quasi-discrete resonant state and a broad continuum of states. This interference can be observed in the scattering cross section and can manifest itself in various line shapes, including peaks, dips and asymmetric shapes. The possible line shapes can be described in terms of the Fano function[180],

$$f(\epsilon) \propto \frac{(q+\epsilon)^2}{\epsilon^2+1}, \tag{89}$$

where the q parameter controls the line shape of the Fano function, ϵ is the the energy with respect to the resonance position, and the resonance is assumed to be of Lorentzian shape. A dip is obtained for $q = 0$, a peak for $q = \pm\infty$, and asymmetric line shapes for q values in between.

An alternative way of writing Eq. 89 is by using the complex representation of a Lorentzian and shifting it by a phase factor,

$$\rho_{\mathrm{FL}}(\omega) = \mathrm{Im}\left[\mathrm{e}^{\mathrm{i}\phi_q}\left(\frac{A}{\omega-\omega_0+\mathrm{i}\Gamma}\right)\right] + \rho_0, \tag{90}$$

where A is the amplitude, Γ the half-width of the Lorentzian, ω_0 the position of the resonance, ρ_0 some background, and $\mathrm{e}^{\mathrm{i}\phi_q}$ a q-dependent phase factor. Using the definitions $q = \tan(\phi_q/2)$ and $\epsilon = (\omega-\omega_0)/\Gamma$, we can show the equivalence to Eq. 89 (see appendix A for the derivation):

$$\rho_{\mathrm{FL}}(\omega) = \frac{A}{\Gamma}\left(\frac{(q+\epsilon)^2}{\epsilon^2+1} - 1\right)\frac{1}{1+q^2} + \rho_0. \tag{91}$$

A similar situation occurs in STS, where the transmission shows Fano-like features, due to quantum interference of the Kondo peak with the surrounding conduction electrons. While the previous formulas are all based on a Lorentzian resonant level, Frota showed that the Kondo peak is much better described by a so-called Frota line shape[181;182],

$$\rho_{\mathrm{Frota}}(\omega) = A \cdot \mathrm{Re}\left[\sqrt{\frac{\mathrm{i}\Gamma_{\mathrm{F}}}{\omega-\omega_0+\mathrm{i}\Gamma_{\mathrm{F}}}}\right], \tag{92}$$

where the Frota parameter Γ_{F} is related to the actual half-width Γ of the resonance by $\Gamma = 2.54\,\Gamma_{\mathrm{F}}$, A is the amplitude and ω_0 the position of the Frota resonance.

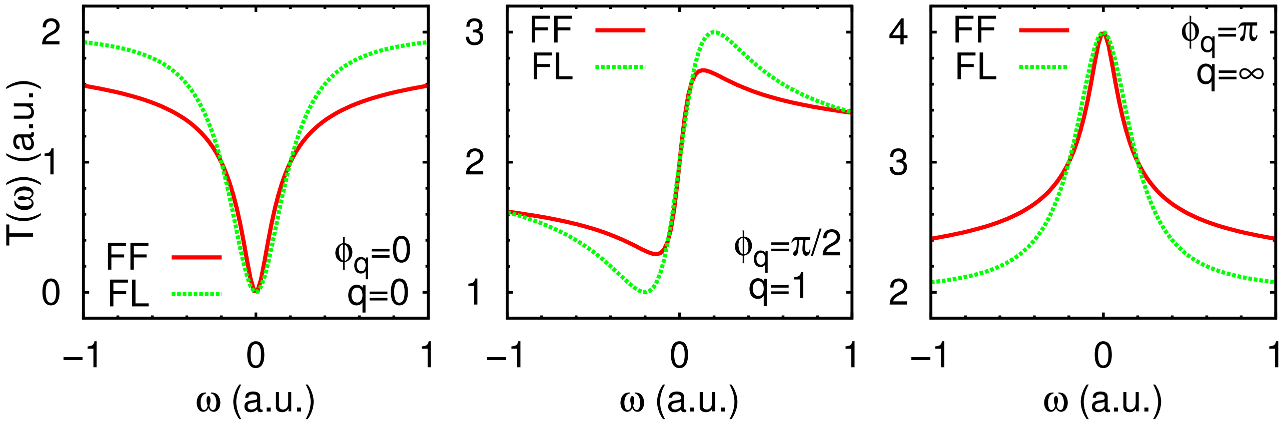

Figure 5: Comparison of Fano-Frota (FF) and Fano-Lorentz (FL) line shapes for different values of the q parameter but for identical amplitudes and half-widths.

In the same spirit as Eq. 91, we define a Fano-Frota line shape, as has been proposed by Prüser et al.[183;184], by shifting the Frota line shape of Eq. 92 by a complex phase factor ϕ_q:

$$T_{\mathrm{FF}}(\omega) = -A \cdot \mathrm{Re}\left[\mathrm{e}^{\mathrm{i}\phi_q} \sqrt{\frac{\mathrm{i}\Gamma_{\mathrm{F}}}{\omega - \omega_0 + \mathrm{i}\Gamma_{\mathrm{F}}}} \right] + T_0. \tag{93}$$

Eq. 93 is defined such that the same definition of ϕ_q as above can be used. A value of $\phi_q = 0$ leads to a dip, $\phi_q = \pi$ to a peak and $\phi_q = \pm\pi/2$ to symmetric Fano line shapes.
In Fig. 5, Fano-Lorentz and Fano-Frota shapes are compared. The Fano-Frota shape is slightly narrower close to the minimum/maximum, and exhibits a slower decay at the flanks. Line shapes for a realistic calculation will be presented in Sec. 3.3.

3.2 Computational details

We perform DFT based *ab initio* quantum transport calculations using the ANT.G package[127], using the methodology introduced in the previous chapter. The electronic structure of the D region is calculated on the level of Kohn-Sham (KS) DFT employing the LSDA functional[83] in the SVWN parametrization[85;86] and a minimal Gaussian basis set including the valence ($4s4p3d$) and outer core electrons ($3s3p$) of the Co and Cu atoms[185;186;187;188;189]. The importance of including the semi-core states was pointed out in the past[190;191;192;193]. The electrodes L and R, here the STM tip and the rest of the Cu surface, respectively, are modeled by Bethe lattices.
In this chapter, we are interested in the Kondo signatures of specific d orbitals, and not of the entire $3d$ shell. Hence we add a Hubbard-like interaction term $\hat{\mathcal{H}}^U = U\hat{n}_{d_\uparrow}\hat{n}_{d_\downarrow}$ only to a *single* d orbital of the Co $3d$ shell, where U is treated as a parameter. Since the Coulomb interaction in the correlated d orbital has already been taken into account on a mean-field level in the KS-DFT calculation, a double-counting correction (DCC) term has to be subtracted from the KS Hamiltonian projected onto the d orbital $\epsilon_d^{\mathrm{KS}} = \langle d|\hat{H}_{\mathrm{D}}^{\mathrm{KS}}|d\rangle$:

$$\epsilon_d = \epsilon_d^{\mathrm{KS}} - \epsilon^{\mathrm{DCC}}. \tag{94}$$

The DCC is chosen such that a certain occupancy is achieved, i.e. for achieving particle-hole (ph) symmetry ($n_d = 1$) we choose ϵ^{DCC} such that $\epsilon_d = -U/2$. Note that ph symmetry is only approximately achieved since the coupling of the d orbital to the rest of the system (see below) is generally not ph symmetric.
The hybridization functions from Fig. 7 together with the energy level ϵ_d and the effective Coulomb interaction U define a sAIM (see Eq. 70) which is solved in the OCA[163]. It is a known issue of the OCA that at too low temperatures (1-2 orders of magnitude below T_{K}) it gives rise to spurious non-Fermi liquid behavior and related artifacts in the impurity spectral function, leading to an overestimation of the height of the Kondo peak and an unphysical self-energy with positive imaginary part[168]. We circumvent this problem by lowering the temperature only to the point where the imaginary part of the self-energy becomes zero. At

this point Fermi liquid behavior is obeyed, and the unitary limit of the Kondo peak is exactly recovered. The computational scheme is depicted in Fig. 6.

3.3 Co adatom on Cu(001) surface

The system under consideration is shown in the left panel of Fig. 7. A Cobalt atom is deposited at the hollow site of a Cu(001) surface. The Cu(001) surface is modeled by three Cu slabs of 36, 25 and 16 atoms, respectively, which are embedded into a Bethe lattice to describe the infinitely extended surface. We model the STM tip by a small pyramid of Cu atoms grown in

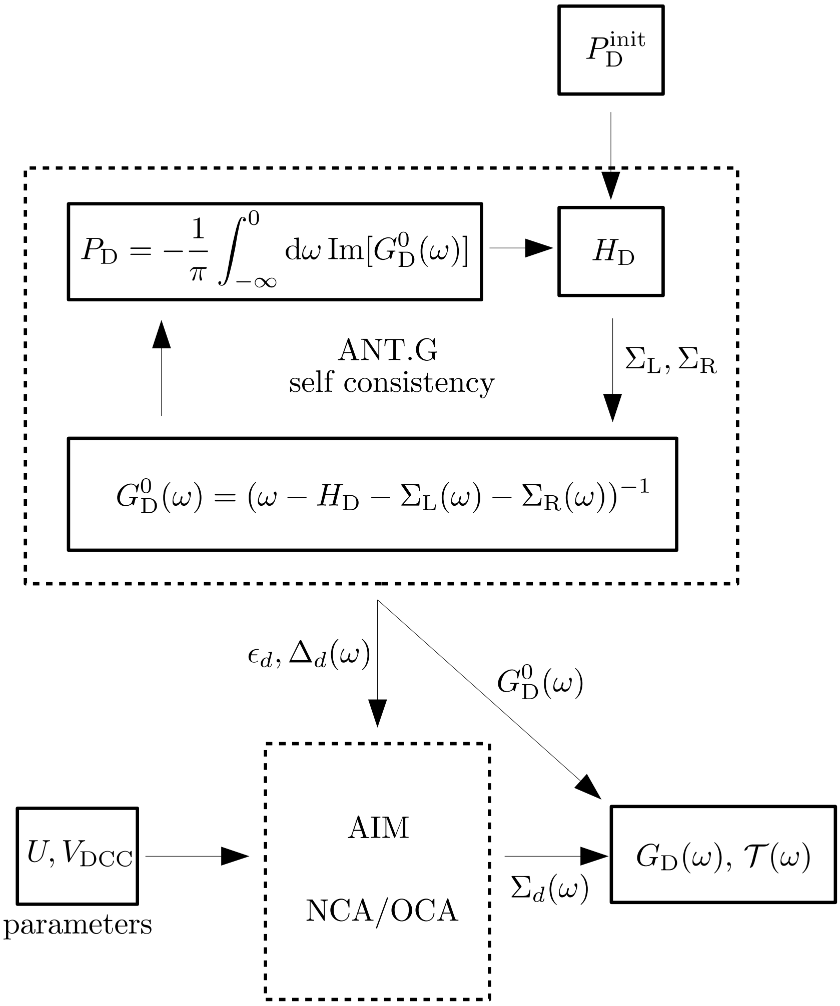

Figure 6: Computational scheme to determine the correlated transmission for a single d level. First, the non-interacting GF $G_D^0(\omega)$ is determined self-consistently, employing the ANT.G code. An AIM is defined by the energy of the d level and the hybridization function $\Delta_d(\omega)$, while the Coulomb interaction U and double counting correction V_DCC are included as tunable parameters. The AIM is solved within the NCA and OCA, respectively, and the correlated self energy $\Sigma_d(\omega)$ is determined. As a last step, the correlated GF G_D and corresponding correlated transmission $\mathcal{T}(\omega)$ can be calculated.

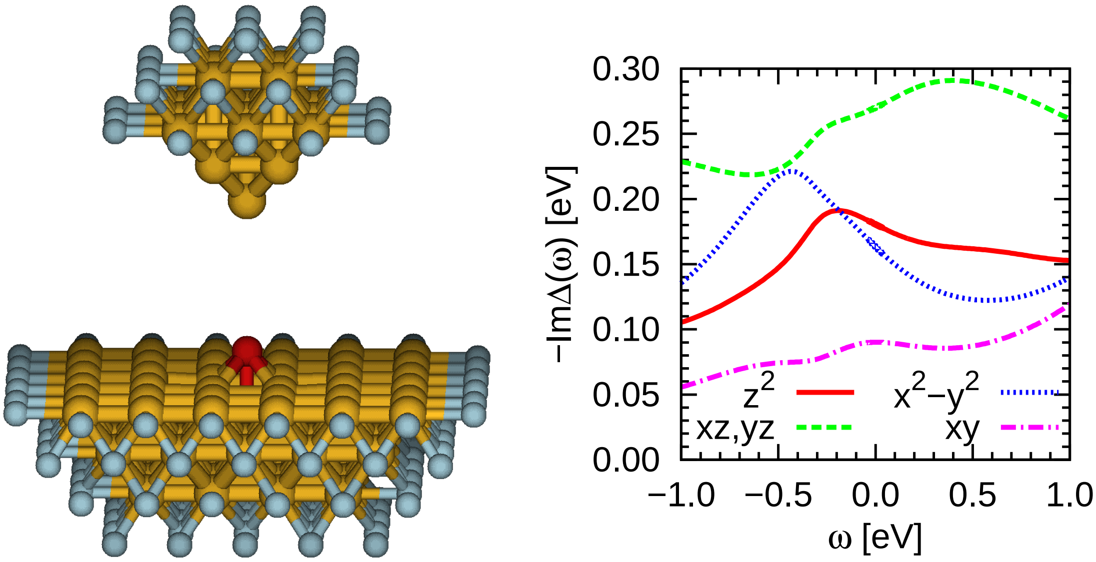

Figure 7: Left: geometry of the Co atom deposited on a Cu(001) surface; dark gray/red: Co, gray/yellow: Cu, light gray/blue: Bethe lattice. Right: imaginary part of the hybridization function for the Co $3d$ shell.

the (001) direction, also embedded into a Bethe lattice. The tip is placed directly above the Co atom at a distance of 6 Å, so that the system is in the tunneling regime.

As explained in Sec. 2.4, we now compute the hybridization functions of the Co $3d$ orbitals (see right panel of Fig. 7). The four-fold symmetry of the Cu(001) surface leads to a splitting into four groups. The xz and yz orbitals are degenerate (in the following, the results for the yz orbital are omitted) and exhibit the strongest hybridization at the Fermi level. This can be explained by the orbital orientation: Two lobes of the xz and yz orbitals point directly at the two underlying surface atoms along the x and y axis, respectively. The hybridization functions of z^2 and x^2-y^2 have comparable values around the Fermi level. Although one lobe of the z^2 orbital points directly towards the surface, it does not point directly at any of the neighboring atoms, but at the hollow space in between them. The x^2-y^2 orbital is oriented in the x-y plane, but its lobes point exactly in the horizontal direction of the four neighboring atoms. The xy orbital has the lowest hybridization in the displayed energy window. It is oriented in the x-y plane, and its lobes point at the hollow spaces between the four neighboring atoms. All hybridization functions show a moderate energy dependence. Note that the hopping between different Co $3d$ orbitals is zero, i.e. they do not couple to each other on the single-particle level. While the hybridization function is calculated *ab initio*, the Coulomb interaction U is used as a parameter that allows us to tune the Kondo coupling strength and explore the effect of the width of the Kondo peak on the transmission line shape. But in order to have an estimate of the magnitude, we have also calculated U *ab initio* for each of the d orbitals by constrained RPA calculations as described in chapter 4. We find values for U ranging from 1.8 eV to 2.6 eV[194]. Accordingly, we choose the U parameters to vary between 2 eV and 3 eV. The hybridization

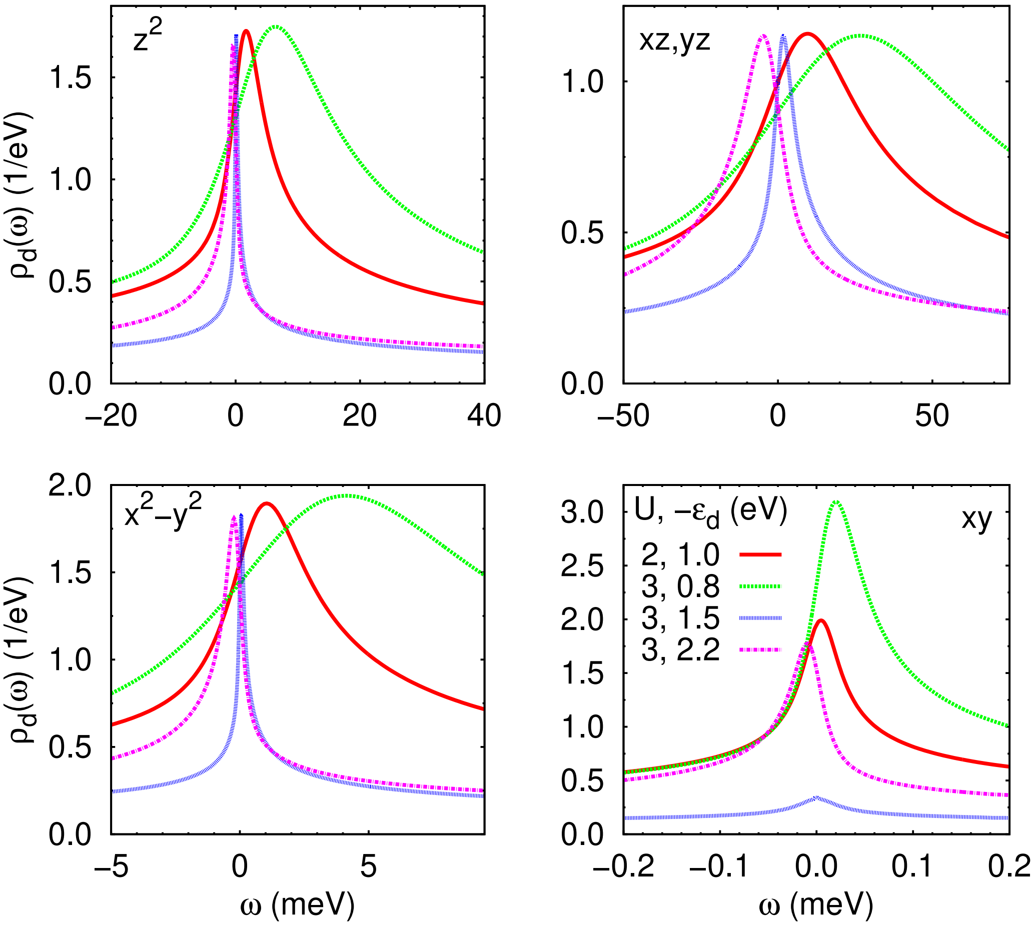

Figure 8: Impurity spectral functions for d orbitals of Co@Cu(001) for different Anderson impurity model parameters U, ϵ_d.

functions from Fig. 7 together with the energy level ϵ_d and the effective Coulomb interaction U define an sAIM which is solved in the OCA[163].

Fig. 8 shows impurity spectral functions $\rho_d(\omega)$ of different d orbitals for different values of the AIM parameters ϵ_d and U. The z^2, xz, yz and x^2-y^2 orbitals behave similarly. For $\epsilon_d = -U/2$ (red solid and blue dotted curves) we have approximate particle-hole symmetry: the Kondo peak is nearly symmetric and centered close to, but slightly above the Fermi level. Note that exact particle-hole symmetry is not achieved because of the non-constant hybridization function. As expected, when U is increased the Kondo temperature and hence the width of the Kondo peak decrease strongly, according to $T_\mathrm{K} \propto \mathrm{e}^{-U/-\mathrm{Im}(\Delta)}$[144]. On the other hand detuning the system from particle-hole symmetry by shifting ϵ_d leads to a strong increase of the Kondo temperature due to charge fluctuations (green dashed, magenta dashed-dotted curves). Note the different Kondo scales for each orbital due to different hybridization strengths. Also note that the peak height is nearly the same for each orbital. In the ideal case of a flat hybridization $\Gamma = -\mathrm{Im}(\Delta)$, the height of the Kondo peak is simply given by $1/(\pi\Gamma)$. Slight deviations from identical height can be explained by the non-constant hybridization functions (see Fig. 7). The situation is different for the xy orbital, which has the lowest hybridization of the d orbitals,

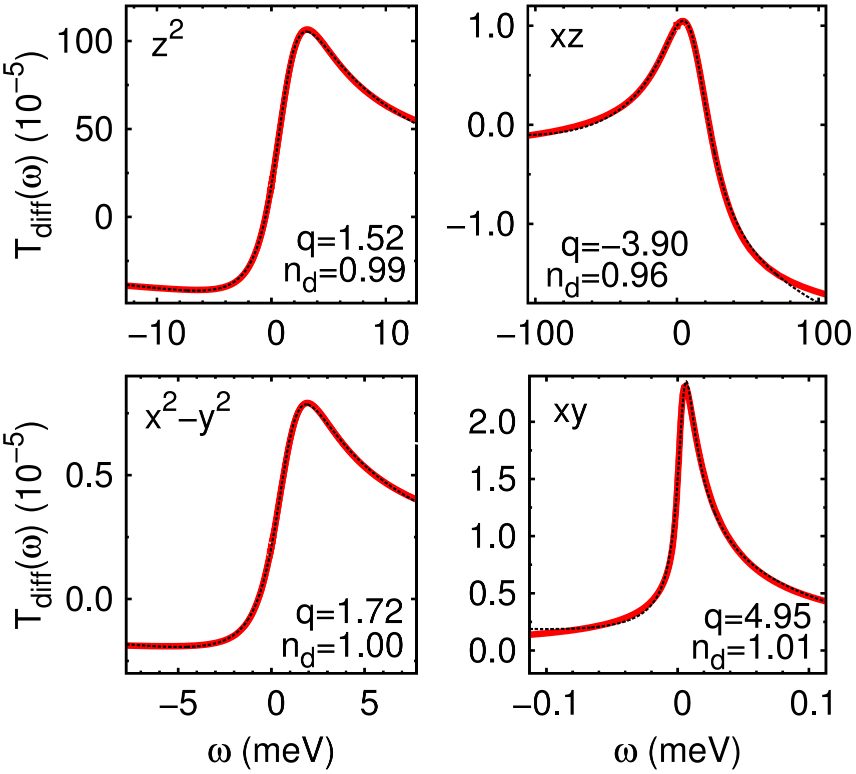

Figure 9: Transmission functions for different d orbitals of Co@Cu(001). Coulomb repulsion $U = 2$ eV, and energy level $\epsilon_d = -1$ eV (approximate particle-hole symmetry). The red continuous curves show the calculated transmission, the black dashed curves Fano-Frota fits. The transmission background has been subtracted[195].

and, correspondingly, the lowest Kondo temperature. It is so low that our calculation, due to numerical limitations, cannot reach temperatures low enough, and the shown Kondo peaks are not fully developed yet.

We now calculate the correlated transmission functions for Kondo peaks in different d orbitals. Fig. 9 shows transmission line shapes for different d orbitals for $U = 2$ eV and $\epsilon_d = -1.0$ eV. In order to make the features more clearly visible, here and in the following the transmission background was subtracted[195]. We find that the line shapes are indeed different for each orbital: We observe approximately antisymmetric Fano line shapes ($q \approx 1$) for z^2 and x^2-y^2, and more peak-like feature ($q \gg 1$) for xz and xy. In order to quantitatively describe the line shapes, we perform Frota fits to determine the q parameter and width of the line shapes, as explained before in Sec. 3.1. The z^2 and x^2-y^2 orbitals have comparable q values of 1.52 and 1.72, respectively. For xz, q becomes negative (-3.9) and for xy we find the most pronounced peak with $q = 4.95$. The widths of the Fano features differ significantly, and in accordance with their hybridization strength at the Fermi level, again according to $T_\mathrm{K} \propto \mathrm{e}^{-U/-\mathrm{Im}(\Delta)}$. Note that a feature with a very small width, as e.g., in the case of xy, might never be observed in an actual experiment, because of the Kondo temperature being much too low and because of limited resolution.

We now vary the Coulomb repulsion U and introduce charge fluctuations by shifting the d level position ϵ_d, as can be seen in Fig. 10. When varying U, but maintaining particle-hole symmetry, the actual shape of the transmission features is only weakly affected, while the widths of the features change strongly, as has already been seen and discussed for the spectral functions in Fig. 8. When introducing charge fluctuations, the Kondo peak becomes asymmetric (see Fig. 8). This asymmetry is also reflected in the transmission line shapes. We find that the q parameter consistently increases when ϵ_d is shifted downwards. For positive q (z^2, x^2-y^2, xy) lowering ϵ_d makes the line shapes more peak-like, while for negative q (xz), lowering ϵ_d leads to more dip-like line shapes.

Hence, while the choice of AIM parameters U and ϵ_d does affect the transmission line shapes to some degree, it does not completely change its symmetry. For example, the sign of the q factor does not change.

While the signal width is determined by the hybridization and choice of AIM parameters exclusively, the signal amplitude decisively depends on the system geometry. Because we chose the z axis as our transport direction, a Kondo peak in the z^2 orbital results in a much more dominant feature compared to the remaining d orbitals, as can be seen in Figs. 9 and 10. Hence, if there is a Kondo peak in the z^2 orbital, the corresponding Fano feature will dominate in the transmission regardless of what happens in the other orbitals. Also Fano features due to Kondo peaks in orbitals other than the z^2 orbital might be difficult to discern from the background if the background dispersion is strong compared to the Fano amplitudes. This statement remains true even if the STM tip is shifted laterally by moderate distances of a few Å. Although tunneling into orbitals other than z^2 becomes more favorable upon a lateral shift of the tip, the feature due to the Kondo peak in the z^2 remains the most dominant one.

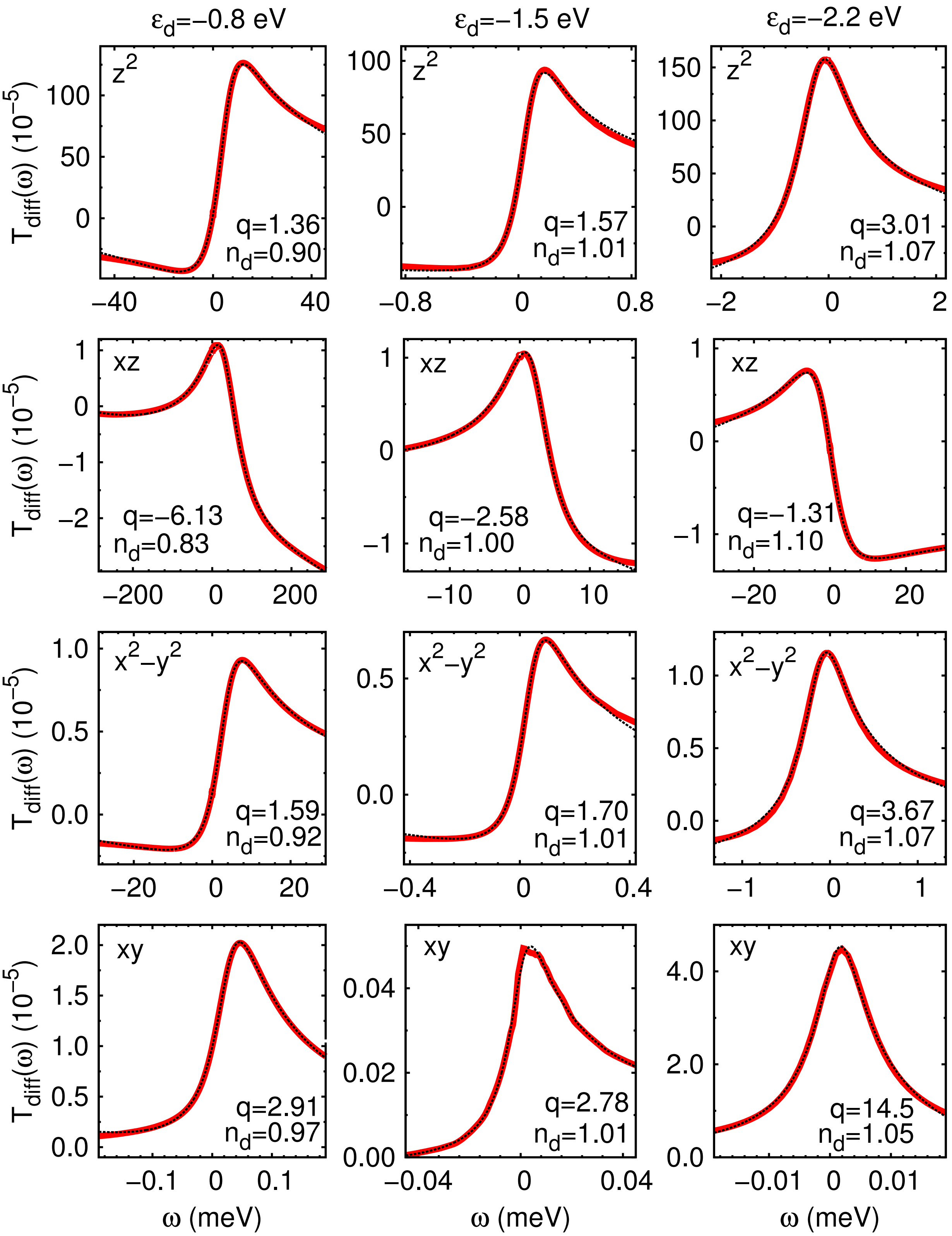

Figure 10: Transmission functions for different d orbitals of Co@Cu(001). The Coulomb repulsion is $U = 3$ eV, the occupation is varied by shifting ϵ_d. The red continuous curves show the calculated transmission functions, the black dashed curves the corresponding Fano-Frota fits. The transmission background has been subtracted.[195]

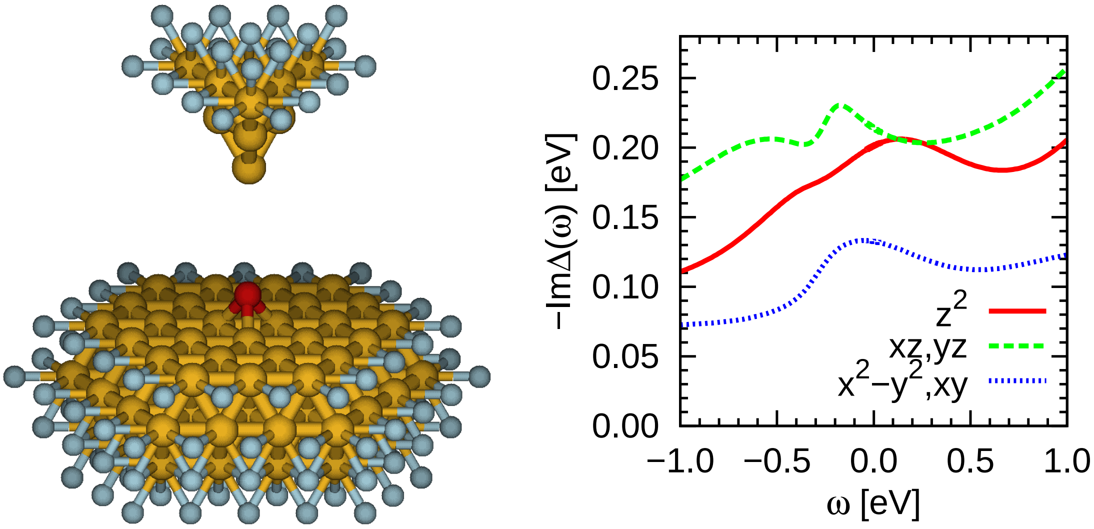

Figure 11: Left: geometry of the Co atom deposited on a Cu(111) surface; dark gray/red: Co, gray/yellow: Cu, light gray/blue: Bethe lattice. Right: imaginary part of the hybridization function of the Co $3d$ shell.

3.4 Co adatom on Cu(111) surface

The next system we focus on is a Cobalt atom, deposited at the 'hcp' hollow site of a Cu(111) surface, as can be seen in the left panel of Fig. 11. The surface is modeled by three Cu slabs of 27, 37 and 27 atoms, respectively, which are connected to a Bethe lattice. The tip is described by a Cu(111) pyramid, consisting of 10 copper atoms, also connected to a Bethe lattice. The threefold symmetry splits the five orbitals of the Co $3d$ shell into three groups: the non-degenerate z^2 orbital ($m = 0$) and two doubly degenerate groups, one with $m = \pm 1$ (xz and yz orbitals) and one with $m = \pm 2$ (xy and x^2-y^2 orbitals). The right panel of Fig. 11 shows the hybridization functions for each of the three groups. The group with the xz and yz orbitals exhibits the strongest hybridization at the Fermi level. Two of their lobes point towards the underlying atoms. The z^2 orbital hybridizes slightly less with the rest of the system. Although one of its lobes points directly at the surface, it points into the hollow space between the three underlying atoms. The group with the x^2-y^2 and xy orbitals show the weakest hybridization, since they are oriented in the x-y plane.

Fig. 12 shows impurity spectral functions $\rho_d(\omega)$ of different d orbitals for different values of the AIM parameters ϵ_d and U. They behave similarly to those of the Co@Cu(001) system: high hybridization, low U values and introducing charge fluctuations by shifting ϵ_d away from particle-hole-symmetry lead to higher Kondo temperatures. For the x^2-y^2 and xy orbitals, the Kondo temperature is relatively low, so that the Kondo peak for $U = 3$ eV and $\epsilon_d = -1.5$ eV is not fully developed for the minimum calculation temperature that we could reach for numerical reasons.

We proceed as described in the previous section and calculate transmission functions for the

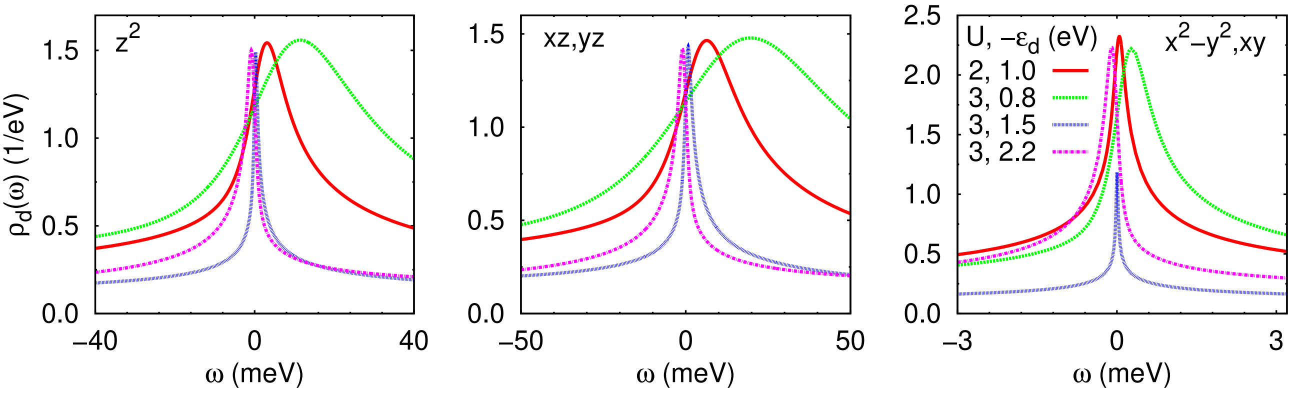

Figure 12: Impurity spectral functions for d orbitals of Co@Cu(111) for different Anderson impurity model parameters U, ϵ_d.

d orbitals of Co@Cu(111), assuming a Coulomb repulsion of $U = 2$ eV and (approximate) particle-hole-symmetry with $\epsilon_d = -1.0$ eV (Fig. 13). Again, we find different line shapes for each orbital. The z^2 orbital gives the most peak-like transmission feature with $q = 2.77$. For x^2-y^2 we observe a transmission peak with $q = -2.44$. The xz orbital results in a Fano-type feature with $q = -1.61$. The widths of the transmission features differ considerably, with the xz and yz orbitals having the largest width, and the xy and x^2-y^2 orbitals the lowest. The z^2 orbital again has the highest signal amplitude, as it strongly couples to the tip conduction electrons.

In Fig. 14, we present calculated line shapes for different AIM parameters U and ϵ_d. We observe a similar behavior as for Co@Cu(001). When staying in the particle-hole symmetric case and increasing U (middle column of Fig. 14), the line shapes remain similar, with slightly increased q values. We introduce charge fluctuations by shifting the position of ϵ_d (left and right column

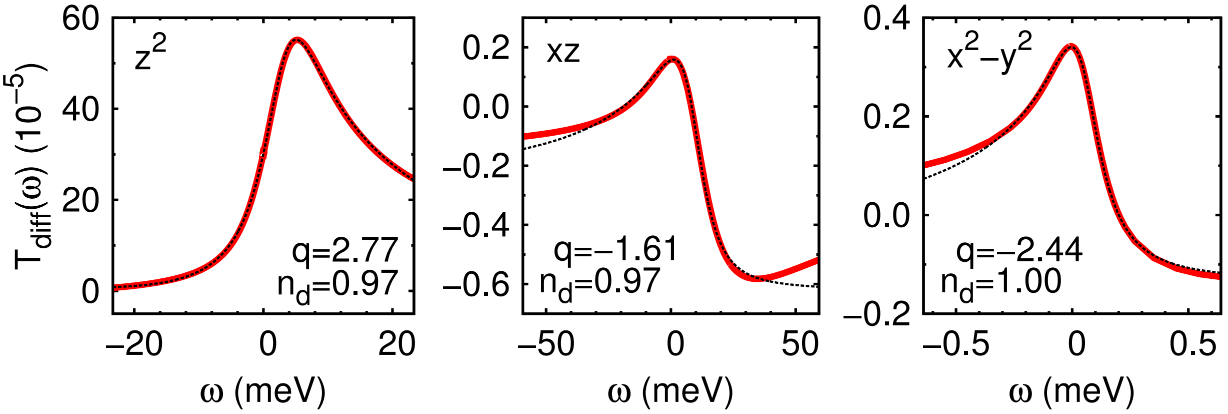

Figure 13: Transmission functions for different d orbitals of Co@Cu(111). Coulomb repulsion $U = 2$ eV, $\epsilon_d = -1.0$ eV. The red continuous curves show the calculated transmission functions, the black dashed curves the corresponding Fano-Frota fits. The transmission background has been subtracted.[195]

of Fig. 14). The q parameter increases when moving ϵ_d to lower energies. For positive q values, as for z^2, this leads to more peak-like line shapes, while for negative q values, as for xz and x^2-y^2, it leads to more Fano- or dip-like line shapes. The only exception to this behavior occurs for the xz orbital, for $U = 3$ eV and $\epsilon_d = -0.8\ eV$. It has a very high Kondo temperature and an equivalently wide Fano feature, and the Fano-Frota fit fails for negative energies. This suggests that the Fano line shape overlaps with other transmission features that alter the final line shape.

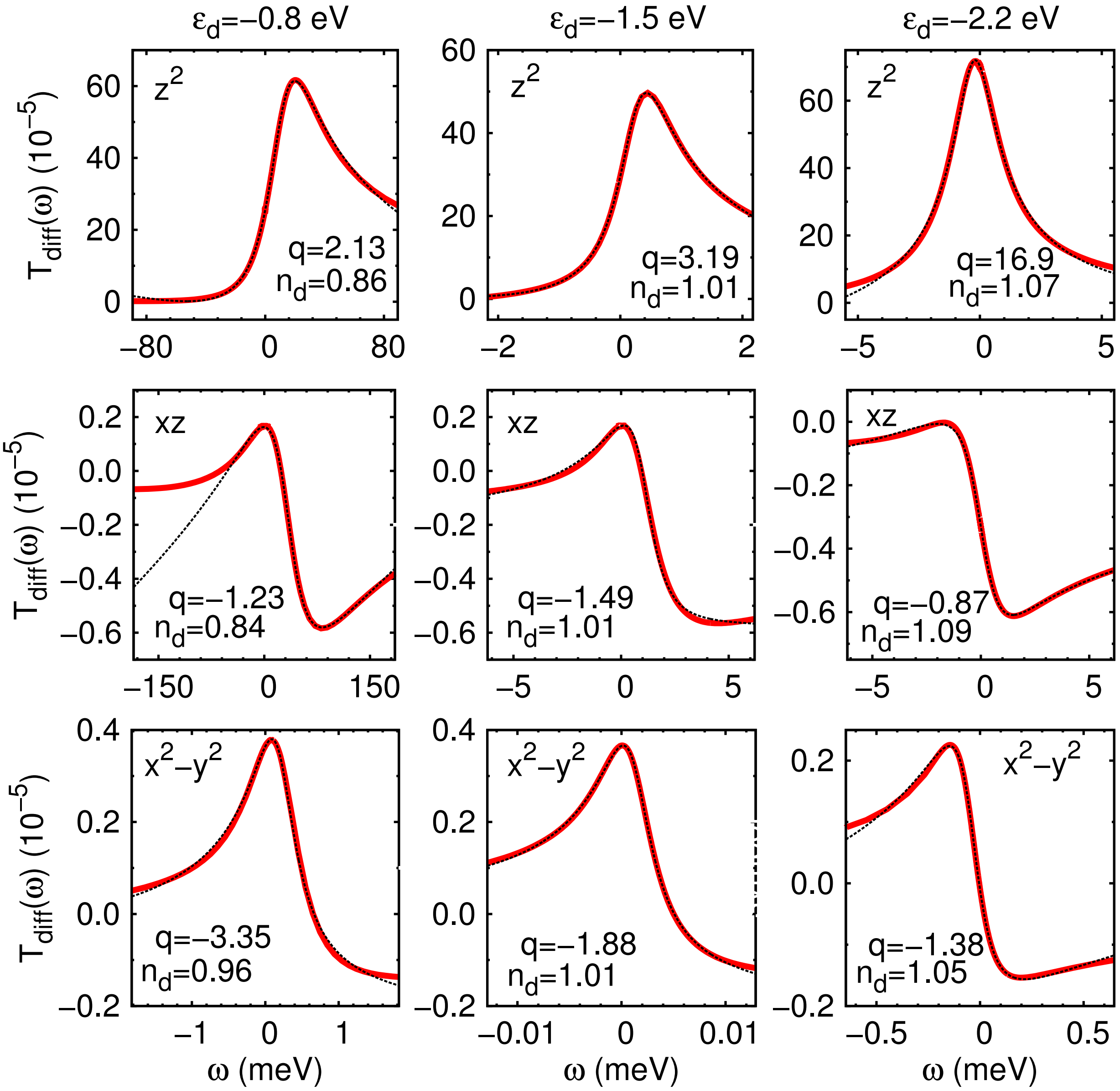

Figure 14: Transmission functions for different d orbitals of Co@Cu(111). The Coulomb repulsion is $U = 3$ eV, the occupation is varied by shifting ϵ_d. The red continuous curves show the calculated transmission, the black dashed curves Fano-Frota fits. The transmission background has been subtracted.[195]

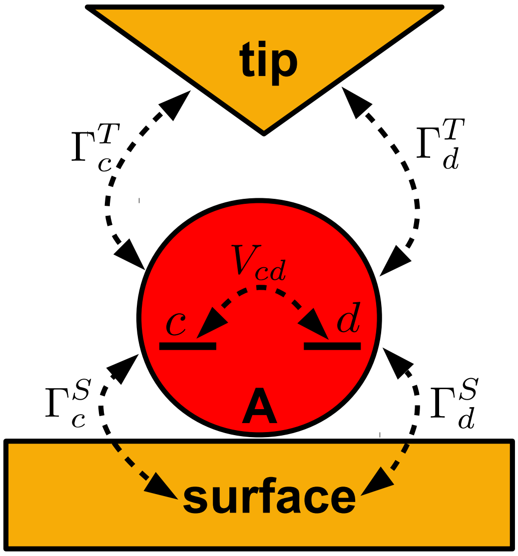

Figure 15: Sketch of the simplified model. The effective atom A is described by the correlated d level and one conduction electron level c, in contact with the surface and the tip.

3.5 A simplified model

The interference mechanism leading to different Fano line shapes still is a matter of discussion[62;63;64;68;175;176;177;178;196;196;197]. We expand on this discussion by introducing a simple model that allows us to determine transmission line shapes from *ab initio* parameters. Fig. 15 shows a schematic drawing of our model system. The central assumption is that the quantum interference primarily occurs *on* the magnetic adatom, namely between one s-type and/or p-type level (in the following, we will simply call it the conduction level c) and the correlated d level. Both levels are in contact to the tip (electrode L) and the surface (electrode R), and the respective interactions are taken into account by coupling matrices $\Gamma_{\mathrm{L/R}}$. As a second central assumption we neglect the direct tunneling from the tip to the surface.

The starting point of our model is the correlated Green's function of the effective atom comprising the conduction c level and the correlated d level of the magnetic atom.

$$G_{\mathrm{A}}(\omega) = \left(\omega\hat{P}_{\mathrm{A}} - \hat{H}_{\mathrm{A}} - \hat{\Delta}(\omega) - \Sigma_d(\omega)\hat{P}_d\right)^{-1}$$
$$= \begin{pmatrix} \omega - \epsilon_c - \Delta_c(\omega) & -V_{cd} - \Delta_{cd}(\omega) \\ -V_{dc} - \Delta_{dc}(\omega) & \omega - \epsilon_d - \Delta_d(\omega) - \Sigma_d(\omega) \end{pmatrix}^{-1} \tag{95}$$

$\hat{P}_{\mathrm{A}}$ is a projector onto the effective atom A, while $\hat{P}_d$ projects onto the d level only. All parameters can either be extracted from the KS-calculation (ϵ_d, ϵ_c, V_{cd}, $\hat{\Delta}(\omega)$) or from the OCA-calculation ($\Sigma_d(\omega)$), while the chemical potential has been set to zero $\mu = 0$. The diagonal elements of the hybridization function $\hat{\Delta}(\omega)$ lead to a shift (real part) of the level position of ϵ_c and ϵ_d, respectively, and yield an effective level broadening (imaginary part). Also note that the hybridization function has off-diagonal components $\Delta_{cd}(\omega) = \Delta_{dc}(\omega)$, which can be

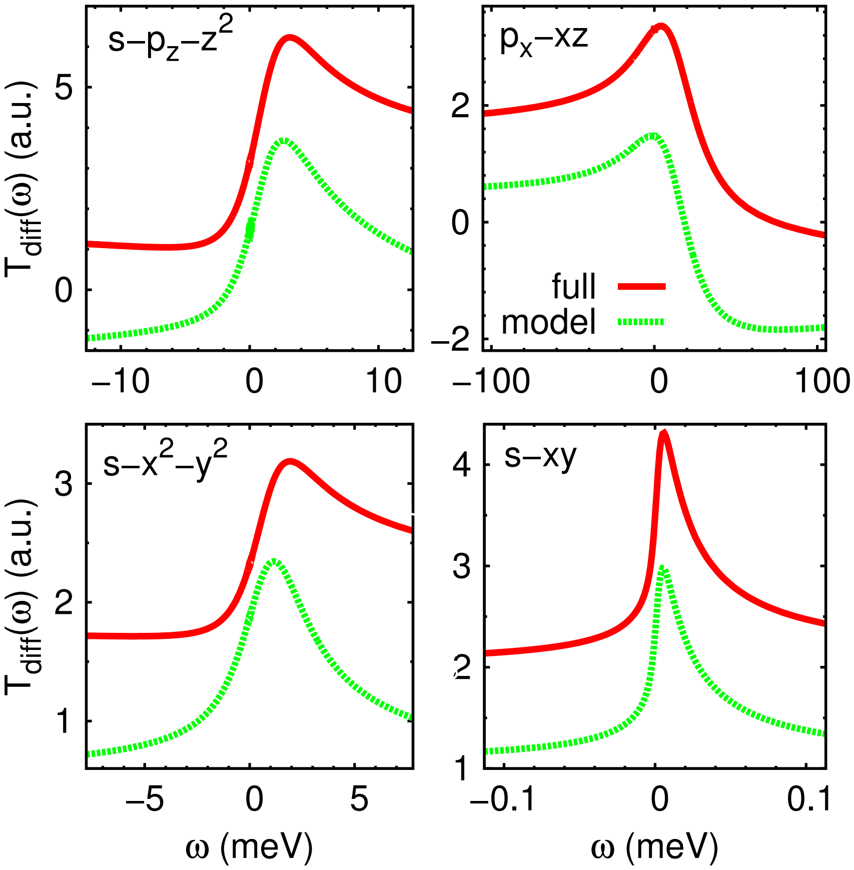

Figure 16: Transmissions calculated *ab initio* with the ANT.G package (see Sec. 3.3) and for the simplified model; Co@Cu(001), $U = 2$ eV, $\epsilon_d = -1$ eV. The transmission functions are rescaled and offset for better visibility.

understood as an additional hopping between the c and d level mediated by hoppings via the substrate, to give a total effective coupling of $\tilde{V}_{cd} = V_{cd} + \Delta_{cd}$. The coupling matrices $\Gamma_{\mathrm{L/R}}(\omega)$ necessary for calculating the transmission function by Eq. 68 can be obtained by decomposing the hybridization function into a tip ($\Delta_{\mathrm{L}}(\omega)$) and a surface ($\Delta_{\mathrm{R}}(\omega)$) component and taking the imaginary parts, i.e. $\Gamma_{\mathrm{L/R}}(\omega) = -2\,\mathrm{Im}[\Delta_{\mathrm{L/R}}(\omega)]$.

For the conduction level c of the effective atom we choose the s or p orbital that couples to the correlated d orbital. The z^2 orbital couples to both the s and the p_z orbital for the (001) and the (111) substrates. In this case we apply a unitary transformation in the subspace of the s and p_z orbitals such that the z^2 orbital decouples completely from one of the orbitals in the new basis. The sp_z hybridized orbital coupling to the z^2 is then found to be the linear combination $|sp_z\rangle \propto \tilde{V}_{sz^2}|s\rangle + \tilde{V}_{p_zz^2}|p_z\rangle$ where $\tilde{V}_{sz^2}$ and $\tilde{V}_{p_zz^2}$ are the effective hoppings of the z^2 orbital with the s and p_z orbitals, respectively. On both surfaces, the xz orbital couples to p_x and the yz orbital to p_y. For the (001) surface both the x^2-y^2 and the xy orbitals do not interact with any of the s or p orbitals of the atom, while on the (111) surface, they do interact with the p_y and p_x orbitals, respectively.

In Fig. 16 and 17, we compare line shapes calculated for the simplified model with the full

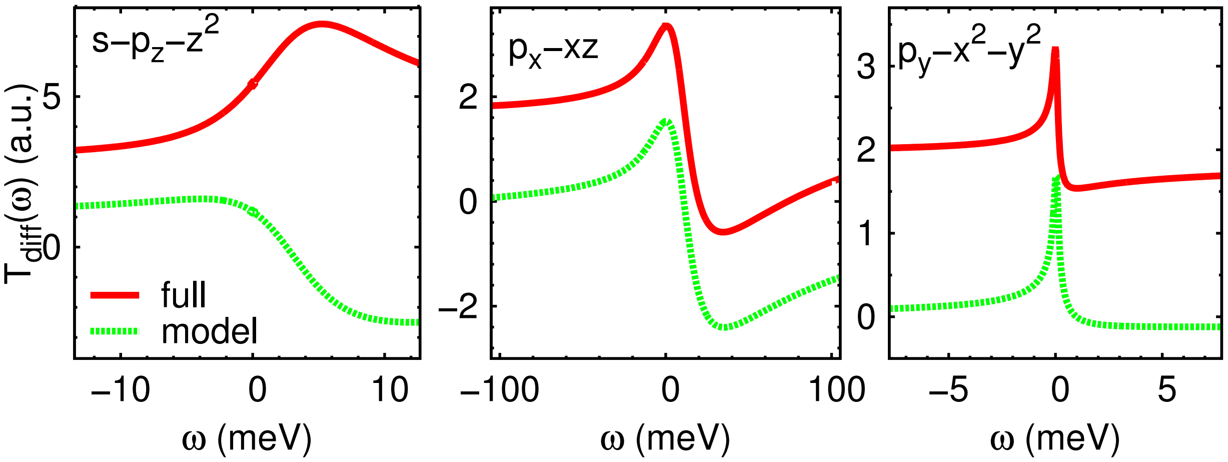

Figure 17: Transmissions calculated *ab initio* with the ANT.G package (see Sec. 3.4) and for the simplified model; Co@Cu(111), $U = 2$ eV, $\epsilon_d = -1$ eV. The transmission functions are rescaled and offset for better visibility.

ab initio results from Sec. 3.3 and Sec. 3.4. For the Co@Cu(001) surface (see Fig. 16), the simplified model consisting of the z^2 orbital and the sp_z hybridized orbital reproduces the line shape of the z^2 orbital quite well. Only the peak character is slightly overestimated. In the case of the xz orbital the line shape of the simplified model including the p_x orbital is in excellent agreement with that of the full *ab initio* calculation. For the x^2-y^2 orbital the agreement between the simplified model and the full calculation is not as good. As stated before this orbital does not interact with any s or p orbital on the Co atom. Hence the transmission of the simplified model reproduces simply the Kondo peak in the spectral function since no interference is taking place. On the other hand the full transmission shows a somewhat asymmetric Fano feature ($q \approx 1.7$) indicating that interference with some substrate state(s) must take place, which is not included in the model. Finally, for the xy orbital we find very good agreement between the simplified model and the full calculation. The line shape in both calculations simply reproduces the Kondo peak in the spectral function of the xy orbital indicating the absence of any interference effects between this d level and s and p levels on the atoms as well as substrate states.

We find a somewhat similar picture for Co@Cu(111) (see Fig. 17). For the xz orbital the model including the interaction with the p_x orbital gives a line shape in excellent agreement with the full calculation. Also for the x^2-y^2 the simplified model including the p_y orbital on the atom reproduces the line shape of the full calculation very well. However, in the case of the z^2 orbital the simplified model including the sp_z hybridized orbital fails quite badly in reproducing the line shape of the full calculation. Apparently, interference with tunneling paths to substrate states play an important role here.

3.6 Discussion

For Co@Cu(001), we found transmission line shapes ranging from asymmetric Fano features with positive (z^2, x^2-y^2) and negative (xz) q values to a more peak-like feature (xy). The line shapes are determined by the interference of different tunneling paths. Our simplified model calculations indicate that for z^2 and xz the interference takes place on the adatom between the correlated d level and the non-interacting sp levels coupling to the d orbital. For the xy orbital, no interference occurs between the conduction and impurity tunneling channels. Hence one directly observes the shape of the Kondo peak in the transmission. On the other hand, for the x^2-y^2 orbital, the interference mechanism probably involves the Cu substrate states which are not captured by the simplified model. Experimentally, asymmetric Fano line shapes were reported with $q \sim 1.1 - 1.2$ in the tunneling regime[32;38]. The measured line shapes are comparable to the features we found both in the z^2 and x^2-y^2 orbitals (see Figs. 9 and 10), although the z^2 orbital yields a slightly better agreement. Better agreement with experiment can surely be achieved by adjusting the Anderson model parameters and fitting the calculated spectra with the experimental ones. We would like to stress though that finding good agreement with experiment is not the primary goal of this chapter, but rather to demonstrate how different orbital symmetries give rise to different Fano-Kondo line shapes. A recent study[70] found an underscreened Kondo effect for Co@Cu(001), where the z^2 and x^2-y^2 are nearly half filled, but only the z^2 orbital is Kondo screened at finite temperatures due to its higher Kondo temperature. Ref. [69] comes to similar conclusions, finding a Kondo peak in the z^2 orbital with $q = 1.2$ in the tunneling regime and explaining it due to the interference of the z^2 with the s orbital.

For Co@Cu(111), we found asymmetric to peak-like Fano line shapes with positive (z^2) and negative (xz, x^2-y^2) q values. For the latter two, we can understand the tunneling interference in terms of the model presented in the previous section. The interference occurs on the magnetic atom, between the conduction electron channel, modeled by one of the p orbitals, and the respective d level. For z^2, which is interacting with the sp_z hybridized level, our model fails, indicating that interference with substrate states plays an important role here.

Experimentally, dips were reported with q values close to zero[31;32;65] which does not seem to agree with any of the calculated line shapes. The z^2 orbital, aligned in the transport direction, again shows the strongest signal, but is rather peak-like. The closest candidate to a dip-like line shape is the xz orbital, particularly when increasing the occupancy relative to half-filling by moving the d level position downwards in energy (see Fig. 14).

Probably, the surface state of the Cu(111) surface[198] plays an important role for determining the line shape[31;64;68;199] since its tunneling amplitude may be twice as strong compared to tunneling into bulk states[200]. However, our embedded cluster calculation probably does not capture the surface state properly. The importance of the surface state for reproducing the correct line shape in the Co@Cu(111) system is also stressed in Ref. [69] where the surface state is not properly captured and the correct q value could not be reproduced either.

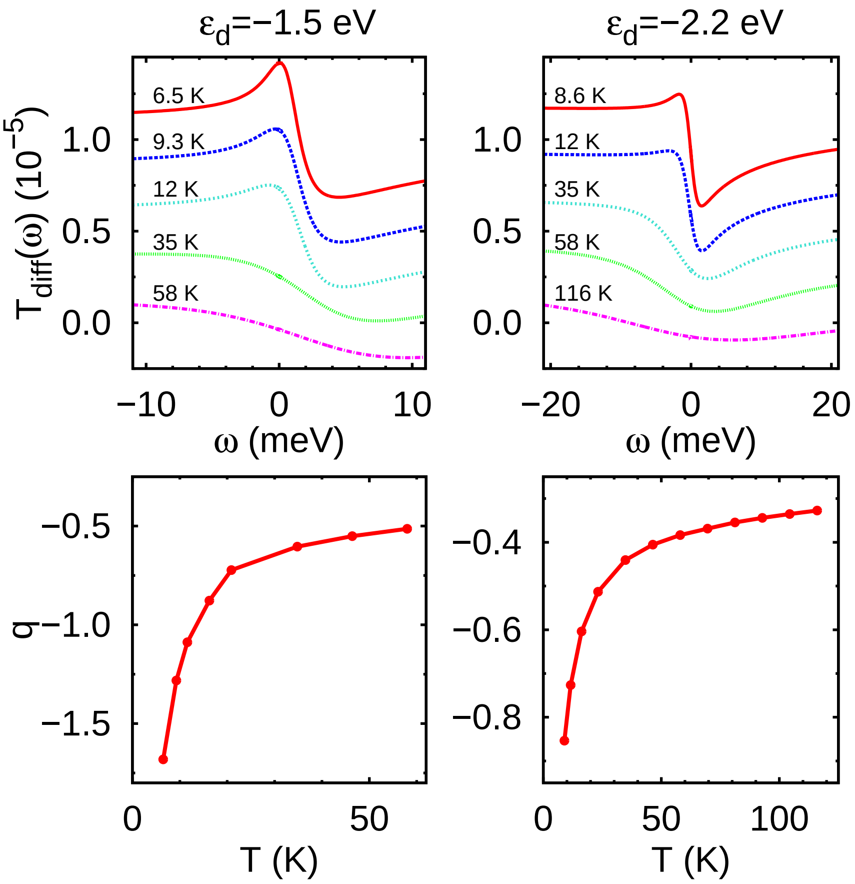

Figure 18: Temperature dependence of two different line shapes for Co@Cu(111), xz, $U = 3$ eV, $\epsilon_d = -1.5$ eV and $\epsilon_d = -2.2$ eV, respectively. Top: Transmission. Bottom: q parameter; the lines are a guide for the eye.

3.7 Temperature dependence

The results presented so far are for the case of $T \to 0$ (according to the criterion discussed in Sec. 3.2), and have been explained and discussed in terms of a simple model. We now study the temperature dependence of two line shapes: One tending towards a peak ($q > 1$) and one tending towards a dip ($q < 1$). We pick the xz orbital of Co@Cu(111), $U = 3$ eV, $\epsilon_d = -1.5$ eV ($q = -1.49$) and $\epsilon_d = -2.2$ eV ($q = -0.87$), respectively. The top row of Fig. 18 shows the evolution of the aforementioned two line shapes. For increasing temperature, the signal amplitude diminishes, while its width grows. The peak does not decay symmetrically. The 'peak' component of the Fano feature decays faster than the 'dip' component of the feature, so that, in both cases, the feature as a whole becomes increasingly dip-like with increasing temperature. In order to quantify that, we perform Fano-Frota fits and calculate the q parameter. We find that the absolute value of the q parameter decreases considerably when temperature is rising, irrespective if the feature tends more towards peak or dip in the $T \to 0$ case. This might also indicate that direct tunneling through the Kondo resonance becomes less important at higher temperatures, and the interference process involves substrate states at higher temperatures.

In this section, we studied the temperature dependence on the line shape, and found that they become increasingly dip-like when increasing the temperature. However, note that in our calculations for the xz orbitals we find $q < 0$ while in experiment q is always positive.

3.8 Moving the STM tip horizontally

So far, the STM tip was placed exactly on top of the adatom. In an STM setup, however, the STM tip can be placed at different locations above the surface. In this section, we investigate the dependence of the Fano line shapes on the horizontal position of the STM tip for the Co@Cu(001) surface. The z^2 and xz orbitals are chosen, since their line shapes could be explained in accordance to the simple model of Sec. 3.5. To this end, the STM tip is moved in the positive x direction in steps of 0.5 Å. The electronic structure calculation does not need to be redone, it suffices to keep the electronic structure of the tip fixed and move it accordingly with the tip atoms. This is possible due to the tunneling setup: Tip and surface orbitals do not overlap, and interactions between tip and surface are weak. The calculated transmission functions for movement in the positive x direction for the z^2 and the xz orbitals are shown in the top panels of Fig. 19.

For the z^2 orbital, the transmission curves have increasingly lower amplitudes when moving the STM away from the adatom, and the line shape changes considerably. For no or small tip displacements, the line shape is peak-like, becomes an asymmetric Fano line shape at $x = 1.5$ Å and increasingly more dip-like when moving the STM tip further away from the adatom, becoming a perfect dip at $x = 3.0$ Å. The q values and the amplitudes of the respective transmission curves were obtained by Frota fits according to Eq. 93. The results corroborate the qualitative description: The q value (middle row of Fig. 19) decreases continuously, until it reaches $q = 0$ at a displacement of $x = 3$ Å. The amplitude (bottom row of Fig. 19) also decreases continuously, but the decrease seems to slow down at high displacements.

For the xz orbital, the transmission curves behave differently: At first, the amplitude increases and reaches a maximum at $x = 2$ Å, then starts to decay when moving the tip further away. The line shapes also change: Peak-like at first, they become increasingly asymmetric Fano line shapes. This is also supported by the Frota fits: The q value increases at first and changes sign between $x = 0$ Å and $x = 0.5$ Å, then decreases (note that the corresponding ϕ_q changes monotonically), and remains roughly constant between $x = 1.5$ Å and $x = 3$ Å. The amplitude in fact decreases for a displacement of $x = 0.5$ Å, increases to a maximum at $x = 2$ Å to decrease again for further displacements.

These results can be explained in context of Sec. 3.5 and 3.6. A schematic drawing of the relevant orbitals is shown in Fig. 20.

For the z^2 orbital, the relevant tip orbital is the s orbital (and to a lesser extent the p_z orbital) of the tip. For no and low tip displacements, tunneling occurs directly with the z^2 orbital of the Co atom. For higher tip displacements, this interaction becomes increasingly smaller and almost vanishes for $x = 3.0$ Å, where the tunneling mostly occurs between the tip and the

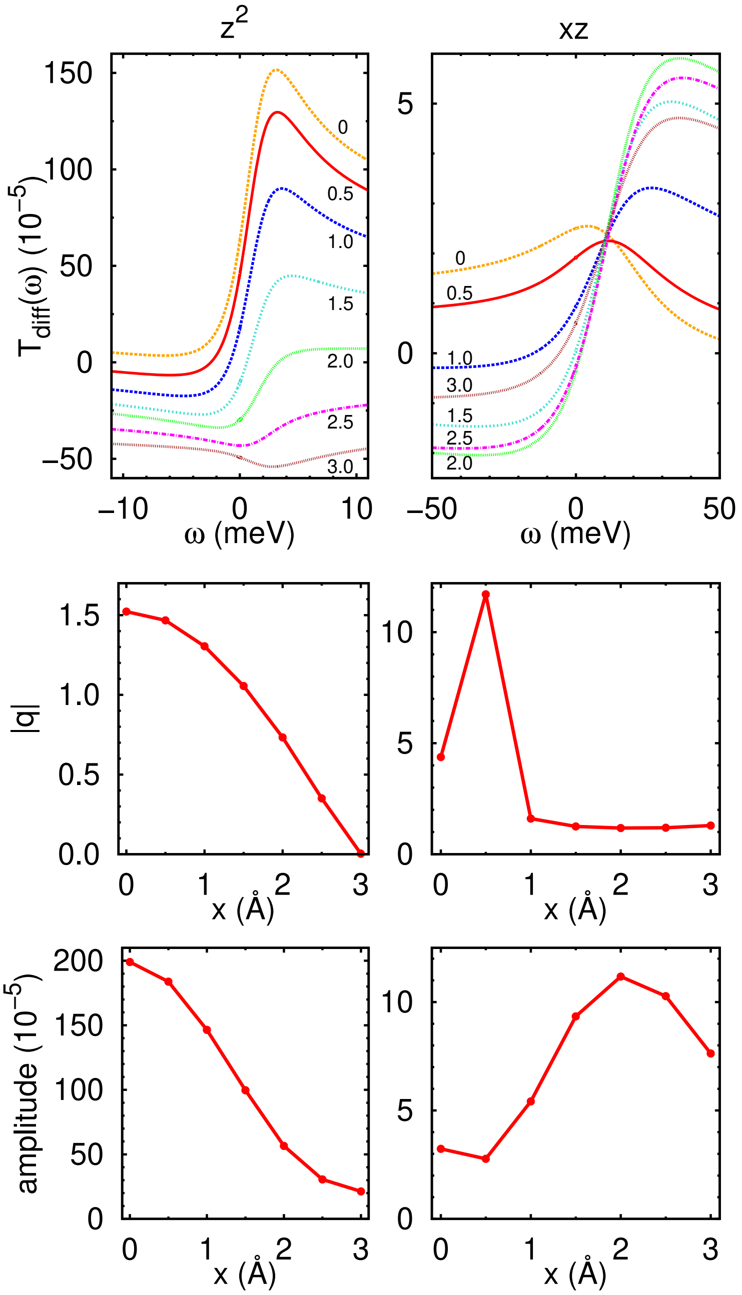

Figure 19: Top: transmission functions for the z^2 and xz orbitals, where the STM tip has been shifted along the x axis by the given distance in Å. The transmission functions are offset for better visibility. The transmission background has been subtracted[195] . Middle: q values for different displacements of the STM tip. Bottom: fitted amplitude for different displacements of the STM tip.

Cu surface, resulting in a dip (similarly to the dip experimentally observed for Co@Cu(111), which was explained in terms of tunneling into surface states as well). This also explains the saturation of the amplitude. When moving the tip in the y direction, the results remain the same: Due to the symmetry of the z^2 orbital within the x-y plane, the results of Fig. 19 are reproduced exactly. For the xz orbital, the relevant tip orbital is the p_x orbital when the STM

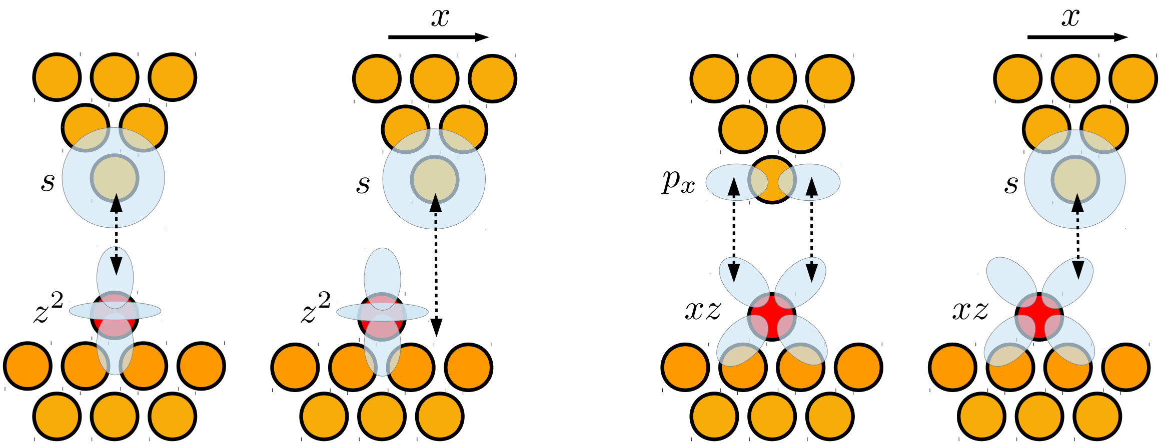

Figure 20: Schematic drawing of the orbitals involved in the interference process when the STM is moved horizontally, for the z^2 and xz orbitals of the Co adatom on the Cu(001) surface.

tip is placed directly on top of the adatom. When the tip is moved away, however, the coupling to the p_x orbital becomes smaller, explaining the slightly reduced transmission amplitude. For higher displacements, the s orbital starts to interact with the right lobe of the xz orbital of the adatom, reaching a maximum at $x = 2$ Å and decreasing for higher displacements. When moving the tip in the y direction, the results are different, and a simple decay of amplitude is observed as in the case of the z^2 orbital. The yz orbital moved in the y direction, however, behaves exactly like xz orbital when moving the tip in the x direction.

We see that the change of line shapes can be explained by the orbitals involved in the tunneling process. We also see that, depending on the d orbital where the Kondo effect occurs, the STS signal might be stronger if the STM tip is not placed directly on top of the adatom, but a few Å away from it.

3.9 Conclusions

In summary, we have calculated the orbital signatures of Kondo peaks in the STM spectra of transition metal adatom systems, namely Co@Cu(001) and Co@Cu(111). Our calculations show that the measured line shapes allow to draw some conclusions on the d orbital(s) involved in the Kondo effect since the line shape depends to a large extent on the coupling of the d orbital to the sp orbitals on the adatom, which in turn is determined by the orbital symmetry. However, also temperature, effective interaction U and in particular the occupancy of the d orbital have a strong influence on the actual line shapes. Also, if multi-orbital effects are important for the actual shape of a Fano-Kondo feature, this approach per se is not appropriate. Nevertheless, even in the case of a multi-orbital Kondo effect, often one orbital will be dominant in the tunnel spectra. In fact if a Kondo resonance forms in the z^2 orbital, the corresponding Fano feature will be dominant in the tunnel spectrum for the typical case of an s-type STM tip, so that Kondo features coming from other d orbitals are likely not visible. These results are also relevant for STS of transition metal complexes on metallic substrates[150;201;202], maybe even more so since tunneling into surface states is less important there.

We stress that the developed method can in principle also be applied to the contact regime. However, unlike in the tunneling case, in the contact regime the voltage can no longer be assumed to mainly drop between tip and adatom. Rather, the voltage drop will distribute in some way over the contact according to the actual geometry of the contact region[202], and needs to be calculated or estimated. Moreover, the actual contact geometry is probably also relevant for the coupling between d orbitals and conduction electrons and thus also has a strong influence on the line shapes. Therefore possible contact geometries need to be explored and relaxed with some care.

Based on our results, we propose a poor man's method to obtain information on the orbital(s) involved in the Kondo effect measured in an actual experiment solely on the basis of a density functional theory calculation of the system: by tailoring an appropriate self-energy for each orbital such that the width of the resulting Kondo peak in that orbital reproduces the width of the measured Fano-Kondo line shape, one can calculate the corresponding line shapes and compare to experiment.

4 The partially screened Coulomb interaction U

Screening is an essential concept to understand the physics of condensed matter systems, particularly metals. If a charge is inserted into a material, the surrounding electrons are subject to a changed potential and rearrange in order to minimize the total energy. This rearrangement can be relatively small (in the case of an insulator whose charges are bound) or very pronounced (in the case of a metal whose charge carriers can move relatively freely). In a metal, a screening cloud will form around the inserted charge. An electron far away from it does not feel the full Coulomb interaction of the inserted charge, but a reduced Coulomb interaction due to the screening[203].

Section 2.4.1 discussed how to obtain AIM parameters from the ab-initio transport calculation, but did not yet discuss how to obtain the interaction $U_{ik;jl}$ (short notation U). It is much smaller than the bare interaction V, since it already takes into account all screening contributions from outside of the correlated region, but not the screening within the correlated region itself. U is a partially screened interaction, where the screening within the correlated region is taken care of when solving the AIM. It initially appeared in the context of model Hamiltonians, particularly the Hubbard model[204], and is still commonly used in electronic structure theory.

Various methods have been proposed to compute the interaction U from a DFT calculation, and whose results may deviate significantly from each other[43]. The first connections between DFT calculations and the U parameter were made by Gunnarsson et. al.[205]. Their approach, often labelled constrained LDA, keeps the orbital occupation of the localized orbitals fixed, and determines the interaction U as the second derivative of the total energy with respect to the occupancy of the localized level. Another constrained DFT-approach was given by Pickett[206] and extended by Cococcioni[207], which is also called linear-response method[43], and relates the interaction U to the linear response function. These methods were often used in the context of (self-consistent) LDA+U, or, more generally, DFT+U[207;208;209].

The random phase approximation[210;211;212;213] (RPA) is another possibility to compute the partially screened Coulomb interaction U. Its basic idea is to only take into account screening contributions due to the formation of electron-hole-pairs. The RPA's first use in this context was the computation of the fully screened interaction W[193;214;215]. The constrained RPA (cRPA) was first introduced by Aryasetiawan[216;217] in order to compute the partially screened interaction U and has since been extended and applied in different contexts and for different classes of materials[70;218;219;220;221;222;223;224;225;226]. While constrained DFT should yield similar results as the cRPA, the latter was shown to provide more reliable results due to technical difficulties in the implementation of the constrained LDA[217].

This thesis therefore combines the cRPA methodology with our finite-cluster DFT calculation in order to obtain partially screened Coulomb interactions for our systems, following the method and notation of Ref. [70]. The focus will lie on the Co@Cu(001) system.

This chapter proceeds as follows: first, the cRPA-methodology is presented. The influence of different DFT functionals and differently sized polarization regions will be investigated. Self-consistent LDA+U and PBE+U calculations are performed and discussed. Two attempts to approximately include polarization effects from outside of the polarization region are proposed, and the chapter finishes with a discussion of the results.

4.1 The constrained random phase approximation

In this chapter, the starting point of the cRPA will be the bare Coulomb interaction V and the non-interacting KS GF $G^0_\mathrm{D}(\omega)$ of a converged DFT calculation (in Sec. 5.3, the starting point will be the interacting GF), after the ANT.G[127] self consistency presented in the previous chapter is achieved (see Fig. 6). The RPA assumes that screening occurs exclusively due to the formation of electron-hole-pairs. Due to computational limitations, it is typically not possible to take into account the screening from the complete device region D if the device is reasonably large. Instead, a smaller polarization region P is defined (see Fig. 1), consisting of the correlated subspace C itself and the surrounding atoms. This approximation can be justified by the fact that the orbitals that span region C are typically strongly localized, and the most relevant screening contributions are mostly local as well.

For a stationary Hamiltonian, the Dyson equation for the screened interaction can be written as:

$$W_{\alpha_1\beta_1;\alpha_2\beta_2}(\tau) = V_{\alpha_1\beta_1;\alpha_2\beta_2}\,\delta(\tau) + \sum_{\mu_1\nu_1\mu_2\nu_2} V_{\alpha_1\beta_1;\mu_1\nu_1} \int_0^\beta \mathrm{d}\tau\,(\Pi_\mathrm{P})_{\mu_1\nu_1;\mu_2\nu_2}(\tau-\tau')W_{\mu_2\nu_2;\alpha_2\beta_2}(\tau'), \tag{96}$$

where τ is an imaginary time and only screening contributions from within the polarization region P are taken into account. The corresponding Feynman diagram is depicted in Fig. 21. This work only considers the static limit of the screened interaction $W^0 \equiv W(\omega = 0) = \int \mathrm{d}\tau\, W(\tau)$. To compute the static polarizability $\Pi^0 = \int_0^\beta \mathrm{d}\tau\,\Pi(\tau-\tau')$, one of the time arguments of $\Pi(\tau - \tau')$ can be set to $\tau' = 0$ due to the β-periodicity. Putting in the definition of the polarizability as a product of two GFs, given by the bubble diagram in Fig. 21, one obtains

$$\begin{aligned}
(\Pi^0_\mathrm{P})_{\mu_1\nu_1;\mu_2\nu_2} &= \int_0^\beta \mathrm{d}\tau\,(\Pi_\mathrm{P})_{\mu_1\nu_1;\mu_2\nu_2}(\tau) \\
&= \int_0^\beta \mathrm{d}\tau \sum_\sigma (G_\mathrm{P})^\sigma_{\nu_2\mu_1}(-\tau)(G_\mathrm{P})^\sigma_{\nu_1\mu_2}(\tau) \\
&= \frac{1}{\beta}\sum_{\mathrm{i}\omega_n}\sum_\sigma (G_\mathrm{P})^\sigma_{\nu_2\mu_1}(\mathrm{i}\omega_n)(G_\mathrm{P})^\sigma_{\nu_1\mu_2}(\mathrm{i}\omega_n) \\
&\overset{T\to 0}{=} \frac{1}{2\pi}\int_{-\infty}^{\infty} \mathrm{d}\omega \sum_\sigma (G_\mathrm{P})^\sigma_{\nu_2\mu_1}(\mathrm{i}\omega)(G_\mathrm{P})^\sigma_{\nu_1\mu_2}(\mathrm{i}\omega),
\end{aligned} \tag{97}$$

where in the third step, the Fourier transform with respect to imaginary time τ was carried out, and in the last step, the limit of $T \to 0$ was taken, turning the discrete sum over Matsubara frequencies ω_n into a continuous integral over the frequency ω. This gives the Dyson equation

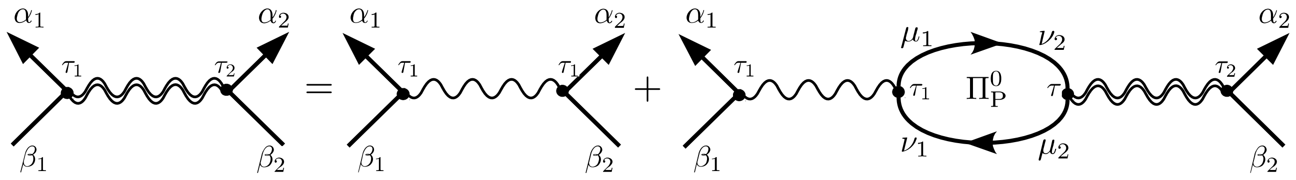

Figure 21: Feynman diagram of the Dyson equation from Eq. 98. The single and double wiggly lines correspond to the bare Coulomb interaction V and the screened Coulomb interaction W, repsectively. The RPA polarizability is represented by so-called bubble diagrams.

for the static screened interaction:

$$W^0_{\alpha_1\beta_1;\alpha_2\beta_2} = V_{\alpha_1\beta_1;\alpha_2\beta_2} + \sum_{\mu_1\nu_1\mu_2\nu_2} V_{\alpha_1\beta_1;\mu_1\nu_1} (\Pi^0_\mathrm{P})_{\mu_1\nu_1;\mu_2\nu_2} W^0_{\mu_2\nu_2;\alpha_2\beta_2}. \tag{98}$$

In order to write the Dyson equation for the screened interaction in a matrix equation, two indices can be merged into a superindex $I := (\alpha_1, \beta_1)$, $J := (\alpha_2, \beta_2)$, and the Dyson equation becomes:

$$\mathbf{W} = \mathbf{V} + \mathbf{V}\,\mathbf{\Pi}^0_\mathrm{P}\,\mathbf{W}. \tag{99}$$

The partially screened interaction $\mathbf{U}$ is calculated in a two-step process. First, the fully screened interaction $\mathbf{W}$ is obtained, by fully screening the bare interaction $\mathbf{V}$, taking into account all screening contribution from within the P subspace:

$$\mathbf{W} = \left(\mathbf{1} - \mathbf{V}\,\mathbf{\Pi}^0_\mathrm{P}\right)^{-1} \mathbf{V}. \tag{100}$$

As a second step, the screened interaction within the correlated subspace $\mathbf{W}_\mathrm{C}$ is partially unscreened, taking into account screening contributions from within the C subspace only:

$$\mathbf{U} = \left(\mathbf{1} + \mathbf{W}_\mathrm{C}\mathbf{\Pi}^0_\mathrm{C}\right)^{-1} \mathbf{W}_\mathrm{C}. \tag{101}$$

This yields the desired partially screened interaction $\mathbf{U}$. Note that the latter equation is numerically unstable[70], so particular care has to be taken in the computation of $\mathbf{\Pi}^0_\mathrm{C}$, since small inaccuracies can already lead to large deviations in the interaction $\mathbf{U}$. Also note that $\mathbf{U}$ depends on the DFT basis set, so the same basis set has to be used in subsequent calculations.
Note that the interaction $\mathbf{U}$ within the RPA could in principle be obtained in a single step by screening the bare Coulomb interaction $\mathbf{V}$ by all screening contributions within the polarization region P except for the contributions within the correlated region C[217]:

$$\mathbf{U} = \mathbf{V} + \mathbf{V}\left(\mathbf{\Pi}^0_\mathrm{P} - \mathbf{\Pi}^0_\mathrm{C}\right)\mathbf{U}, \tag{102}$$

which can be solved for the partially screened interaction

$$\mathbf{U} = \left(\mathbf{1} - \mathbf{V}\left(\mathbf{\Pi}^0_\mathrm{P} - \mathbf{\Pi}^0_\mathrm{C}\right)\right)^{-1} \mathbf{V}. \tag{103}$$

For computational reasons, it is more convenient to use the two-step process from above, particularly due to the use of non-orthogonal basis sets, where the correct choice of projection is crucial, and choosing the wrong projection will give unphysical results[70;227;228]. For a non-orthogonal basis set, $\mathbf{\Pi}^0_{\mathrm{C}}$ is not just a submatrix of $\mathbf{\Pi}^0_{\mathrm{P}}$. Details on non-orthogonal basis sets can be found in Appendix B.

The cRPA methodology calculates all elements of the partially screened Coulomb interaction $U_{ik;jl}$, but realistic impurity solver calculations only take into account a subset of elements, typically the direct Coulomb interaction $U_{ii;jj}$ and exchange interaction $U_{ij;ji}$. This will also be the case in chapter 5. Other elements are typically small, the discussion in this chapter will therefore refer to the direct and exchange elements. More details on the quality of the results of an cRPA calculation can be found at the end of this chapter in Sec. 4.6.

4.2 U computed for different functionals

First, the influence of the DFT functional on the resulting U is investigated. The focus will be on the Co@Cu(001) system. An improved geometry for Co@Cu(001) has become available in the meantime[229], where the Co atom and the surrounding 4 Cu atoms were relaxed using the Vienna Ab initio Simulation Package[230] (VASP) and the PBE functional. Note that the new geometry is rotated by 45° compared to the geometry used in previous chapters. Due to that, xy and x^2-y^2 orbitals are interchanged, but all other system properties are unaffected by the rotation. The polarization region contains 10 atoms, namely the Co atom and the 9 closest Cu atoms (see Fig. 25). Calculations are performed for the LSDA and PBE functionals as standard KS-DFT functionals, and the range-separated hybrid functional HSE[99], LDA+U and PBE+U as generalized KS-DFT functionals (also see Sec. 2.1.3). For the latter, U_{LSDA} and U_{PBE} were used as an input to perform a single (one-shot) LDA+U and PBE+U calculation, on whose basis $U_{\mathrm{LDA+U}}$ and $U_{\mathrm{PBE+U}}$ were determined, employing the orbital-dependent version of the fully localized double counting correction. The diagonal elements $U_{ii;ii}$ for orbital d_i (short notation: U_{d_i}) obtained from a cRPA calculation are shown in Fig. 22, the corresponding orbital magnetization is presented in Tab. 1.

For the LSDA, the U_{d_i} parameters range from 6.1 eV to 7.8 eV, where U_{z^2} is the lowest and U_{xy} the highest. The spin is not localized, only the x^2-y^2 orbital is nearly full, all other orbitals carry significant magnetization, and no apparent connection between magnetization and size of U is visible. For the PBE functional, the U_{d_i} are significantly higher, ranging from 8.0 eV to 9.8 eV. The spin is localized in the z^2 and xy orbitals, while the remaining orbitals are nearly completely filled, which also agrees with results from previous calculations with high-level correlation[69;70], and is henceforth assumed to be the correct spin state. Note that in the literature, the spin is reported to be localized in the z^2 orbital and either in the xy or the x^2-y^2 orbital, depending on the spatial orientation of the system, and can be adjusted by a simple rotation of 45° around the z axis. The higher U_{d_i} values correspond to the half-filled orbitals. The U_{d_i} parameters for LDA+U deviate significantly from the LSDA result. They are much higher and less spread out, ranging from 8.3 eV to 8.7 eV. LDA+U captures the correct spin state, and the orbitals that carry the spin have higher U_{d_i} values, but the effect is less

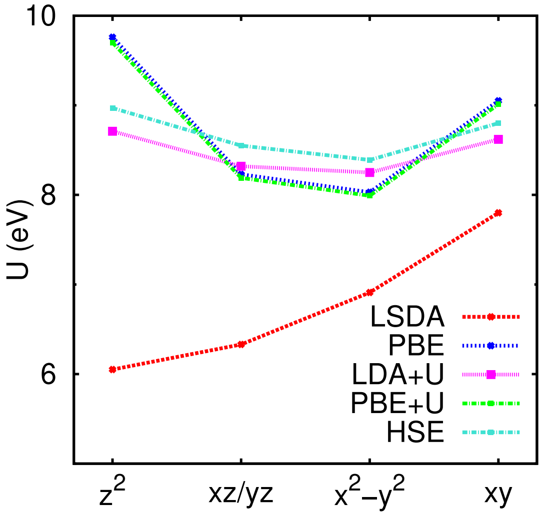

Figure 22: Elements of the partially screened Coulomb interaction $U_{ik;jl}$ for the d level of the Co atom for different DFT functionals. The lines between data points are a guide for the eye.

	z^2	xz/yz	x^2-y^2	xy
LSDA	0.39	0.31	0.09	0.65
PBE	0.85	0.06	0.03	0.88
HSE	0.97	0.03	0.02	0.97
LDA+U	0.98	0.03	0.01	0.98
PBE+U	0.99	0.01	0.01	0.99

Table 1: Magnetization $n_{d_{i\uparrow}} - n_{d_{i\downarrow}}$ for orbital d_i of the Co atom for various DFT functionals, where $n_{d_{i\sigma}}$ is is the orbital's occupation for spin channel σ.

pronounced than in the case of the PBE functional. The PBE+U result is almost completely identical to the PBE, and the U_{d_i} lie only slightly (0.05 eV) below their PBE values. The HSE is very similar to LDA+U, ranging from 8.4 eV to 9.0 eV, which is about 0.2 eV higher than the LDA+U values. It captures the correct spin state, and shows the same trends as the LDA+U result. The direct elements between sites $U_{ii;jj}$ follow similar trends as the direct on-site elements $U_{ii;ii}$, and are on average 1 eV below the on-site elements, irrespective of the employed functional. The exchange elements $U_{ij;ji}$, often denoted J_{ij}, are insensitive to the functional and vary between 0.55 eV and 1.05 eV for different combinations of i and j (also see Tab. 3).

Overall, only the LSDA does not obtain the correct spin state, while all higher-level functionals do. U_{d_i} parameters are also considerably higher for functionals with higher-level correlation. The geometry also seems to play an important role: Ref. [70] uses the identical methodology and the LSDA, but a differently optimized geometry, and obtains a slightly different spin state and considerably lower and less spread-out U_{d_i} between 5.23 eV and 5.56 eV. There is also a connection between occupancy and U_{d_i}, where higher magnetization leads to higher U_{d_i}. This effect is most pronounced for PBE and PBE+U.

4.3 Self-consistent DFT+U

As a next step, the effect of self-consistency (sc) on the electronic structure and the resulting partially screened Coulomb interaction U obtained by cRPA will be investigated for a DFT+U calculation. The starting point is a DFT calculation, based on which U will be computed within the cRPA. The resulting U is used as input for a DFT+U calculation, which will not only lead to a rearrangement of the d levels, which are affected directly by U, but will affect the complete electronic structure. Based on this updated electronic structure, a new U can be obtained, which can be used for a new DFT+U calculation. This can be repeated until convergence is reached, where occupation and U approach a constant. In this section, self-consistent LDA+U and PBE+U calculations will be performed. Self-consistent DFT+U combined with the cRPA has already been applied to various systems[220;222], and it has been stressed that it is superior to one-shot DFT+U in certain situations. This section does not intend to give a complete account of scDFT+U, but is used to get a first idea of the influence of self-consistency in U on the electronic structure. While DFT+U and scDFT+U can describe the formation of Hubbard bands, they cannot account for Kondo physics, which requires more advanced methods. The effect of self-consistency will be investigated in much more detail in chapter 5, where different types of self-consistent DFT+OCA calculation are performed.

Fig. 23 shows the direct on-site elements $U_{ii;ii}$ for a converged scLDA+U and scPBE+U, comparing them to those of one-shot LDA+U, one-shot PBE+U and the range-separated hybrid HSE from the previous section. The scLDA+U and scPBE+U results are nearly identical and only offset by less than 0.2 eV, while the relative size of different $U_{ii;ii}$ is the same. They lie about 0.8 eV and 1.0 eV above the HSE and one-shot LDA+U results, respectively, and have similar relative sizes: U_{z^2} is the highest, $U_{x^2\text{-}y^2}$ the lowest, and the elements lie relatively closely together. While scLDA+U behaves similarly to one-shot LDA+U, PBE+U (whose U is very close to the PBE result) yields relatively spread-out U values. This spread is significantly reduced due the self-consistency, where U_{z^2} remains almost the same, but the remaining U_{d_i} are

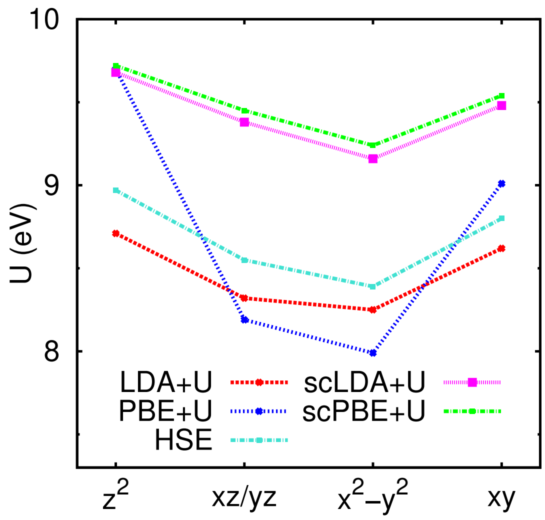

Figure 23: Elements of the partially screened Coulomb interaction $U_{ik;jl}$ for the d level of the Co atom for self-consistent DFT+U, compared to other functionals. The lines between data points are a guide for the eye.

	z^2	xz/yz	x^2-y^2	xy
LDA+U	0.98	0.03	0.01	0.98
scLDA+U	0.98	0.02	0.01	0.98
PBE+U	0.99	0.01	0.01	0.99
scPBE+U	0.99	0.01	0.01	0.99
HSE	0.97	0.03	0.02	0.97

Table 2: Magnetization $n_{d_{i\uparrow}} - n_{d_{i\downarrow}}$ for orbital d_i of the Co atom for self-consistent LDA+U and PBE+U, where $n_{d_{i\sigma}}$ is is the orbital's occupation for spin channel σ.

raised significantly.

The d level occupation and magnetization is almost completely unaffected by the self-consistency process (see Tab. 2), and all presented methods yield nearly identical occupations, where z^2 and xy carry the spin, while the remaining orbitals are completely filled.

The next goal is to better understand the self-consistency process itself. To this end, Fig. 24 shows the direct on-site elements $U_{ii;ii}$ and one selected direct element $U_{ii;jj}$ for several steps of the self-consistency process for scLDA+U and scPBE+U. The zeroth step corresponds to the pure LSDA/PBE calculation, the first step to the one-shot LDA+U/PBE+U.

For LDA+U, the first step leads to a significant increase and a relative change in size between different U_{d_i}. The addition of U changes the d level occupation significantly (see Tab. 1), which is distributed over several orbitals for the LSDA (a typical deficiency of the LSDA), and becomes localized due to the addition of U. For PBE+U, U remains almost constant in the first step, potentially since PBE already finds the correct orbital occupation. Surprisingly, a significant drop of U occurs in the second step, for both scLDA+U and scPBE+U and all $U_{ii;jj}$. In the third step, a significant jump of U is observed. In the following steps, U increases monotonically and quickly reaches a plateau. The differences between the 6th and 7th step are negligibly small, so self-consistency is reached after 6 steps for both scLDA+U and scPBE+U. The occupation of the d levels remains nearly constant in the self-consistency process, also for the second step of the self-consistency, where the significant drop of U is observed, and is therefore not shown.

We see that self-consistency has a considerable effect on U for a DFT+U calculation. Since the d level occupation barely changes, it must mostly stem from changes in the surrounding electronic structure, not necessarily from the d levels themselves. The self-consistent values

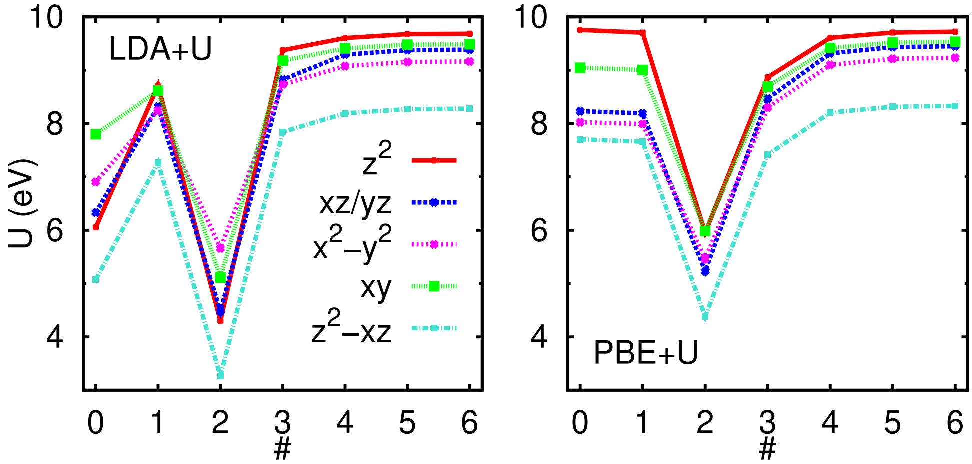

Figure 24: Elements of the partially screened Coulomb interaction U for the d level of the Co atom for different iterations of scLDA+U and scPBE+U. All direct on-site $U_{ii;ii}$ elements (red, green, blue, magenta) and one direct $U_{ii;jj}$ element between different sites (light blue) are presented.

of U are higher than those obtained from DFT functionals or one-shot DFT+U. A possible explanation is that the d levels are pushed away from the Fermi level due to adding U, forming Hubbard bands, and therefore reducing the screening at the Fermi level, leading to higher U parameters in each consecutive step of self-consistency until a plateau is reached. The formation of the Kondo peak, which cannot be described by DFT+U or scDFT+U, might remedy this issue by shuffling spectral weight back to the Fermi level and contributing to the screening. This will be explored in chapter 5.

4.4 U for different polarization regions

So far, the size of the polarization region has been kept fixed, containing the Co and the 9 surrounding Cu atoms. This section will explore the influence of the size of the polarization region on the resulting partially screened Coulomb interaction U. To this end, cRPA calculations will be performed for differently sized polarization regions P, which are shown in Fig. 25. Atoms are added to the polarization region P in accordance to their distance to the Co atom, where atoms of equal distance have to be added as a group. The smallest cluster consists of the Co atom and the 4 closest Cu atoms of the topmost layer of the Cu surface. The next cluster adds one more Cu atom of the second layer which is located directly underneath the Co atom. The cluster of 10 atoms adds another 4 atoms of the second layer. This cluster was used so far in this chapter. The next-biggest cluster contains 18 atoms. For a basis set size of 13 basis functions per atom ($3s3p4s4d4p$), inclusion of 8 additional atoms would make the resulting polarizabilities Π^0_P and interactions V and W too large to be handled computationally. A possible workaround is to remove the semi-core states of the Cu atoms for the computation of the polarizability, reducing the number of basis functions per atom to 9 ($4s4d4p$), which makes the polarizability and cRPA calculation feasible. While it has been pointed out that the inclusion of semi-core states is essential to correctly capture the electronic structure of certain transition metal compounds (see discussion in Sec. 3.2), they might play a smaller role for an excited-state-property like the polarizability. This effect will also be explored in this section.

Tab. 3 presents different elements $U_{ik;jl}$, namely all direct on-site elements $U_{ii;ii}$, two selected direct elements $U_{ii;jj}$ between orbitals i and j and two exchange elements $U_{ij;ji}$ for different sizes

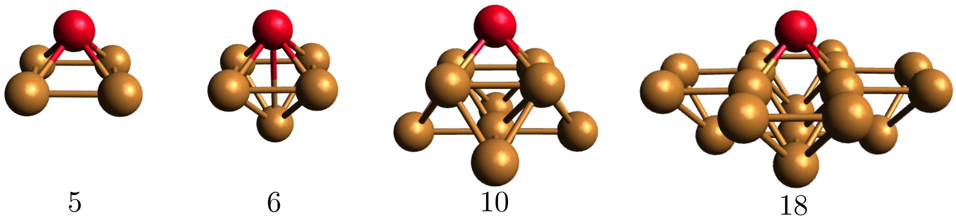

Figure 25: Different polarization regions for the Co@Cu(001) system. The number indicates the total number of atoms within the polarization region P.

of the polarization region and different functionals. The main result is visualized in Fig. 26, where the average over the direct on-site elements $\bar{U} = \sum_i U_{ii;ii}$ is plotted for the LSDA, the PBE and the HSE functionals, including and excluding semi-core states. It suffices to analyze $\bar{U}$, since the relative size of different $U_{ii;ii}$ does not change when the size of the polarization region is changed.

For the LSDA, $\bar{U}$ increases when the polarization region is made bigger, from 5.0 eV to 6.7 eV when increasing the size from 5 to 10 atoms. This seems counterintuitive, since more orbitals contributing to the screening process are added, which should lead to lower partially screened Coulomb interactions. When excluding semi-core states, $\bar{U}$ is about 0.3 eV higher than for the LSDA with semi-core states included, indicating that they contribute to the screening and should be included if high accuracy is required. For a polarization region containing 18 atoms

		$U_{ii;ii}$				$U_{ii;jj}$		$U_{ij;ji}$	
	size	U_{z^2}	$U_{xz/yz}$	$U_{x^2-y^2}$	U_{xy}	$U_{z^2;xz}$	$U_{z^2;xy}$	$J_{z^2\,xz}$	$J_{z^2\,xy}$
LSDA	5	4.88	4.90	5.08	5.45	3.78	3.38	0.55	0.85
	6	4.89	4.94	5.10	5.48	3.81	3.40	0.55	0.87
	10	6.05	6.33	6.91	7.80	5.07	5.00	0.56	0.91
PBE	5	8.42	7.64	7.36	8.18	6.77	6.21	0.59	1.02
	6	10.10	8.71	8.21	9.14	8.12	7.48	0.59	1.04
	10	9.76	8.23	8.03	9.05	7.71	7.24	0.60	1.05
HSE	5	10.10	9.76	9.49	9.93	8.67	7.97	0.63	1.01
	6	10.10	9.75	9.49	9.93	8.67	7.99	0.63	1.01
	10	8.97	8.55	8.39	8.80	7.51	6.86	0.63	1.01
LSDA (w/o core states)	5	5.11	5.14	5.29	5.69	4.01	3.61	0.55	0.85
	6	5.12	5.17	5.30	5.69	4.04	3.62	0.55	0.87
	10	6.43	6.71	7.28	8.21	5.44	5.39	0.56	0.91
	18	25.18	23.62	24.63	30.33	23.19	25.55	0.59	1.03
PBE (w/o core states)	5	8.39	7.59	7.34	8.17	6.74	6.18	0.60	1.02
	6	9.95	8.58	8.12	9.04	7.98	7.36	0.59	1.04
	10	9.52	8.03	7.87	8.87	7.49	7.04	0.60	1.04
	18	9.14	7.76	7.79	8.78	7.17	6.82	0.61	1.04
HSE (w/o core states)	5	10.08	9.74	9.48	9.92	8.65	7.97	0.63	1.01
	6	10.08	9.73	9.48	9.92	8.65	7.98	0.63	1.01
	10	8.93	8.51	8.36	8.77	7.47	6.83	0.63	1.01
	18	8.36	7.97	7.96	8.31	6.92	6.33	0.63	1.00

Table 3: U parameter for Co@Cu(001) and different sizes of the polarization region for LSDA, PBE and HSE, with semi-core states included and excluded. All direct on-site elements $U_{ii;ii}$, selected direct elements between sites $U_{ii;jj}$ and exchange elements $U_{ij;ji}$ are presented.

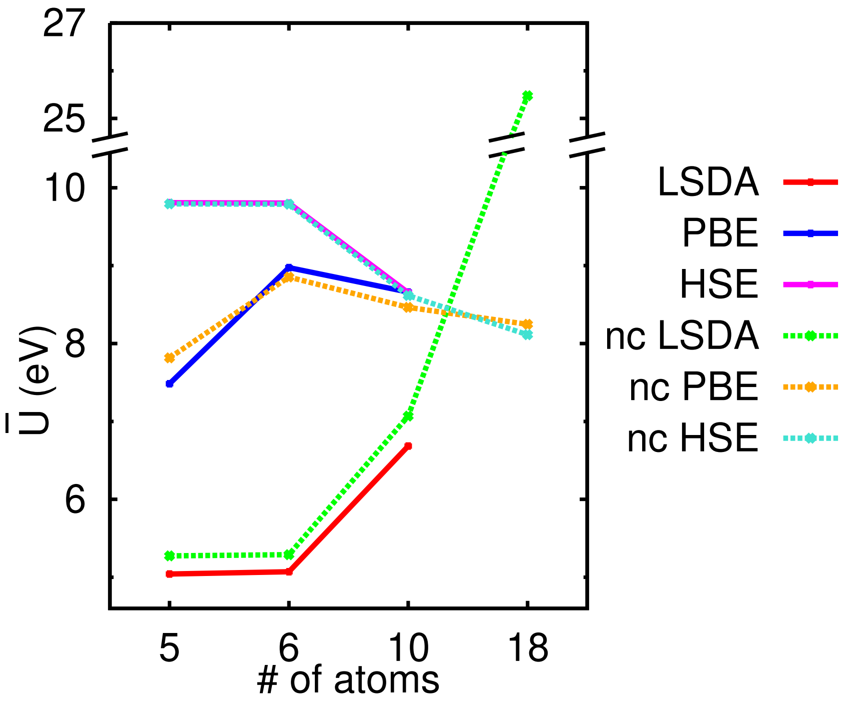

Figure 26: Average of the direct on-site parameters $\bar{U} = \sum_i U_{ii;ii}$ for differently sized polarization regions for the Co@Cu(001) system (also see Fig. 25).

and no semi-core states, however, an unphysical $\bar{U}$ of 25.5 eV is obtained. This is likely not a problem related to the semi-core states and might point to a more general problem of using the LSDA in the context of cRPA, and may also be related to the incorrect spin state which is found by the LSDA. This issue will also be discussed in more detail in Sec. 4.6.

In case of the PBE, $\bar{U}$ first increases when adding the 6th atom to the polarization region, and decreases when adding the next 4 atoms, not showing a clear trend. The exclusion of semi-core states also does not show a consistent behavior, and $\bar{U}$ is above the PBE result with semi-core states included for 5 atoms and below it for 6 and 10 atoms, the difference not being greater than 0.2 eV, though. For 18 atoms and no semi-core states included, $\bar{U}$ decreases and does not go up to unphysical values as in the case of the LSDA.

For the HSE functional and small polarization regions, $\bar{U}$ is close to 10 eV, considerably higher than for the other functionals. When the polarization region is enlarged, $\bar{U}$ behaves as one would intuitively expect: the more atoms contribute to the screening, the lower $\bar{U}$ becomes and for 18 atoms and no semi-core states, the resulting $\bar{U} = 8.1$ eV is lower than the corresponding PBE result, despite the much higher starting value. The semi-core states play a nearly negligible role.

Overall, $\bar{U}$ decreases when the size of the polarization region is increased, with the exception of the LSDA, where $\bar{U}$ grows to unphysically large values for the largest cluster. Convergence seems not to be reached for PBE and HSE, and the inclusion of more atoms to the polarization region would be desirable. Questions of convergence will be discussed in more detail in Sec. 4.5

and Sec. 4.6. Semi-core states seem to contribute to the screening, but not very strongly, and seem to be less relevant for functionals with higher-level correlation. The direct elements between orbitals $U_{ii;jj}$ behave similarly to the on-site elements upon changing the size of the polarization region, while the exchange elements $U_{ij;ji}$ are almost completely insensitive, so they are not discussed separately.

4.4.1 Co@Cu(111)

Although this chapter's focus is on the Co@Cu(001) system, this section will perform cRPA calculations for Co@Cu(111), in order to see if the trends observed for Co@Cu(001) are also present in this system. To this end, cRPA calculations are performed, employing the LSDA and PBE functionals, and using differently sized polarization regions, which are shown in Fig. 27. For Co@Cu(111), it is possible to include a total of 14 atoms in the largest cluster, and it is not necessary to exclude core electrons to make the calculation numerically feasible.

Tab. 4 shows the direct on-site elements of the partially screened Coulomb interaction U, and Fig. 28 the average $\bar{U}$ of those elements. The trends are similar to those of the Co@Cu(001) system. For the LSDA, U increases when the polarization region is enlarged, reaching unphysically high values for the largest cluster of 14 atoms. The LSDA therefore seems to be unreliable in combination with cRPA calculations for the present class of systems. While $\bar{U}$ seems to assume reasonable values for small polarization regions, this is likely by chance, since its value becomes unphysical for larger polarization regions. For the PBE functional, $\bar{U}$ goes down when the size of the polarization region is increased, starting with $\bar{U} = 8.3$ eV for the smallest cluster of 4 atoms and going down to $\bar{U} = 7.2$ eV for the biggest cluster of 14 atoms. Also here, convergence does not seem to be reached, and a further decrease of $\bar{U}$ is probable if the polarization region were further enlarged. Although the total value of $\bar{U}$ goes down, the difference between individual elements becomes larger. For a polarization region consisting of 4 atoms, $U_{z^2} - U_{xy} = 0.29$ eV, while for 14 atoms, a much larger difference of $U_{z^2} - U_{xy} = 0.83$ eV is obtained.

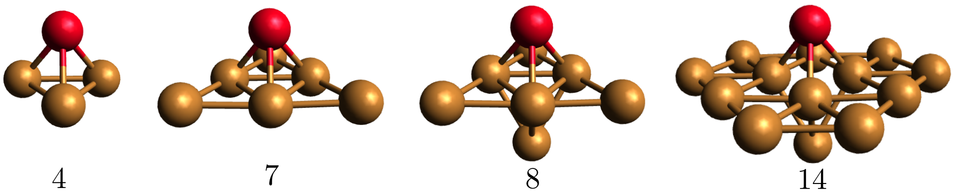

Figure 27: Different polarization regions for the Co@Cu(111) system. The number indicates the total number of atoms within the polarization region P.

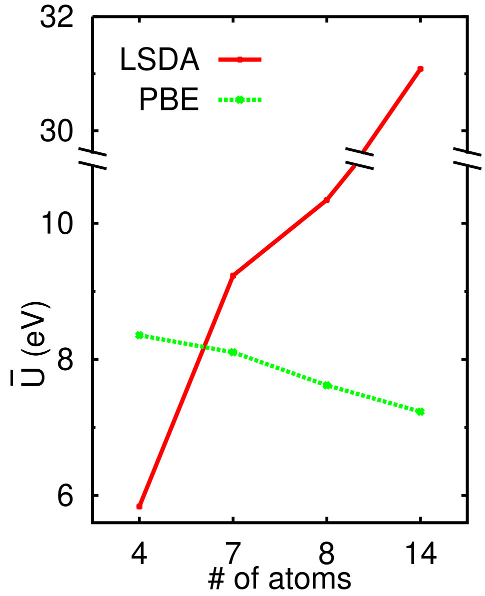

Figure 28: Average of the direct on-site parameters $\bar{U} = \sum_i U_{ii;ii}$ for differently sized polarization regions for the Co@Cu(111) system (also see Fig. 27).

	size	U_{z^2}	U_{xz}, U_{yz}	$U_{x^2-y^2}$, U_{xy}
LSDA	4	5.84	5.83	5.84
	7	8.34	8.95	9.96
	8	9.43	9.81	11.33
	14	27.91	28.66	35.09
PBE	4	8.13	8.40	8.42
	7	7.64	8.13	8.31
	8	7.17	7.66	7.81
	14	6.64	7.29	7.47

Table 4: U parameter for Co@Cu(001) and different sizes of the polarization region for LSDA and PBE.

4.5 Approximately including screening effects from outside of the polarization region

As we could see in the previous section, the partially screened interaction U obtained from a cRPA calculation does not seem to be fully converged with respect to the size of the polarization region. It would therefore be desirable to work with larger polarization regions P, which ideally would comprise the complete device D. This is a complicated task, however: the polarizability Π^0 and the Coulomb matrices V, W and U are 4-index quantities, and doubling the size of the polarization region would lead to a 16-fold increase in size for these quantities, quickly reaching computational limits of RAM and file size. The basis set used in this chapter consists of 13 basis functions per atom, and for a polarization region comprising 18 atoms and 8 Byte per file entry, the resulting file size is already $\approx$ 24 GB. This is already too much for the available hardware if more than two quantities have to be stored simultaneously, and could only be handled if matrices are only read in partially or results are directly written into files to reduce the RAM demand, which would also slow down calculations considerably. Even then, it would still be impossible to include the complete device region.

Unfortunately, it is also not possible to diagonalize the entirety of the system and work in a diagonal basis, which is further complicated by the use of non-orthogonal basis sets: at some point in the cRPA calculation, a non-sparse quantity would occur, which cannot be handled with the present methodology.

The goal of this section is therefore to find approximate solutions to the aforementioned problem, by approximately including polarization effects from outside of the polarization region. The necessary modules were not implemented in the ANT.G code, but in a new code, named NanoRPA, which exclusively takes care of screening and the cRPA. There is merit to that: since the memory demand can be very high as discussed earlier, a code just for the cRPA step does not need to store additional quantities from the DFT/ANT.G self-consistency cycle, freeing up memory and potentially enabling the use of better approximations or larger polarization regions. It was made sure that the NanoRPA-code exactly reproduces the cRPA results from the previous sections, and modules were added to approximately account for polarization effects from outside of the polarization region. Two approximations will be proposed in the following, namely pre-screening by the RPA to first order, and pre-screening of direct elements only.

4.5.1 Attempt 1 - Pre-screening by RPA to first order

The first attempt includes all polarization bubble diagrams of the device region, but approximates the Dyson equation Eq. 99, with the aspiration that it is sufficient to treat polarization effects from further away to first order. Just as the cRPA, this will be done as a two-step process: firstly, the complete device region will be screened by a polarization obtained from the RPA to first order, and secondly, the polarization region will be unscreened by a polarization obtained from the RPA to first order, resulting in a pre-screened U^{pre}. This will then be used as input for a conventional cRPA calculation within the polarization region, where U^{pre} replaces V in Eq. 99.

Method: As a first step, the polarization of the complete device region has to be computed in a diagonal basis. The starting point is the Hamiltonian of the complete device region $\mathbf{H}_{\mathrm{D}}$ in the local Gaussian basis, which can be diagonalized by a unitary matrix $\mathbf{u}$:

$$\mathbf{H}_{\tilde{\mathrm{D}}} = \mathbf{u}\,\mathbf{H}_{\mathrm{D}}\,\mathbf{u}^{-1}. \tag{104}$$

The diagonal basis is denoted by the tilde $\tilde{\mathrm{D}}$. From the diagonalized Hamiltonian, the GF of the complete device $\mathbf{G}_{\tilde{\mathrm{D}}}$ in the diagonal basis can be computed:

$$\mathbf{G}_{\tilde{\mathrm{D}}} = (\omega - \mathbf{H}_{\tilde{\mathrm{D}}} - \mathbf{\Sigma}_{\tilde{\mathrm{L}}} - \mathbf{\Sigma}_{\tilde{\mathrm{R}}})^{-1}. \tag{105}$$

Note that the self-energies $\mathbf{\Sigma}_{\tilde{\mathrm{L}}/\tilde{\mathrm{R}}}$ are not diagonal in the new basis after applying the unitary transformation $\mathbf{u}$. Since we do require the GF $\mathbf{G}_{\tilde{\mathrm{D}}}$ to be diagonal for the following considerations to work, their diagonality has to be enforced, by projecting out all non-diagonal elements after the unitary transformation to the diagonal subspace:

$$\mathbf{\Sigma}_{\tilde{\mathrm{L}}/\tilde{\mathrm{R}}} := \hat{P}^{\mathrm{diag}}\,\mathbf{u}\,\mathbf{\Sigma}_{\mathrm{L/R}}\,\mathbf{u}^{-1}\,\hat{P}^{\mathrm{diag}}. \tag{106}$$

This is an approximation, but since the self-energies are only directly affecting atoms at the edge of the cluster, their effect on the screening of the central Co atom is expected to be small.

From the diagonal GF $\mathbf{G}_{\tilde{\mathrm{D}}}$ it is possible to compute the polarizability of the complete device region by the RPA:

$$(\mathbf{\Pi}^{0}_{\tilde{\mathrm{D}}\tilde{\mathrm{D}}})_{\mu_1\mu_2;\mu_2\mu_1} = \frac{1}{2\pi}\int_{-\infty}^{\infty} \mathrm{d}\omega \sum_{\sigma} (\mathbf{G}_{\tilde{\mathrm{D}}})^{\sigma}_{\mu_1\mu_1}(\mathrm{i}\omega)(\mathbf{G}_{\tilde{\mathrm{D}}})^{\sigma}_{\mu_2\mu_2}(\mathrm{i}\omega). \tag{107}$$

Due to the diagonality of $\mathbf{G}_{\tilde{\mathrm{D}}}$, the polarizability $\mathbf{\Pi}^{0}_{\tilde{\mathrm{D}}\tilde{\mathrm{D}}}$ is now effectively a two-index quantity with size N_{D}^{2}, which can easily be stored (for the Co@Cu(001) system, $N_{\mathrm{D}} = 1268$), and the only approximation made so far was enforcing the self-energies $\mathbf{\Sigma}_{\tilde{\mathrm{L}}/\tilde{\mathrm{R}}}$ to be diagonal in the new basis. In this section, polarization and interactions will be assigned two labels, to account for different dimensions or basis sets of left and right superindex.

The second step is to use the polarizability of the device region to pre-screen the bare Coulomb interaction, by applying the RPA. The starting point for finding an appropriate approximation for the pre-screening is the RPA equation for the complete device region, where the bare interaction $\mathbf{V}$ is calculated in the local Gaussian basis and the polarization of the complete device region in the diagonal basis $\tilde{\mathrm{D}}$. Note that we do not need to compute the pre-screened interaction $\mathbf{W}^{\mathrm{pre}}$ for the complete device region. It suffices to compute $\mathbf{W}^{\mathrm{pre}}_{\mathrm{PP}}$ and $\mathbf{U}^{\mathrm{pre}}_{\mathrm{PP}}$ for the polarization region, where the latter serves as the starting point for a full cRPA calculation within the polarization region. The RPA equation for the complete device projected on the polarization region then becomes:

$$\mathbf{W}^{\mathrm{pre}}_{\mathrm{PP}} = \hat{P}_{\mathrm{P}}(1 - \mathbf{V}_{\mathrm{DD}}\mathbf{\Pi}^{0}_{\tilde{\mathrm{D}}\tilde{\mathrm{D}}})^{-1}\mathbf{V}_{\mathrm{DD}}\hat{P}_{\mathrm{P}}. \tag{108}$$

The bare Coulomb interaction of the device region $\mathbf{V}_{\mathrm{DD}}$ has dimension N_{D}^{4} and is too big to be computationally handled. In order to develop an approximation, the above equation can be expanded and the projection operator applied:

$$\mathbf{W}^{\mathrm{pre}}_{\mathrm{PP}} = \mathbf{V}_{\mathrm{PP}} + \mathbf{V}_{\mathrm{PD}}u_{\mathrm{D}\tilde{\mathrm{D}}}\mathbf{\Pi}^{0}_{\tilde{\mathrm{D}}\tilde{\mathrm{D}}}u_{\tilde{\mathrm{D}}\mathrm{D}}\mathbf{V}_{\mathrm{DP}} + \mathbf{V}_{\mathrm{PD}}u_{\mathrm{D}\tilde{\mathrm{D}}}\mathbf{\Pi}^{0}_{\tilde{\mathrm{D}}\tilde{\mathrm{D}}}u_{\tilde{\mathrm{D}}\mathrm{D}}\mathbf{V}_{\mathrm{DD}}u_{\mathrm{D}\tilde{\mathrm{D}}}\mathbf{\Pi}^{0}_{\tilde{\mathrm{D}}\tilde{\mathrm{D}}}u_{\tilde{\mathrm{D}}\mathrm{D}}\mathbf{V}_{\mathrm{DP}} + \ldots \tag{109}$$

The operators $u_{\mathrm{D}\tilde{\mathrm{D}}}$ and $u_{\tilde{\mathrm{D}}\mathrm{D}}$ were introduced to make it possible to carry out multiplications between quantities which are computed in different bases, where $u_{\mathrm{D}\tilde{\mathrm{D}}}$ is a generalized unitary matrix to transform one side of a 4-index quantity from D to $\tilde{\mathrm{D}}$, effectively transforming two indices (also see Sec. 4.1 and Eq. 99), therefore requiring a generalized version of the unitary matrix appearing in Eq. 104.

The second and all higher-order terms contain V_{DD} (or, after applying the unitary transformation, $V_{\tilde{\mathrm{D}}\tilde{\mathrm{D}}}$), so these terms can not be included in the approximation. This leaves the zeroth and first order terms, which will be used for the pre-screening process:

$$\mathbf{W}^{\mathrm{pre}}_{\mathrm{PP}} = \mathbf{V}_{\mathrm{PP}} + \mathbf{V}_{\mathrm{PD}}u^{*}_{\mathrm{D}\tilde{\mathrm{D}}}\mathbf{\Pi}^{0}_{\tilde{\mathrm{D}}\tilde{\mathrm{D}}}u^{*}_{\tilde{\mathrm{D}}\mathrm{D}}\mathbf{V}_{\mathrm{DP}}. \tag{110}$$

In practical calculations, the correct order of the multiplications is important, and has to either start from the left-hand or the right-hand side, such that no quantity of dimension N_{D}^{4} occurs. In this case, the largest quantity has dimension $N_{\mathrm{D}}^{2}N_{\mathrm{P}}^{2}$ and is the limiting factor in the aforementioned procedure. With $N_D = 1268$ for the Co@Cu(001) system, it is possible to treat a polarization region of 5 atoms (Co and 4 Cu) with $N_\mathrm{P} = 65$. In this case, the maximum file size is ≈ 46 GB, which is close to the RAM limit of the available hardware. Due to that it is not possible to have two quantities of this dimension stored in the RAM at one time and requires matrix multiplication results to be directly written to files. Note that while the operators $u^*_{\mathrm{D}\tilde{\mathrm{D}}}$ and $u^*_{\tilde{\mathrm{D}}\mathrm{D}}$ have labels D and $\tilde{\mathrm{D}}$, they apply separate unitary transformations for each index, and each transformation matrix has size N_D^2 only.

The pre-screened interaction $\mathbf{W}^\mathrm{pre}_\mathrm{PP}$ then has to be unscreened by RPA to first order within the polarization region to obtain $\mathbf{U}^\mathrm{pre}_\mathrm{PP}$:

$$\mathbf{U}^\mathrm{pre}_\mathrm{PP} = \mathbf{W}^\mathrm{pre}_\mathrm{PP} - \mathbf{W}^\mathrm{pre}_\mathrm{PP}\mathbf{\Pi}^0_\mathrm{PP}\mathbf{W}^\mathrm{pre}_\mathrm{PP}. \tag{111}$$

This way, polarization effects from outside of the polarization region are included to first order. The pre-screened interaction $\mathbf{U}^\mathrm{pre}_\mathrm{PP}$ then serves as a starting point for a full cRPA calculation, replacing $\mathbf{V}$ in Eq. 99 and 100.

Results and discussion: The described methodology is now applied to the Co@Cu(001) system. The ANT.G code is used to compute the bare Coulomb interactions $\mathbf{V}_\mathrm{PP}$ and $\mathbf{V}_\mathrm{DP/PD}$, the unitary matrix u and the polarizability $\mathbf{\Pi}^0_{\tilde{\mathrm{D}}\tilde{\mathrm{D}}}$, which serve as input for the NanoRPA code. The PBE functional is used throughout this section, and the polarization region contains the Co atom and the 4 neighboring Cu atoms (see Fig. 25). Tab. 5 contains direct on-site elements and selected direct and exchange elements for bare, pre-screened and fully screened interactions.

The direct elements of the pre-screened $\mathbf{W}^\mathrm{pre}$ assume negative values, which appears to be an unphysical result. It might, however, also be due to the fact that first-order RPA is not sufficient for the polarization region itself, but accurate for the remaining device, and could be remedied by the unscreening to first order within the polarization region.

Unfortunately, this is also not the case. The direct elements of the pre-screened U^pre are positive, but more than one order of magnitude larger than the bare interaction, which would signify an extremely strong negative screening due to the device outside of the polarization region, which seems highly unlikely and unphysical.

$\mathbf{U}^\mathrm{pre}$ now acts as the starting point for a cRPA calculation within the polarization region P. Surprisingly, although the direct elements of $\mathbf{U}^\mathrm{pre}$ are considerably too high, they lead to physical values for $\mathbf{W}$ and $\mathbf{U}$, where the direct on-site elements $U_{ii;ii}$ range from 6.64 eV for the x^2-y^2 orbital to 8.87 eV for the xz/xy orbital. This is in contrast to the cRPA results without any pre-screening (see Fig. 22), where the orbitals carrying the spin had higher on-site U parameters, while those of filled orbitals were lower. The average $\bar{U} = 8.05$ eV is still higher than that of a 'pure' cRPA calculation, using PBE and the same polarization region of 5 atoms, which results in $\bar{U} = 7.82$ eV.

Although the final result for $\mathbf{U}$ seems to have some merit, the results cannot be trusted, since they are based on unphysical intermediate results after the pre-screening, and the final result

		$X_{ii;ii}$				$X_{ii;jj}$		$X_{ij;ij}$	
	X	X_{z^2}	$X_{xz/yz}$	$X_{x^2-y^2}$	X_{xy}	$X_{z^2;xz}$	$X_{z^2;xy}$	$X_{z^2\,xz}$	$X_{z^2\,xy}$
PBE	V	24.3	24.3	24.3	24.3	22.2	23.0	0.64	1.05
	W^{pre}	-937	-936	-922	-928	-937	-933	0.26	0.11
	U^{pre}	832	834	744	747	831	786	1.18	2.81
	W	0.96	0.78	1.44	1.29	0.16	0.15	0.39	0.35
	U	8.25	8.87	6.64	7.63	6.77	6.25	0.94	1.85

Table 5: Selected elements of the interaction V, the pre-screened interactions W^{pre} and U^{pre} using RPA to first order, the fully screened interaction W and the final partially screened interaction U.

could just be due to some type of error cancellation. Even if it was not, no decrease, but a slight increase of the average direct on-site **U** was observed. The use of first-order RPA for the screening due to the remaining device region is therefore not sufficient, and the infinite resummation of the RPA might be essential for it to function also for screening effects from further away. Screening in metallic systems is simply too strong and too long-range to justify the use of a first-order approximation.

Although the LSDA was shown to be unreliable, the same calculation has been run for the LSDA as well, and similar results have been found, which are not shown.

4.5.2 Attempt 2 - Pre-screening of direct elements only

For the second attempt, the pre-screening is only done for the direct elements of the Coulomb interaction, which are most strongly affected in the screening process due to the long range of the Coulomb interaction, using only the corresponding elements of the polarizability. The basic assumption is that all other elements of the Coulomb interaction are only weakly affected from polarization effects from outside of the polarization region: as we already saw in this chapter, exchange elements are not strongly affected by the screening, and other elements of the Coulomb interaction are typically small and will also be neglected in the DFT+OCA calculations in the following chapter 5. The pre-screening will be done as a two-step process analogously to the cRPA: firstly, the direct elements of the Coulomb interaction are screened for the complete device region. Secondly, the direct elements will be unscreened within the polarization region, resulting in a pre-screened U^{pre}. This will then be used as input for a conventional cRPA calculation within the polarization region, where U^{pre} replaces the direct elements of V in Eq. 99.

Method: The starting point for the pre-screening are the direct elements of the bare Coulomb interaction

$$V^{\text{dir}}_{\alpha_1\beta_1;\alpha_2\beta_2} = V_{\alpha_1\alpha_1;\alpha_2\alpha_2}\delta_{\alpha_1\beta_1}\delta_{\alpha_2\beta_2}, \tag{112}$$

where δ is the Kronecker delta. The polarizability diagrams that connect different direct elements of the Coulomb interactions are of the following type,

$$(\Pi^0_\mathrm{D})_{\mu_1\mu_1;\mu_2\mu_2} = \frac{1}{2\pi}\int_{-\infty}^{\infty} \mathrm{d}\omega \sum_\sigma (G_\mathrm{D})^\sigma_{\mu_2\mu_1}(\mathrm{i}\omega)(G_\mathrm{D})^\sigma_{\mu_1\mu_2}(\mathrm{i}\omega), \tag{113}$$

and all other elements of the polarizability will be neglected for the pre-screening. Both $V_{\alpha_1\alpha_1;\alpha_2\alpha_2}$ and $(\Pi^0_\mathrm{D})_{\mu_1\mu_1;\mu_2\mu_2}$ have size N_D^2, and can be easily treated computationally. Firstly, the direct elements of the Coulomb interaction will be screened for the complete device by the RPA, in order to obtain W^pre:

$$W^\mathrm{pre}_{\alpha_1\alpha_1;\alpha_2\alpha_2} = \sum_{\mu_1,\mu_2}\left[\left(1 - V_{\alpha_1\alpha_1;\mu_1\mu_1}(\Pi^{0,\mathrm{dir}}_\mathrm{D})_{\mu_1\mu_1;\mu_2\mu_2}\right)^{-1}\right]_{\alpha_1\alpha_1;\mu_2\mu_2} V_{\mu_2\mu_2;\alpha_2\alpha_2}. \tag{114}$$

The direct elements W^pre are then partially unscreened by $\Pi^{0,\mathrm{dir}}_\mathrm{P}$ within the polarization region, resulting in U^pre:

$$U^\mathrm{pre}_{\alpha_1\alpha_1;\alpha_2\alpha_2} = \sum_{\mu_1,\mu_2}\left[\left(1 + W^\mathrm{pre}_{\alpha_1\alpha_1;\mu_1\mu_1}(\Pi^{0,\mathrm{dir}}_\mathrm{P})_{\mu_1\mu_1;\mu_2\mu_2}\right)^{-1}\right]_{\alpha_1\alpha_1;\mu_2\mu_2} W^\mathrm{pre}_{\mu_2\mu_2;\alpha_2\alpha_2}. \tag{115}$$

Note that $\Pi^{0,\mathrm{dir}}_\mathrm{P}$ is not just a submatrix of $\Pi^{0,\mathrm{dir}}_\mathrm{D}$ due to the use of non-orthogonal basis sets, and the use of the correct projection is crucial to obtain correct results[70] (also see appendix B). We then proceed to apply the cRPA methodology described in Sec. 4.1, where the direct elements of V_P are replaced by those of $U^\mathrm{pre}_\mathrm{P}$

$$V^\mathrm{pre}_{\alpha_1\beta_1;\alpha_2\beta_2} \rightarrow \begin{cases} U^\mathrm{pre}_{\alpha_1\beta_1;\alpha_2\beta_2} & \forall\ \alpha_1 = \beta_1 \wedge \alpha_2 = \beta_2 \\ V_{\alpha_1\beta_1;\alpha_2\beta_2} & \text{otherwise,} \end{cases} \tag{116}$$

V^pre replaces V in Eq. 99, and a conventional cRPA calculation is performed to obtain U.

Results and discussion: The described methodology is applied to the Co@Cu(001) system. The ANT.G code is used to compute the direct elements of the bare Coulomb interaction $V_{\alpha_1\alpha_1;\alpha_2\alpha_2}$ and the corresponding elements of the polarizability $(\Pi^{0,\mathrm{dir}}_\mathrm{D})_{\mu_1\mu_1;\mu_2\mu_2}$, which serve as input for the NanoRPA code. The PBE functional is used throughout this section, and the polarization region contains the Co atom and the 9 neighboring Cu atoms (see Fig. 25).

Tab. 6 shows all direct on-site elements and selected other direct and exchange elements of the bare, pre-screened and completely screened interactions. The elements of W^pre have positive values between 2.2 and 2.7 eV for the on-site and 0.8 and 1.2 eV for other direct elements, which seems to be a reasonable result in line with screened interaction from RPA calculations in the previous sections. Note that exchange elements are not included in the pre-screening and omitted in Tab. 6.

The unscreening of the direct elements within the polarization region yields interactions ranging from 8.1 to 9.2 eV for the direct on-site elements and 6.6 to 7.0 eV for other direct elements of U^pre. This is a surprising result, since screening from within the polarization region has been

		$X_{ii;ii}$				$X_{ii;jj}$		$X_{ij;ij}$	
	X	X_{z^2}	$X_{xz/yz}$	$X_{x^2-y^2}$	X_{xy}	$X_{z^2;xz}$	$X_{z^2;xy}$	$X_{z^2\,xz}$	$X_{z^2\,xy}$
PBE	V	24.3	24.3	24.3	24.3	22.2	23.0	0.64	1.05
	W^{pre}	2.17	2.26	2.66	2.52	1.17	0.76	-	-
	U^{pre}	8.39	8.08	9.16	8.98	6.98	6.57	-	-
	W	2.31	2.38	2.87	2.64	1.34	0.91	0.34	0.75
	U	8.93	7.65	7.77	8.57	6.95	6.54	0.59	1.02

Table 6: Bare interaction V, pre-screened interactions W^{pre} and U^{pre} obtained from applying the RPA for direct elements of the Coulomb interaction only, fully screened interaction W and final partially screened interaction U.

subtracted, and U^{pre} contains screening contributions from outside of the polarization region only. This screening is already very strong and similar in size to the screening due to the polarization region itself (see cRPA results for PBE in Sec. 4.2).

As described above, U^{pre} now replaces the direct elements of V as starting point for a cRPA calculation within the polarization region. The direct elements of the fully screened interaction W are 0.1 to 0.2 eV higher than W^{pre}. This difference can be attributed to the fact that the computation of W includes all types of polarizability diagrams and also non-direct elements of the Coulomb interaction.

In the last calculation step, the partially screened U is computed. Direct on-site elements range from 7.7 to 8.9 eV, which is lower than the corresponding cRPA result without pre-screening for the PBE functional (8.0 to 9.8 eV). The half-filled orbitals z^2 and xy have higher values of U than the filled ones, also in line with previous results presented in this chapter.

The pre-screening of the direct elements leads to the anticipated result: the final partially screened U is lower than the corresponding result without pre-screening, successfully incorporating polarization effects from outside of the polarization region. The values of U^{pre} are unexpectedly low, and the same order of magnitude as the final U. Particularly for the z^2 orbital, U^{pre} is smaller than U, which means that the local screening due to the full polarizability within the polarization region leads to an increase in U, which cannot be easily explained. Further testing would be required to show that the method is applicable to other systems and functionals, and make sure that the present results are not based on some type of error cancellation. If these tests were successful, the proposed methodology could serve as a simple and computationally cheap possibility to include polarization effects from outside of the polarization region.

4.6 Discussion

This chapter introduced the cRPA methodology to obtain partially screened interactions U, and applied the cRPA for the Co@Cu(001) system and various functionals.

We could also see that the LSDA seems to yield unreliable results for the partially screened interaction U, which was particularly evident when the size of the polarization region was increased. This problem only occurred for the 'pure' LSDA, and was not present in one-shot or self-consistent LDA+U. It can potentially be attributed to the fact that LSDA gives an incorrect orbital occupation, where the spin is distributed over all d orbitals, which is a well-known deficiency of the LSDA. It might also not sufficiently capture polarization effects appropriately, which are non-local in nature.

For all higher-level functionals, namely PBE, HSE, one-shot and self-consistent DFT+U, the results are more consistent: direct on-site elements lie in the range of 8.0 to 9.8 eV, where the lowest average value is observed for one-shot LDA+U and the highest average value for self-consistent LDA+U and PBE+U. The highest direct on-site elements of U can be attributed to the orbitals carrying the spin. This effect is strong for PBE and less strong, albeit present, for all other functionals studied.

In principle, there are two convergences to be taken into account: firstly, convergence with respect to the size of the polarization region. The Coulomb interaction is intrinsically long-range, and the cRPA method is limited to relatively small sizes of the polarization region. The convergence with respect to the size of the polarization region has been tested for several clusters for the Co@Cu(001) and the Co@Cu(111) system in Sec. 4.4. It was shown that the size of the partially screened interaction U goes down when the size of the polarization region is increased, with the notable exception of the LSDA, where an unphysical increase was observed, which is not present for one-shot or self-consistent LDA+U. Convergence with respect to the size of the polarization region does not seem to be reached yet for the largest clusters that could computationally be tested. Unfortunately, the calculations with the present implementation are limited to relatively small clusters due to the rapidly growing size of interaction and polarizability matrices when the size of the polarization region is increased.

Two methods were proposed to include polarization effects from outside of the polarization region approximately: using the RPA to first order for the pre-screening yields unphysical intermediate results for the pre-screened interactions. Although the final U is close in size to the cRPA values without pre-screening, it does not lead to an overall reduction of the average of the direct on-site elements of U, and does not reproduce the relative size of the different direct on-site elements, and this attempt will not be further pursued. The pre-screening of only the direct elements yields more promising results: the interactions W^{pre} and U^{pre} have physical values, although it is surprising that the pre-screening alone already leads to a considerable screening of the Coulomb interaction. The final U is lower than the pure cRPA result without pre-screening, and the relative size of the direct on-site elements is maintained when the pre-screening is included. The pre-screening of the direct elements might serve as a cheap and easily implemented way to include screening effects from outside of the polarization region in the future, but further testing for different systems and functionals will still be required.

The second convergence is with respect to the number of unoccupied and occupied orbitals taken into account in the computation of the polarizability. This can be more easily seen in the notation of Ref. [217]:

$$\Pi(\vec{r},\vec{r}\,';\omega) = \sum_{i}^{\text{occ}} \sum_{j}^{\text{unocc}} \Psi_i(\vec{r})\Psi_i^*(\vec{r}\,')\Psi_j^*(\vec{r})\Psi_j(\vec{r}\,') \left(\frac{1}{\omega - \epsilon_j + \epsilon_i + \mathrm{i}0^+} - \frac{1}{\omega + \epsilon_j - \epsilon_i + \mathrm{i}0^+} \right), \tag{117}$$

where Ψ_i and ϵ_i are one-particle Block eigenfunctions and eigenvalues of the system. The denominator in the calculation of the polarizability contains differences between occupied and unoccupied orbitals, and only a certain number of unoccupied orbitals, typically up to an energy cutoff, can be included in realistic calculations. Since the denominator only decays slowly with increasing energy of unoccupied orbitals, this convergence can be slow, requiring the inclusion of a high number of unoccupied orbitals. While the energy cutoff is an input parameter in plane-wave basis sets, it is less obvious in calculations with a local basis, where the convergence has to be tested by adding additional basis functions describing unoccupied orbitals. This is problematic, however, since it would lead to a considerable increase of the size of Coulomb interactions and polarizability, and it could only be tested for very small polarization regions of 5 atoms, which has been shown to be too small. The energy convergence has therefore not been tested in the present work.

So far, no statement was made on the expected size of the interaction U. This will be done in the next chapter, where U serves as an input parameter for an Anderson impurity model, which will be solved within the OCA. The resulting self energy will be used to calculate the correlated transmission, which can then be compared to experimental data. The next chapter will also discuss the influence of the Kondo peak on U in a self-consistent DFT+OCA calculation, and perform self-consistent DFT+OCA+cRPA calculations, where U is updated each cycle.

5 Transport calculations for the full d shell using DFT+OCA

This chapter will go further towards a full ab-initio description of the Co@Cu(001) system. The complete d shell of the Co adatom will be correlated, and U will not be treated as a tunable parameter: it will instead be determined by the cRPA introduced in chapter 4. The final result will be the correlated transmission $\mathcal{T}(\omega)$, which can then be compared to experimental conductance curves.

We will proceed in three steps. At first, a one-shot DFT+OCA calculation will be performed, computing the correlated transmission from the non-interacting GF and the correlated self energy, similar to chapter 3, but correlating the complete d shell. In the second step, the charge-density will be updated at each cycle to incorporate the effects of the correlated self energy within the d shell: the correlated self-energy will be included in the DFT calculation, which will, in turn, lead to updated d level positions and an updated hybridization function. This defines a new AIM, which is solved by the OCA. This is repeated until self-consistency is reached. The U parameter is kept unchanged throughout the calculation. This will be called the charge self-consistency cycle. The third step will include the computation of U in the self-consistency cycle. Based on the updated charge density, a new hybridization function is determined and an updated U is computed by the cRPA. This defines a new AIM, which is solved by the OCA. This is also repeated until self-consistency is reached, and will be called the charge-U self-consistency cycle.

5.1 One-shot DFT+OCA

As the first step, one-shot DFT+OCA calculations are performed. DFT has already been combined with different impurity solvers in the past, often in the context of one-shot DFT+DMFT[231;232;233]. It improves many system properties, for instance for transition metals[232], transition metal oxides[234] and f electron systems[235;236]. The advantages are clear: the method is relatively cheap, and once a self-energy describing the correlations within the d shell is obtained, the interacting GF of the device can be directly computed according to Eq. 86 and the correlated transmission according to Eq. 87. One-shot DFT+OCA will serve as a good starting point for more advanced calculations.

The methodology used in this chapter has been tested and extended in the past[70;150;166;171;237;238]. We proceed in the same spirit as chapter 3, but instead of correlating a single d level, the complete d shell is treated by the OCA. The computational scheme is shown in Fig. 29.

5.1.1 Results

At first, the ANT.G code is used to perform a DFT calculation of the Co@Cu(001) system connected to semi-infinite surface and STM tip, which are described by Bethe lattice self energies. The LANL2MB minimal basis set[187;189] is employed, which explicitly includes the valence electrons and the outer core electrons, while the inner core electrons are described by a

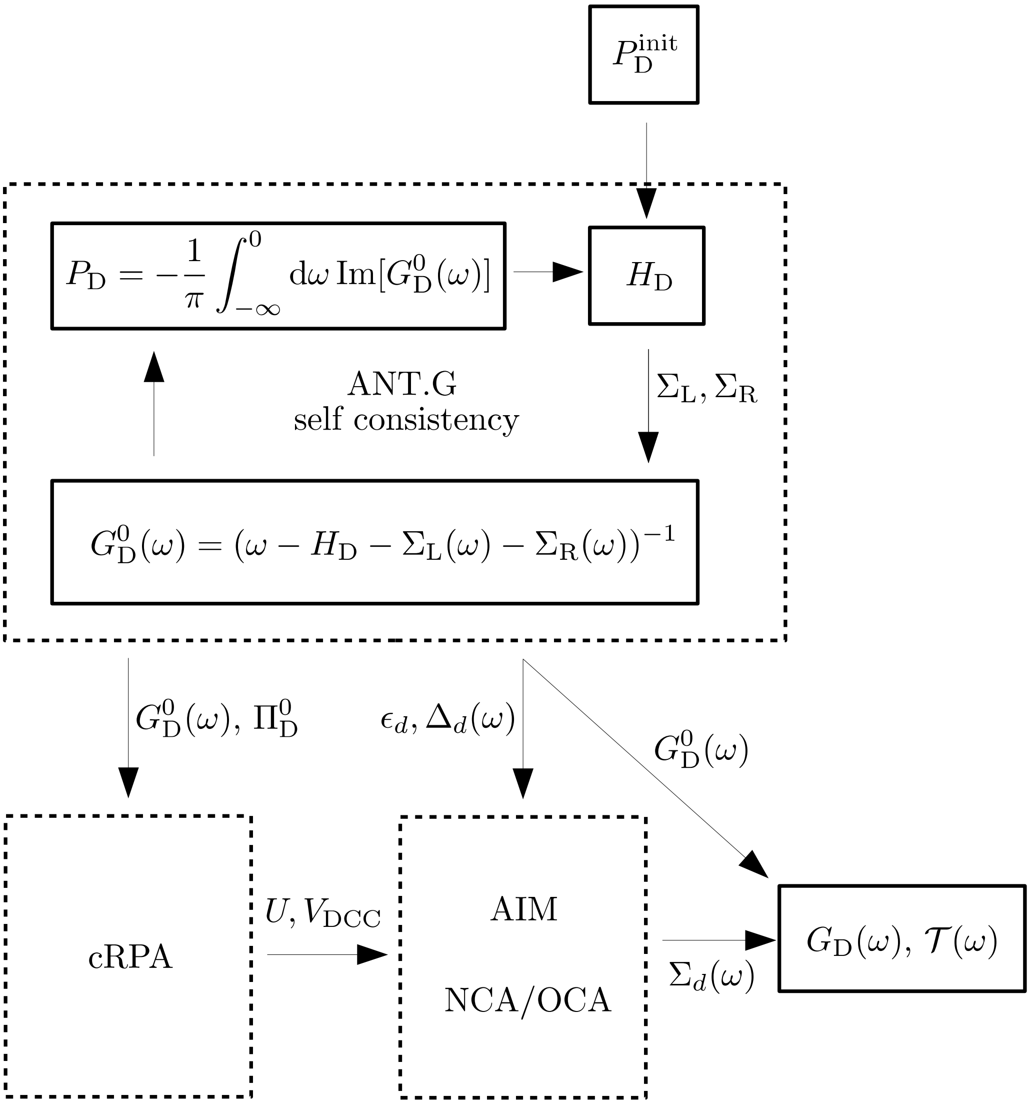

Figure 29: Computational scheme for the one-shot DFT+OCA calculations to determine the correlated transmission for the complete d shell. U is determined by a cRPA calculation, the remaining scheme is identical to that of chapter 3 (see Fig. 6).

	z^2	xz/yz	x^2-y^2	xy	$3d$ shell
LDA	1.63	1.53	1.74	1.50	7.93
LSDA	1.55	1.59	1.82	1.29	7.84
LDA+OCA	1.17	1.95	1.96	1.17	8.20
PBE (no spin)	1.64	1.54	1.76	1.48	7.96
PBE	1.12	1.85	1.90	1.10	7.82
PBE+OCA	1.01	1.99	1.99	1.03	8.01
PBE*+OCA	1.06	1.97	1.98	1.09	8.07

Table 7: Occupation of the respective d level and the complete d shell for different levels of approximation.

pseudopotential. The geometry is the same as in chapter 4. As DFT functionals, LDA/LSDA and PBE are used. The system is in an approximate spin 1 state (see Tab. 7). For all LDA, LSDA and spin-independent PBE, the orbital occupation is relatively spread out between the orbitals. For spin-dependent PBE, the improved description of electronic correlation leads to a localization of the spin in the z^2 and xy orbitals.

The hybridization functions are computed from the DFT calculation as presented in Fig. 30. They show the same features for LDA and PBE: the xz/yz orbitals hybridize most strongly, z^2 and xy show intermediate hybridization, and x^2-y^2 the weakest hybridization. The largest difference between LDA and PBE occurs in the xz/yz orbitals, where the hybridization from PBE is more than 0.01 eV below the LDA result. The hybridization of x^2-y^2 is slightly lower for PBE, while z^2 and xy are very close for both functionals.

The LDA results are similar to those obtained in chapter 3, where the hybridization function was computed for a slightly different geometry (see Fig. 7, and note that xy and x^2-y^2 are interchanged when comparing the results to chapter 3 because the new geometry is rotated by 45°, see Sec. 4.2). The updated geometry leads to a small reduction in hybridization strength (around 0.01 eV), and the effect is strongest for the z^2 orbital.

In order to define an AIM, we also require the partially screened Coulomb interaction. In contrast to chapter 3, U is not treated as a parameter, but is computed within the cRPA. The methodology was discussed in detail in chapter 4. A polarization region of 10 atoms is chosen, and the values of U can be found in Tab. 3. Note that although the computation of U based on an LSDA calculation is problematic (see Sec. 4.6), the LSDA is often used in the literature and will be presented for comparison. For a polarization region of 10 atoms, the U values appear to be physical, and while the LSDA fails to accurately describe the d levels, they will be treated by the impurity solver.

An AIM is defined by: the hybridization function $\Delta(\omega)$, the d level positions, the partially screened Coulomb interaction U, and the corresponding double counting correction. Only certain elements of the Coulomb interaction are taken into account, namely direct Coulomb

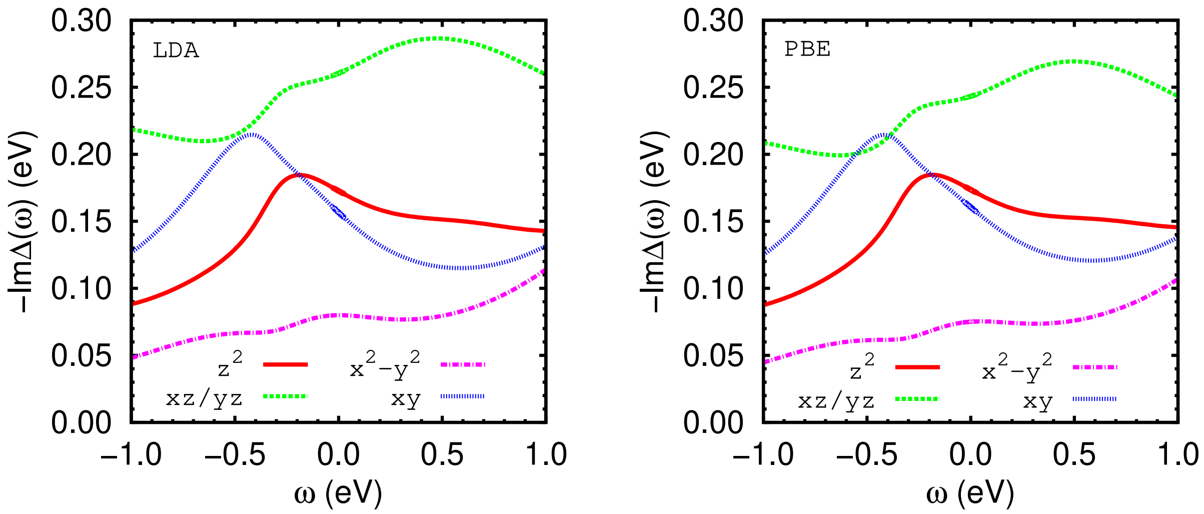

Figure 30: Imaginary part of the hybridization function for the Co 3d shell for LDA and PBE.

$U_{ii;jj}$ and exchange elements $U_{ij;ji}$. Other elements are relatively small and will be neglected, which is a typical assumption in impurity solver calculations[239].

The AIM is now solved using the OCA. The calculation temperature is set to $T = 0.001$ eV (11 K), which is a realistic temperature for Kondo-STM experiments. This is different from chapter 3, where the temperature was chosen for each d level to achieve Fermi liquid behavior. The temperature cannot be directly set to the desired value, but has to be gradually reduced in order for the OCA calculation to find the relevant pseudoparticles. This is done in 4 steps with temperatures 1 eV, 0.1 eV, 0.01 eV and 0.001 eV.

The resulting occupations of the LDA+OCA/PBE+OCA calculations can be found in Tab. 7. For LDA+OCA, the z^2 and xy orbitals are now much closer to half-filling, while the remaining orbitals are nearly completely filled. The deviation from half-filling by 0.17 indicates the presence of strong charge fluctuations. For PBE, the localization is much more pronounced, yielding virtually half-filled z^2 and xy orbitals. The choice of the double-counting correction is crucial here: LDA+OCA requires the orbital-dependent FLL DCC (see Eq. 75) to arrive at the correct spin state. The standard FLL DCC would result in an empty xy orbital, where all other d orbitals are completely filled. This can be understood by the strong anisotropy in the direct elements of U, where the xy orbital exhibits the strongest direct on-site interaction. If not appropriately corrected by the DCC, the strong Coulomb repulsion then leads to an emptying of the xy orbital. PBE, on the other hand, requires the standard FLL DCC (see Eq. 74) to reach the correct spin state. The orbital-dependent version yields a spin state where the xz/yz orbitals are half filled, while all remaining d orbitals are full. The reason for this behavior is not completely clear, and might be an overcorrection of the orbital-dependent FLL DCC. This highlights the importance of the choice of the DCC, particularly if the correct spin state is previously unknown. It would be highly desirable to develop a method where the DCC is exactly known. Fortunately, the choice of DCC will be slightly less important in the self-consistent

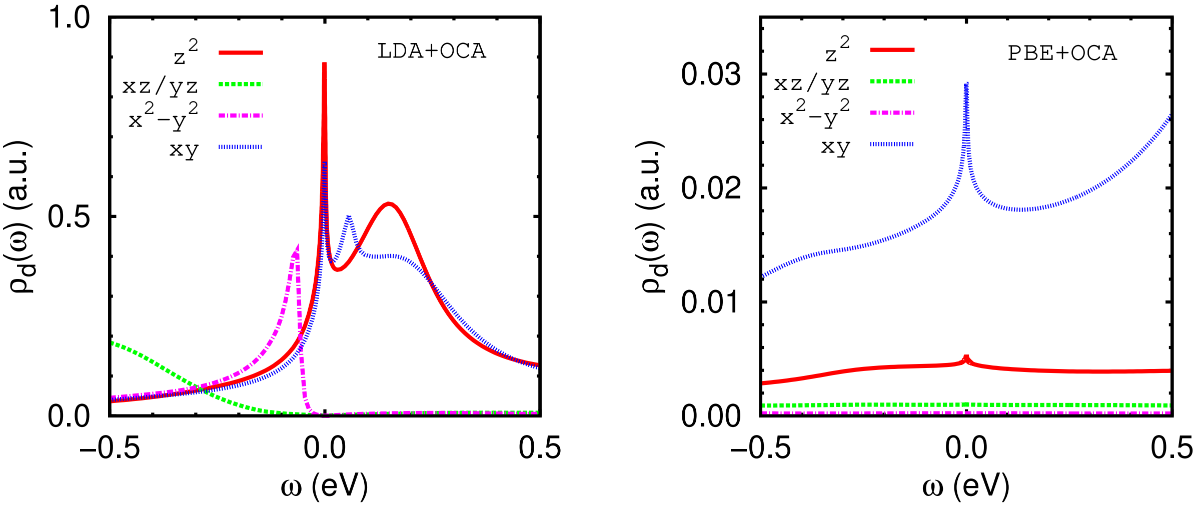

Figure 31: Spectral functions for the orbitals of the Co 3d shell for LSDA and PBE.

calculations conducted later in this chapter.

Fig. 31 shows the spectral functions obtained from the OCA calculation. For LDA+OCA, the Kondo peak is clearly developed for the z^2 and xy orbitals, and both lie in the left flank of another spectral feature at around 0.2 eV, which can be associated with the upper Hubbard band. This is also supported by the charge fluctuations present for z^2 and xy. The Kondo peak associated with xy is slightly smaller, since its direct on-site interaction U is higher and the hybridization around the Fermi level slightly smaller than for z^2. In order to assess the peak height, we look at the unitary limit (also see Sec. 3.2 and Sec. 3.3). Although only strictly defined for a single impurity, it still gives an indication for the expected size of the Kondo peak in a multi-orbital situation. For a single impurity and the given hybridization, a peak height of 1.8 1/eV and 2.0 1/eV would be expected for z^2 and xy, and the observed values lie a factor of 2 and 3 below for z^2 and xy, respectively.

For PBE+OCA, the Kondo peak is already visible, but barely developed and still very far from reaching the unitary limit. The xy orbital is associated with the stronger Kondo peak, whereas the z^2 orbital is associated with the weaker one, potentially because the direct on-site interaction U is slightly higher for z^2 than for xy, and although the hybridization of xy around the Fermi level is slightly weaker.

The filled orbitals do not show any spectral features around the Fermi level for LDA+OCA and PBE+OCA, which is the expected result.

The correlated transmission functions are presented in Fig. 32. The LDA+OCA transmission shows an asymmetric Fano feature tending towards a peak. A Fano-Frota fit yields $q = 1.75$, which is slightly higher than the experimental value (Ref. [32] reports $q = 1.13$), yet has the same symmetry. The difference might be due to the choice of the DCC, whose influence on the line shape can be considerable (see Sec. 3.3 and Ref. [70]). The Fano-Frota fit yields $\Gamma_F = 1.6$ meV, from which the half-width of the Fano feature can be determined according

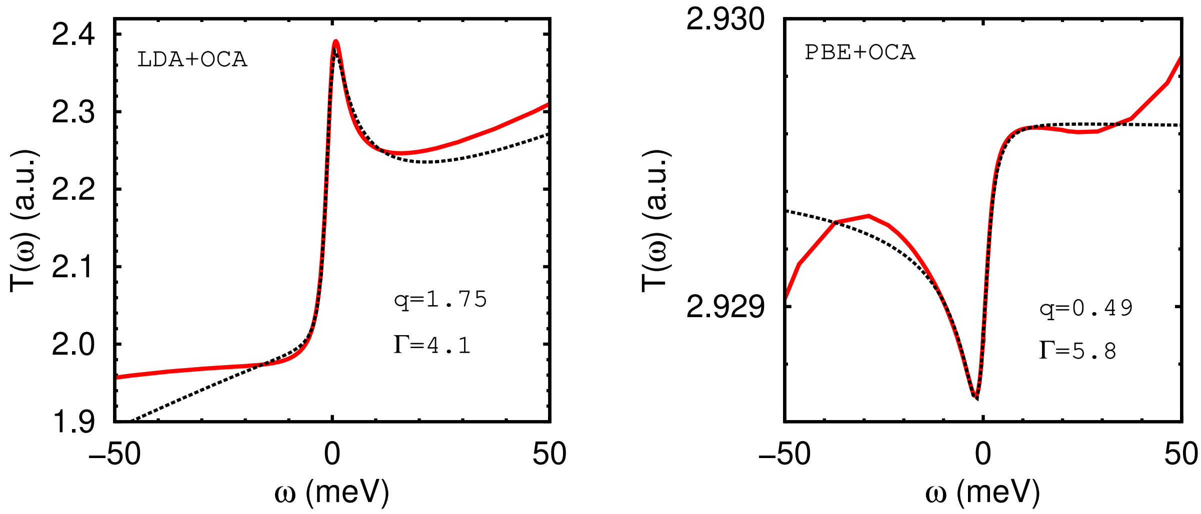

Figure 32: Transmission functions for one-shot LDA+OCA and PBE+OCA, where the linear and quadratic background are subtracted for the latter. Frota fits (dotted black lines) yield the q factor and the half-width parameter Γ of the Fano-Frota feature.

to $\Gamma = 2.54\Gamma_{\mathrm{F}}$. If no temperature broadening of the Kondo peak were present, this would correspond to a Kondo temperature of 47 K, in good agreement with the experimental value of 53 K[32]. However, since the Kondo peak is already pronounced, but not yet fully developed, a small temperature broadening is likely present and the resulting Kondo temperature is slightly lower.

For PBE+OCA, the transmission feature is several orders of magnitude smaller than for LDA+OCA, in accordance with the much weaker Kondo peak in the spectral function. In order to resolve the feature, a Fano-Frota fit (see Sec. 3.1) with additional linear and quadratic terms was required. The line shape is an asymmetric Fano line shape tending towards a dip, with $q = 0.49$, much lower than for LDA+OCA and than observed in experiment. This can be understood in context of the results of Sec. 3.7: because the Kondo peak is barely developed, direct tunneling through the Kondo peak is much weaker, and indirect processes via substrate states are responsible for the observed feature. This leads to more dip-like line shapes than in the case of a strongly pronounced Kondo peak. The Fano-Frota fit also yields the half width $\Gamma = 5.8$ meV, which is higher than the LDA+OCA value. This can only be explained by a strong temperature broadening (also see Fig. 18). In order to determine the Kondo temperature, a further decrease of calculation temperature would be required.

5.1.2 PBE+OCA with lower U

While LDA+OCA yields line shape and Kondo scale in close agreement with experiment, the computation of U using the LSDA is highly problematic (see chapter 4), and the LSDA is not capable of capturing the correct spin state. PBE, on the other hand, already captures the spin state of the d shell correctly, but the Coulomb interaction U is considerably too high, because

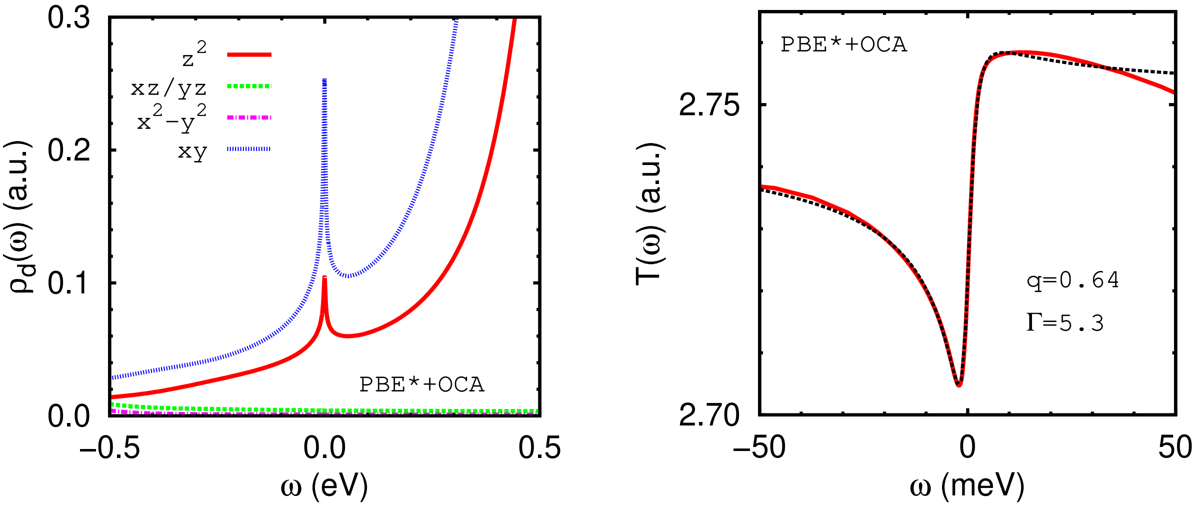

Figure 33: Spectral function and transmission function for PBE*+OCA.

screening contributions from outside of the polarization and from high-energy states could not be included (see Sec. 4.6), resulting in a very small Kondo scale. This section aims to combine the best of both worlds: the starting point of the calculation will be the PBE functional, but another, much smaller U parameter is chosen. The U is chosen as follows: chapter 4 has shown that the cRPA is not converged with respect to the size of the polarization region, and that a further increase of the polarization region would likely lead to a further reduction in U. We also observed that the direct on-site elements of U were less spread-out for methods with higher-level correlation (like scDFT+U and HSE). We therefore choose U obtained from scPBE+U, but reduce its direct elements by a factor of two, resulting in $U_{d_{z^2}} = 4.86$, $U_{d_{xz/yz}} = 4.73$, $U_{d_{x^2-y^2}} = 4.62$ and $U_{d_{xy}} = 4.77$ for the direct on-site elements, while the exchange elements are kept unchanged. This is closer to U values reported in the literature resulting in the correct Kondo scale (see Ref. [70] and Ref. [69]). This choice will be further corroborated by the results later in this chapter (see Sec. 5.2.4), although it is a departure from a complete ab-initio description. This method will henceforth be labeled PBE*+OCA.

The AIM is now defined by the hybridization function and the d level positions taken from a PBE calculation, while U is obtained as described in the previous paragraph. The occupations are shown in Tab. 7. The spin is localized in the z^2 and xy orbitals, which are closer to half-filling than for PBE and LDA+OCA, but not as close as for PBE+OCA. The choice of DCC plays a slightly smaller role here: since the higher-level correlation of scPBE+U leads to less spread-out direct elements of U, both standard and orbital-dependent FLL DCC localize the spin in the z^2 and xy orbitals, and there are only small quantitative differences in the occupations. Since it is more commonly used in the literature, the standard FLL DCC has been chosen here and for the remainder of this work.

The impurity spectral function and transmission functions are presented in Fig. 33. The Kondo peak is clearly developed for the xy and z^2 orbitals, but far from the unitary limit. While hybridization and U of both orbitals carrying a Kondo peak are comparable, xy shows stronger charge fluctuations than z^2 (occupation of 1.09 to 1.06, see Tab. 7), and is therefore associated with the larger Kondo feature, pointing to the importance of charge fluctuations.

The Kondo peaks are less pronounced than those of the LDA+OCA calculation. Although the U of PBE*+OCA is lower than that of LDA+OCA, charge fluctuations are also considerably smaller, leading to an overall smaller Kondo scale. The transmission function shows an asymmetric Fano-feature tending towards a dip, with $q = 0.64$, which is higher than that of PBE+OCA, and thus indicates that slightly more tunneling occurs through the Kondo peak. Also note that the transmission feature is likely due to the z^2, since it couples significantly more strongly to the tip than the xy orbital (see Sec. 3.3), although the latter is associated with the higher Kondo peak. The half-width is $\Gamma = 5.3$ meV, but significant temperature broadening of the feature must be present. Therefore no statement can be made about the Kondo temperature.

Although PBE*+OCA does not lead to larger Kondo scales as initially anticipated, it produces sizable Kondo peaks. It will also be used for self-consistent calculations later in this chapter, where charge fluctuations will play a smaller role, and the reduced U will have a greater influence.

5.1.3 Discussion

One-shot DFT+OCA serves as a good starting point for more advanced calculations. It is capable of describing the influence of strong electronic correlations on the electronic structure and the transmission properties of the system, and results in Fano line shapes in the transmission function. LDA+OCA yields a strongly developed Kondo peak, and a transmission feature close to experimental data, albeit slightly more peak-like. PBE+OCA, on the other hand, results in a very small Kondo scale and a barely visible transmission feature between asymmetric Fano line shape and a dip. This is likely due to the high value of the Coulomb interaction U obtained from cRPA and from barely any charge fluctuations. PBE*+OCA produces an intermediate result: a clearly discernible Kondo peak which is still far from being fully pronounced, and an asymmetric Fano feature tending towards a dip, which is already closer to experiment than PBE+OCA.

There are certain drawbacks, however. The correlated self energy is only added to the d shell, and the remaining electronic structure is fixed to the non-interacting value. That way, the surrounding electrons cannot adapt to the new environment posed by the correlated self energy Σ_d.

Another problem is related to that: the d level positions and the hybridization functions are obtained from a spin-independent calculation, and both spin-independent PBE and LDA yield an occupation spread out over all d orbitals, instead of z^2 and xy being nearly half-filled and the remaining orbitals nearly filled (see Tab. 7). It would be highly desirable to extract AIM parameters from an electronic structure where the orbital occupation is already correctly captured. These issues will be addressed in the following sections, by implementing different levels of self-consistency in the DFT+OCA cycle.

5.2 Charge self-consistency for DFT+OCA

As discussed at the end of the previous section, one-shot DFT+OCA does not include any feedback of the correlated self energy on the electronic structure of the complete system. This gap will be closed in this section: the electronic structure of the device region will be relaxed under the influence of the correlated self energy. The relaxed electronic structure in turn defines a new AIM, which can be solved for an updated correlated self energy. This will be repeated until convergence is reached, and will be called the charge self-consistency cycle.

According to Ref. [240], a calculation can be called charge self-consistent if charge can be exchanged between the two subsystems, the electronic structure of the two subsystems affects each other, and the total electronic structure is at a stationary point of the thermodynamics. The importance of achieving charge self-consistency in the context of DFT+DMFT has been pointed out in the past[61;239;241;242;243;244;245;246;247]. Ref. [239] found that the charge self-consistency significantly shifts the position of the Hubbard bands of Ce_2O_3 and the γ phase of metallic Ce. Ref. [244] observed that the self-consistent inclusion of correlation effects significantly improves both structural and magnetic properties for the iron-pnictide superconductor LaFeAsO. Ref. [247] finds a significant occupation redistribution for a single layer of $SrVO_3$ when charge self-consistency is achieved.

This section will introduce the charge self-consistency cycle in the context of our DFT-based transport code augmented by local correlations. We will discuss the computational and technical aspects of implementing charge self-consistency, and present results for Co@Cu(001).

5.2.1 Computational and technical aspects

The computational scheme of the charge self-consistency cycle is shown and described in Fig. 34. The charge self-consistency cycle is continued until convergence is reached, but no convergence criterion has been defined yet. The convergence of various system properties will be investigated, in order to verify if there is different convergent behavior for occupation, d level positions, hybridization functions and transmission functions.

The ANT.G code had to be extended in order to account for effects of charge self-consistency. The module which computes the density matrix by integration along the Matsubara axis has been modified so that it now can read in the correlated self energy and compute the interacting GF.

One more technical aspect has to be discussed. The output of the OCA is the correlated self energy on the real axis $\Sigma_d(\omega)$. ANT.G, however, computes the density matrix by integration of the system's Green's functions along the Matsubara axis. In order to include the effects due to the correlated self energy in the ANT.G calculation, $\Sigma_d(\omega)$ has to be continued to the

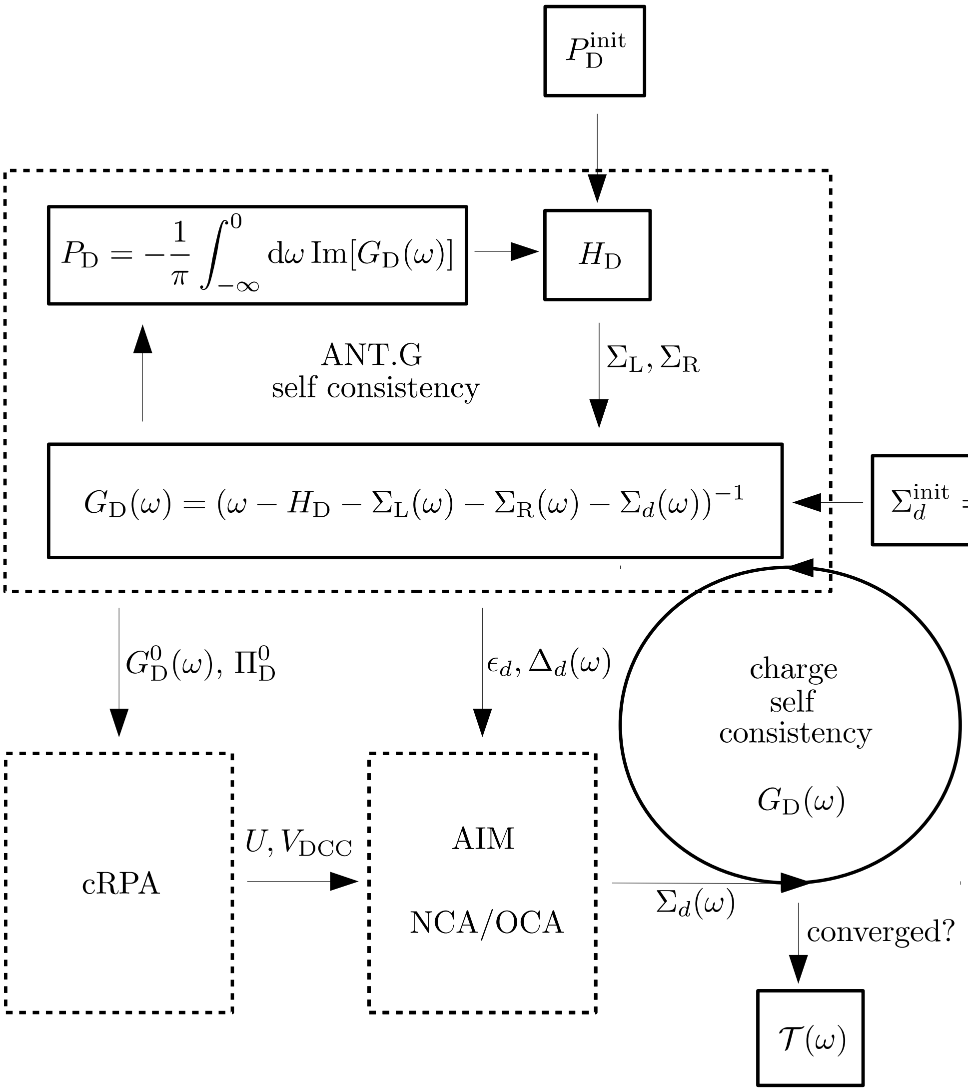

Figure 34: Computational scheme of the charge self-consistency cycle to determine the correlated transmission for the complete d shell. First, the non-interacting GF $G_D^0(\omega)$ is determined self-consistently, employing the ANT.G code. The Coulomb interaction within the d shell is computed by cRPA only once, using the non-interacting GF G_{D}^0. An AIM is defined by the energy of the d level and the hybridization function $\Delta_d(\omega)$, the Coulomb interaction U and double counting correction V_{DCC}. The AIM is solved within the OCA, and the correlated self energy $\Sigma_d(\omega)$ is determined. The correlated GF $G_{\mathrm{D}}(\omega)$ and an updated density matrix are determined by the ANT.G self consistency, and new AIM parameters are extracted. When convergence of the charge self consistency cycle is reached, the correlated transmission $\mathcal{T}(\omega)$ can be calculated.

imaginary axis. We stress that this is a much simpler task than the continuation of a quantity from the Matsubara to the real axis, as has to be done in CTQMC calculations. A program was written that determines $\Sigma_d(\mathrm{i}\omega)$ on the imaginary axis by solving Cauchy's integral formula:

$$f(a) = \frac{1}{2\pi\mathrm{i}} \oint_\gamma \frac{f(z)}{z-a} \mathrm{d}z, \tag{118}$$

where $f(z)$ is a holomorphic function defined over the complex plane, γ is a closed curve, and z and a are complex numbers, where a has to lie within the boundaries of γ. Here, γ is given by the real axis and a semi-circle that encloses the upper complex half-plane, where the latter does not contribute to the integral if $\Sigma_d(\omega)$ decays sufficiently fast for large ω. This is not the case without a workaround: the real part of $\Sigma_d(\omega)$ does not decay to zero, but to a constant, the so-called Hartree shift Σ_{Hartree}. In order to guarantee convergence of Cauchy's integral formula, the Hartree shift has to be obtained by fitting and has then to be subtracted from $\Sigma_d(\omega)$:

$$\Sigma_d^{\text{input}}(\omega) = \Sigma_d(\omega) - \Sigma_{\text{Hartree}}. \tag{119}$$

$\Sigma_d^{\text{input}}(\omega)$ decays sufficiently quickly for large ω, Eq. 118 can be easily applied by carrying out the integral along the real axis, and Σ_{Hartree} can be added back to $\Sigma_d^{\text{output}}(\mathrm{i}\omega)$ after the continuation.

Since $\Sigma_d(\omega)$ is defined on a discrete mesh, its low and high energy tales have to be determined by a fit. For the real part, both flanks are fit by a single Lorentzian for each d level, also in order to obtain the respective Hartree shift. The upper and lower flanks of the imaginary part of $\Sigma_d(\omega)$ are fit separately by Lorentzian functions. The fitting of the flanks can be relevant to the overall result: Ref. [239] points out that a careful summation of the high-frequency tail of $\Sigma_d(\omega)$ is necessary to achieve reliable results, albeit in the context of computing the total energy.

In realistic OCA calculations, the fitting of the flanks is not completely straightforward because unphysical artifacts appear for very low and very high frequencies, likely due to edge effects (see Fig. 45 in appendix C). The appropriate fitting range has to be chosen manually for each calculation, and this process cannot be easily automatized. Two examples of the continued self energy on the Matsubara axis are presented in Fig. 46 of appendix C. After the continuation, the high-energy flank of $\Sigma_d(\mathrm{i}\omega)$ has to be also fit by a Lorentzian, since the integration of the GF on the Matsubara axis in ANT.G goes up to very high frequencies. This fit is of very high quality and unproblematic. Overall, the analytical continuation requires a large amount of manual input and fitting. A further automatization would be highly desirable, but is not straightforward.

5.2.2 Results

The charge self-consistency cycle described in the previous section is now applied for LDA+OCA, PBE+OCA, and PBE*+OCA. The choice of DCC remains the same as for one-shot DFT+OCA, since both methods use the same U parameters: LDA+OCA employs the orbital-dependent FLL DCC, while PBE+OCA and PBE*+OCA utilize the standard FLL DCC. Fig. 35 presents ϵ_d, occupations n_d of the OCA and the DFT steps and the imaginary part of the hybridization function at the Fermi level $-\text{Im}\Delta(\epsilon_\text{F})$ for different iterations of the charge self-consistency cycle. The zeroth iteration refers to the pure DFT calculation for the DFT step, and to the OCA calculation with AIM parameter obtained from the pure DFT calculation, as discussed in Sec. 5.1. The zeroth order result is omitted in some of the graphs to increase the visibility of changes due to the self-consistency process.

For ϵ_d, a sharp increase is observed in the second iteration for all three functionals and all d orbitals, and a subsequent decay for all further iterations. Although convergence is not yet fully reached after 10 iterations, it is clear that all ϵ_d converge to a constant value, which lies below the pure DFT value (zeroth iteration). The relative order of ϵ_d is maintained over all iterations of PBE+OCA and PBE*+OCA, where ϵ_d of the half-filled orbitals (z^2 and xy) lies above that of the filled orbitals (xz/yz and x^2-y^2). For LDA+OCA, the order of different ϵ_d changes in the first four iterations of the self-consistency cycle, but becomes stable after the fifth iteration, and all ϵ_d lie within 0.1 eV for the final iteration.

The first step of the charge self-consistency leads to a considerable drop of the OCA occupation for the z^2 and xy orbitals (see Tab. 7 for comparison), leading to a significant reduction of charge fluctuations and moving both orbitals closer to half-filling. This effect is particularly pronounced for LDA+OCA and PBE*+OCA. Further iterations of the charge self-consistency cycle have a much smaller effect. For LDA+OCA and PBE+OCA, only minor changes of occupation occur after the fifth iteration. For PBE*+OCA, the charge self-consistency leads to a slight increase of occupation, moving away from half-filling and increasing the presence of charge fluctuations, but the occupation always remains below that of the zeroth iteration. The filled orbitals xz/yz and x^2-y^2 behave very similarly for all functionals. The minimum of occupation is reached for the second iteration, and all further iterations lead to a gradual increase of occupation, which eventually seems to converge to a constant.

The first iteration of the DFT step brings the orbitals much closer to half-filling than for the pure DFT calculation (see Tab. 7 for comparison). For the remaining iterations, the occupation of the DFT step does not follow the same pattern as the OCA occupation for the z^2 and xy orbitals. A local maximum of occupation is reached for z^2 and xy after 2 iterations for PBE+OCA and PBE*+OCA and 3 or 4 iterations for LDA+OCA. In all further iterations, the occupation falls off in a step-like fashion, which was not observed for the OCA occupation. For the z^2 orbital of LDA+OCA and the z^2 and xy orbitals of PBE*+OCA, the DFT and OCA occupations seem to converge against each other, as per the expectations. This is not the case for PBE+OCA and the xy orbital in the LDA+OCA calculation, however, and it remains unclear why the OCA and the DFT occupations deviate. The DFT occupations of the filled orbitals xz/yz and x^2-y^2 behave similarly to those of the OCA step. After inconsistent behavior in the first three iterations, the occupation slowly increases for all functionals. This increase also occurs in small

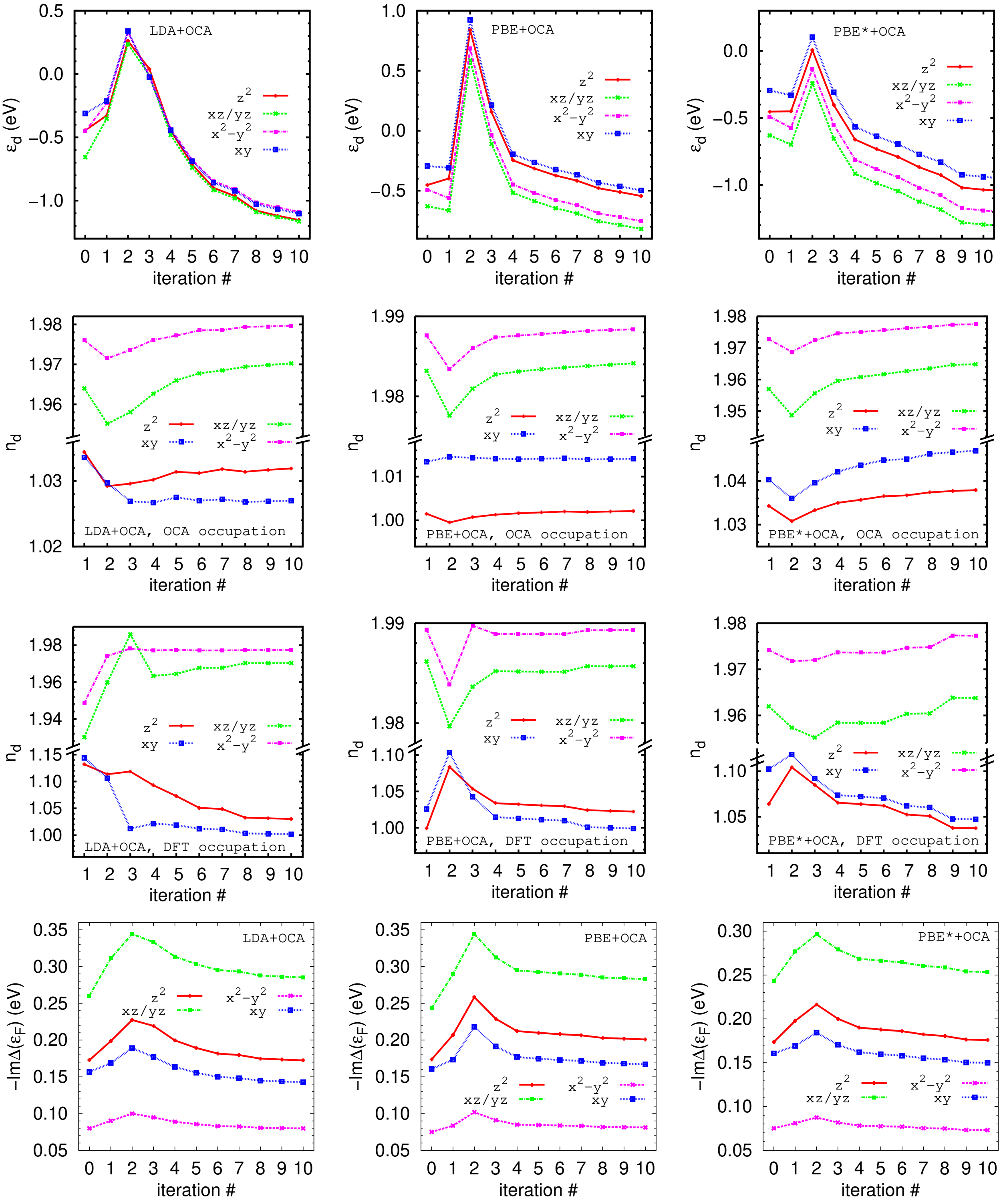

Figure 35: d level positions, OCA occupations, DFT occupations and the imaginary part of the hybridization function at the Fermi level for different iterations of the charge self-consistency cycle. Zeroth order occupations are not shown for better visibility and can be found in Tab. 7.

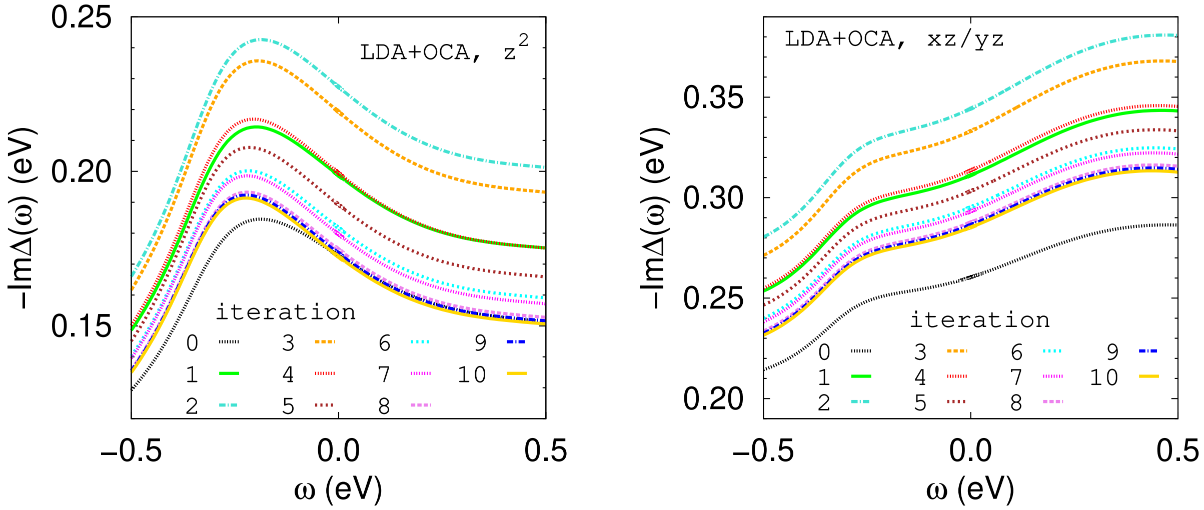

Figure 36: Imaginary part of the hybridization function for different iterations of the charge self-consistency cycle for the z^2 and the xz orbitals.

steps. The filling of the orbitals is very similar to that of the OCA steps.
The imaginary part of the hybridization function at the Fermi level initially increases for all functionals and d levels, reaches its maximum at the second iteration, and then gradually falls off. Although convergence is not yet fully reached after 10 iterations, it clearly converges to a constant value. This value can either lie above (e.g. xz/yz for all functionals), below (e.g. xy for LDA+OCA and PBE+OCA), or very close (e.g. z^2 for LDA+OCA) to the zeroth order hybridization. In Fig. 35, only the value of the imaginary part of the hybridization function at the Fermi level is presented. In Fig. 36, the energy dependence of the imaginary part of the hybridization function is plotted for two selected orbital (z^2 and xz/yz) and LDA+OCA. The charge self-consistency does not lead to large qualitative changes, and different iterations are mostly offset by a shift. Therefore it typically suffices to study the hybridization at the Fermi level to gain insight on the effect of charge self-consistency. Small qualitative differences can be observed when comparing the zeroth order and the tenth order for the z^2 orbital: while their right flank nearly coincides, the peak around -0.2 eV is less pronounced for the zeroth iteration than for the tenth.
Fig. 37 shows impurity spectral functions for the z^2 and xy orbitals for different iterations of the charge self-consistency cycle. The xz/yz and x^2-y^2 orbitals do not carry a Kondo peak and are therefore not shown. For LDA+OCA, the charge self-consistency leads to an initial decrease of the Kondo feature in both orbitals, and all iterations beyond the third are associated with very similar Kondo peaks. For PBE+OCA, the charge self-consistency leads to an initial increase and subsequent decrease of the height of the Kondo feature, while for PBE*+OCA, an initial decrease and subsequent increase of the Kondo peak is observed.
In order to compare the Kondo peaks quantitatively, Frota fits were performed according to Eq. 92, and the amplitude of the Frota line shape is plotted in the bottom panels of Fig. 37.

For LDA+OCA and PBE*+OCA, the amplitude of the Kondo peak behaves very similarly to the OCA occupation of Fig. 35: the higher the orbital occupation in the OCA step, the more the Kondo peak is pronounced, again pointing to the strong influence of charge fluctuations. For PBE+OCA, however, the OCA occupation only very slightly varies, but the amplitude of the Kondo peak drastically changes for different iterations. It behaves more similarly to the hybridization function shown in Fig. 35. This, on the other hand, is not observed for LDA+OCA and PBE*+OCA. This points to a complex interplay of charge fluctuations, hybridization strength and U parameter.

The Kondo peak is most pronounced for PBE*+OCA, the method associated with he lowest U parameter, and least pronounced for PBE+OCA, associated with the highest U parameter. This was different for the one-shot calculation of Sec. 5.1, where the strong charge fluctuations for LDA+OCA caused the associated Kondo peak to be more pronounced than that of PBE*+OCA, although the latter is associated with the lower U. The self-consistency dampens the charge-fluctuations for all functionals, but more strongly for LDA+OCA than for PBE*+OCA. For all functionals, the Kondo peaks are distant from the unitary limit, and a further decrease in temperature should lead to more pronounced Kondo features.

Fig. 38 shows transmission functions for LDA+OCA, PBE+OCA and PBE*+OCA. In order to compare the transmission functions quantitatively, Fano-Frota fits according to Eq. 93 were performed, adding a linear and quadratic term to account for the transmission background in order to determine the transmission amplitudes, q parameters and half-width parameters Γ. These are also shown in Fig. 38.

For LDA+OCA and PBE*+OCA, the charge self-consistency initially leads to significantly smaller transmission features, while for PBE the transmission amplitude increases. The transmission amplitude generally follows the amplitude of the Kondo peak of the z^2 orbital (see Fig. 37, and note that the nth iteration of the transmission is based on the (n-1)th iteration of the spectral function, so features appearing in the spectral function appear in the subsequent iteration of the transmission). The z^2 orbital dominates the transmission because it has a strong overlap with the s and p_z orbitals of the STM tip, while the xy orbital does not have any (also see Sec. 3.9).

For all functionals, a drop of q occurs in the first few iterations. This effect is particularly strong for LDA+OCA. This can be explained in the context of Sec. 3.7 and the model of Sec. 3.5: the charge self-consistency leads to much smaller Kondo peaks; therefore to less direct tunneling through the Kondo peak, so that indirect interactions via substrate states dominate. This leads to more dip-like line shapes. After the fifth iteration, the value of q barely changes, and the small differences might be due to the quality of the fit since the transmission signal is relatively weak. The final value of q (0.52 for LDA+OCA, 0.48 for PBE+OCA and 0.54 for PBE*+OCA) lies considerably below the experimental value of $q = 1.13$ reported in Ref. [32]. The closest agreement with experiment is found for the first iteration of LDA+OCA, which uses the zeroth order self-energy Σ_d but already incorporates its effect on the electronic structure of the system,

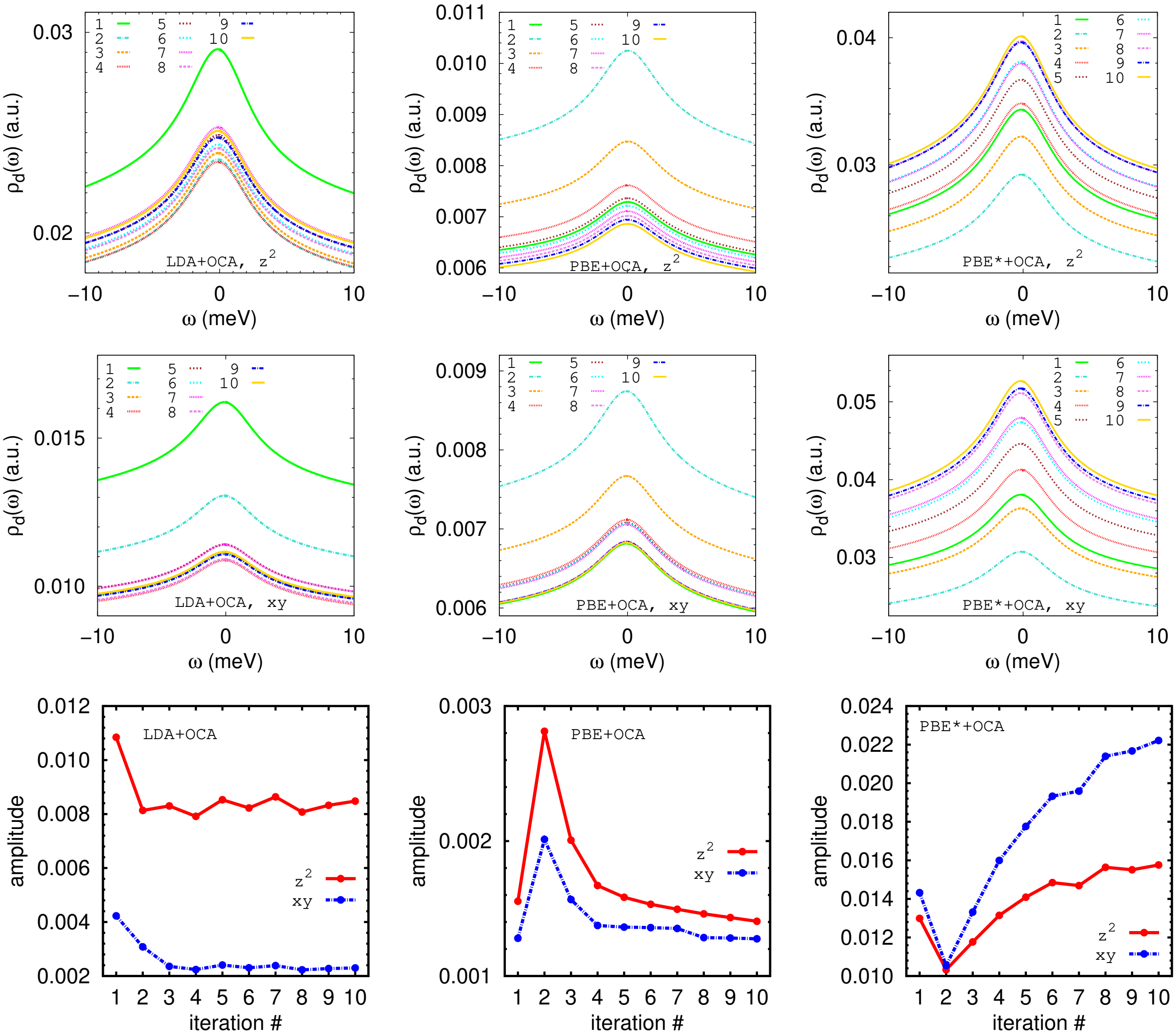

Figure 37: Impurity spectral functions for z^2 and xy (the zeroth order results can be found in Fig. 31 and Fig. 33) and the amplitude of the Kondo peak fitted according to Eq. 92.

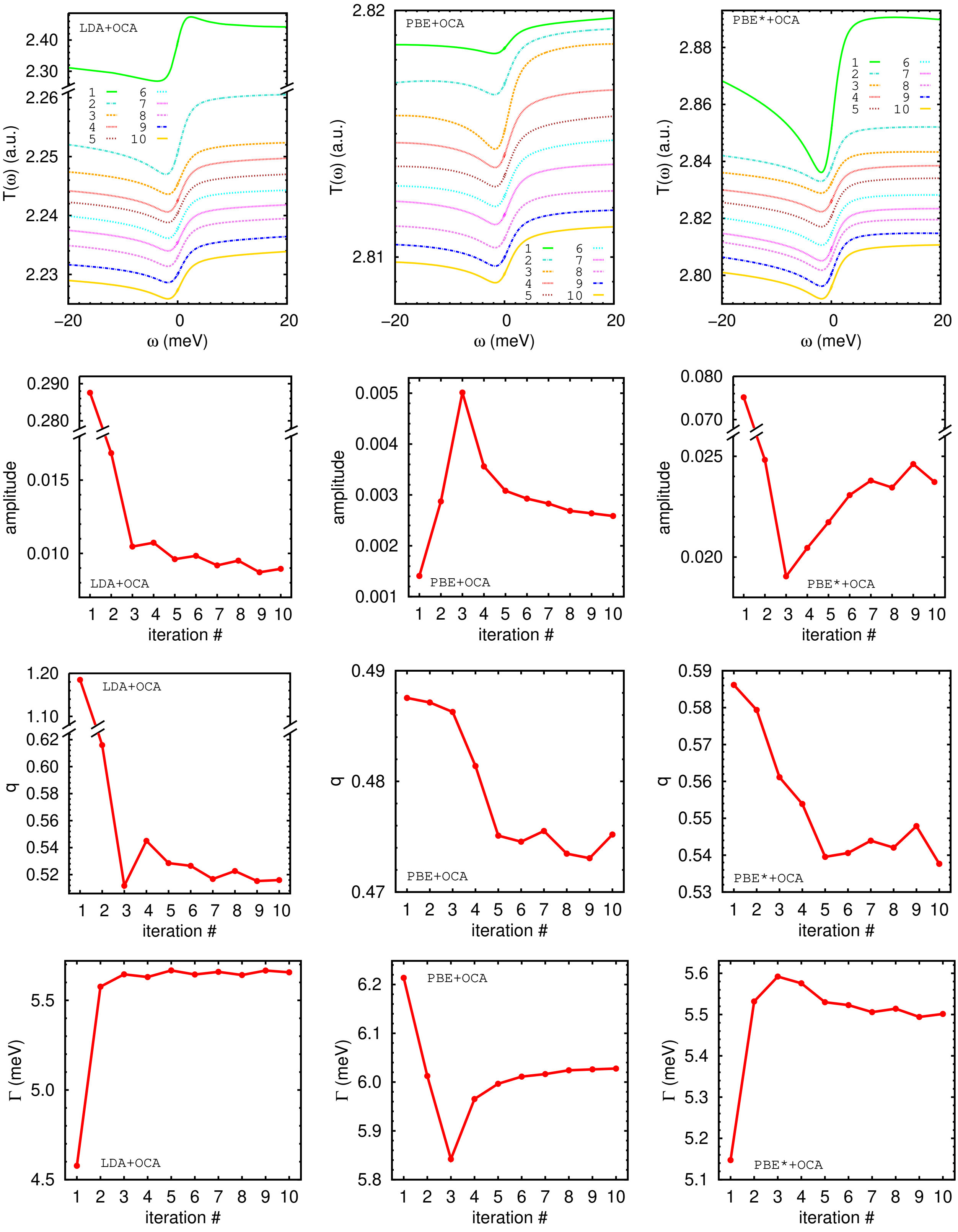

Figure 38: Transmission functions for a different number of iterations of the charge self-consistency cycle. Transmission functions have been offset, and linear and quadratic background terms have been subtracted for better visibility. Transmission amplitude, q factor and half-width $\Gamma = 2.54\Gamma_F$ were obtained by Frota fits according to Eq. 93.

yielding a transmission feature with q=1.18.

The half-width Γ behaves inversely to the amplitude of the transmission feature (and, correspondingly, to the amplitude of the spectral function): smaller Kondo peaks are associated with higher width parameters. The half-width is influenced by two major factors: the Kondo temperature T_K, which is given by the half-width of the Kondo peak at $T = 0\ K$; and the temperature broadening if the Kondo peak is not fully developed. These two effects are competing: if, for instance, charge fluctuations become smaller (as is the case going from the first to the second iteration for LDA+OCA), the Kondo temperature also becomes smaller, which would lead to smaller half-widths of the Kondo peak at $T = 0\ K$. The temperature broadening, on the other hand, increases: since the calculation temperature is fixed, a lower Kondo temperature means that the Kondo peak is further away from being fully pronounced, as indicated by the lower amplitude[248], leading to a stronger temperature broadening. It appears that the temperature broadening is more relevant, although the overall effect is not very large, and the width parameter is similar for all functionals and iterations.

5.2.3 Discussion

Charge self-consistency has a sizable effect on the electronic structure of the Co@Cu(001) system. It leads to: lower d level positions ϵ_d for all functionals; occupations closer to half-filling in both the OCA and DFT step, particularly for LDA+U and PBE*+OCA; and changes in the hybridization function. The effect of charge self-consistency on the Kondo scale and the resulting transmission line shapes is large. A strong connection is observed between the presence of charge fluctuations in the OCA step and the size of the resulting Kondo peak, and resulting Kondo peaks have low amplitudes and are far away from the unitary limit. This leads to dip-like transmission features, since direct tunneling through the Kondo peak is improbable, and interactions of the Kondo peak with substrate states is more relevant. The transmission feature is associated with the Kondo peak in the z^2 orbital because of the symmetry of the STM setup.

The charge self-consistency cycle seems to be stable and convergent: no considerable oscillations are observed, and all studied quantities seem to trend to a constant value, although convergence is not fully reached after 10 iterations. The numerical effort is considerably higher than for one-shot DFT+OCA because an AIM has to be solved for each iteration, and the technical aspects discussed in Sec. 5.2.1 require a lot of manual input.

5.2.4 *U* from charge self-consistency calculation

This section performs cRPA calculations to determine the partially screened Coulomb interaction U for different iterations of the charge self-consistency cycle. We stress that the complete charge self-consistency cycle is done with fixed U obtained as described in Sec. 5.1.1, and U is not updated in each cycle (this will be done in Sec. 5.3). By doing so, the effects of charge

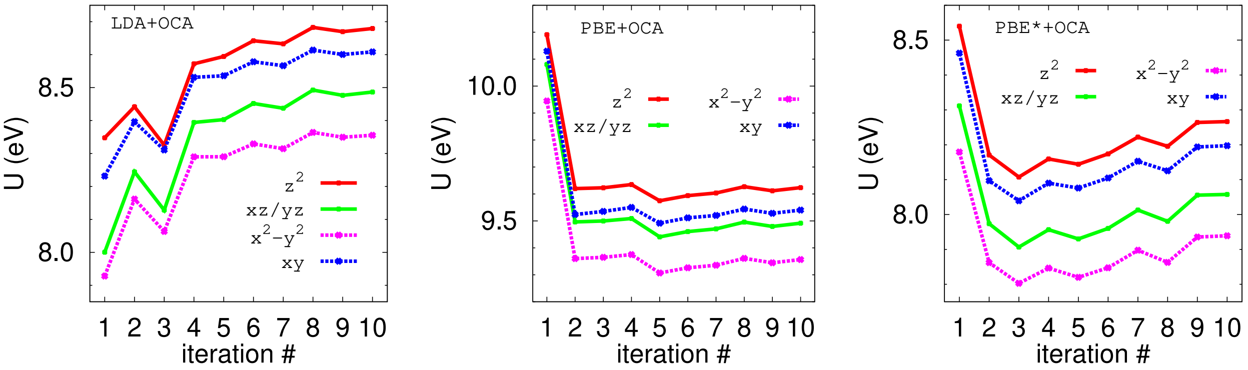

Figure 39: Interaction U computed for different iterations of the charge self-consistent calculation. The zeroth order is omitted for better visibility and can be found in Tab. 3.

redistributions due to the charge self-consistency alone on the computation of U can be studied. Fig. 39 plots the direct on-site elements of U obtained from different iterations of the charge self-consistency cycle. The first iteration leads to an increase of U for all functionals, and reduces the spread between different elements of U. This was also observed for the HSE functional and scDFT+U in Sec. 4.2 and Sec. 4.3, indicating that higher-level correlation leads to less spread-out U parameters. The relative order of the direct on-site elements is unaffected by the charge self-consistency, and the nearly half-filled orbitals z^2 and xy are associated with higher U than the nearly filled orbitals xz/yz and x^2-y^2 for all iterations, which was also observed in Sec. 4.2 for higher-level functionals.

For LDA+OCA, the charge self-consistency leads to an overall increase of U. Small oscillations occur, but U seems to converge to a constant. LDA+OCA behaves similarly to the other methods, indicating that the addition of the correlated self energy remedies the problems of pure LDA in a cRPA calculation (see Sec. 4.4). For PBE+OCA, U drops in the second iteration, and only small changes are observed for all further iterations. For PBE*+OCA, a drop of U in the second iteration, and a subsequent slow increase of U towards a constant, accompanied by small oscillations, are also observed.

For the tenth iteration, PBE+OCA is associated with the highest direct on-site U, whose elements are very similar in size to those obtained from a self-consistent LDA+U and PBE+U calculation (see Sec.4.3), ranging from 9.36 to 9.62 eV, while those of LDA+OCA range from 8.36 t0 8.68 eV. The lowest U is obtained for PBE*+OCA, ranging from 7.94 to 8.27 eV. The method with the smallest U^{input} also yields the smallest U in the cRPA calculation. This can be explained by two effects: first, the Hubbard bands associated with the respective d level are pushed away less from the Fermi level when U^{input} is lower. Second, the effect of the Kondo feature itself is now included in the electronic structure, and might therefore directly affect screening processes close to the Fermi level. This effect is expected to be small in this situation, however, due to the small Kondo peaks observed in Fig. 37.

Overall, the U parameters obtained from the charge self-consistent calculations are still considerably too high. While charge self-consistency has a sizable effect on U, the spatial and energy convergence of the cRPA also has to be improved (see detailed discussion in Sec. 4.6).

5.3 Charge-U self-consistency for DFT+OCA

In the previous section, the charge self-consistency cycle was introduced, by taking into account the feedback of the correlated self energy on the electronic structure of the full system self-consistently. The partially screened Coulomb interaction U, however, was only computed once based on the initial DFT calculation for LDA+OCA and PBE+OCA, and then estimated for PBE*+OCA as described in Sec. 5.1.2. This section will go one step further to a full ab-initio description of the system and compute U for each step of the charge-U self-consistency cycle, employing the cRPA methodology introduced in chapter 4.

The computation of U via cRPA was discussed in detail in chapter 4, and found a strong dependence on the functional used. It also found that higher level correlation leads to higher and less spread-out U parameters. The effect of pure charge self-consistency on the interaction U was studied in Sec. 5.2.4.

In order to investigate the influence of the inclusion of U in the self-consistency cycle, the ANT.G module computing the non-interacting polarizability from the non-interacting GF was extended to read in the correlated self energy and compute the interacting GF. From that, the interacting polarizability can be computed according to Eq. 97. The full computational scheme is shown and described in Fig. 40.

5.3.1 Results

The charge-U self-consistency cycle described in Fig. 40 is applied for LDA+OCA, PBE+OCA, and PBE*+OCA. The starting value of U is the same as for the charge self-consistency cycle (see Sec. 5.2) but is now updated for each iteration. Note that PBE*+OCA is only included to study the convergence of the algorithm: PBE+OCA and PBE*+OCA only differ by the initial value of U, and should yield identical final results if the algorithm were to converge.

Fig. 41 shows the direct on-site elements of the interaction U for different iterations of the charge-U self-consistency. The first two iterations lead to a strong increase of U for LDA+OCA and PBE*+OCA, while for PBE+OCA, it increases in the first and drops in the second iteration. For PBE+OCA, the value of U barely changes after the third iteration, and convergence seems to nearly reached. This is not the case for LDA+OCA and PBE*+OCA. For the former, U seems to slightly decrease, shows small oscillations and does not behave consistently over different iterations. For the latter, U seems to oscillate around the converged value of PBE+OCA, but more iterations would be necessary to make a definitive statement. The relative order of different direct elements of U is maintained for all functionals during all iterations. The charge-U self-consistency cycle yields U parameters ranging from 8.54 to 8.88 eV for LDA+OCA, 8.95 to 9.28 eV for PBE+OCA and 8.96 to 9.29 eV for PBE*+OCA in the final iteration, although

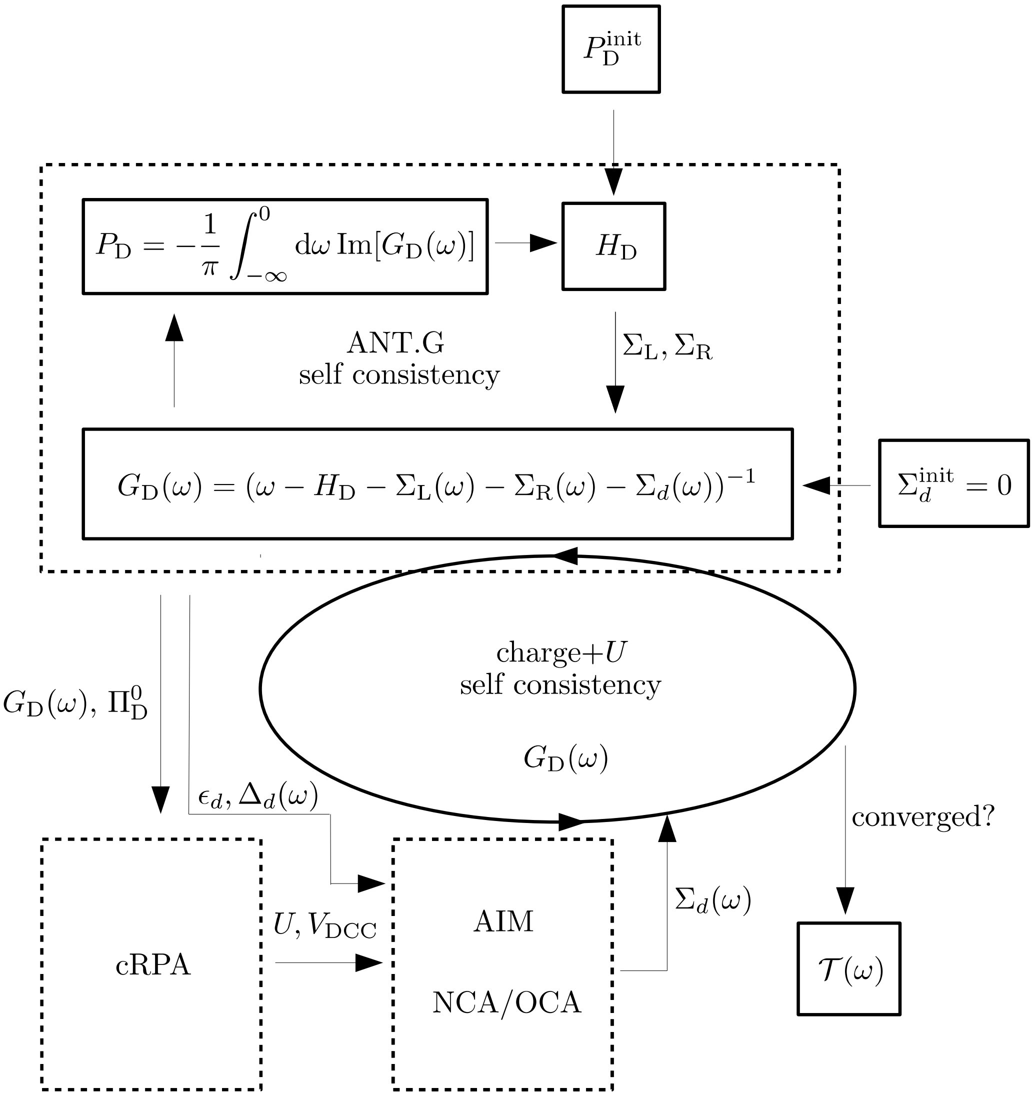

Figure 40: Computational scheme of the charge self-consistency cycle to determine the correlated transmission for the complete d shell. First, the non-interacting GF $G_D^0(\omega)$ is determined self-consistently, employing the ANT.G code. The Coulomb interaction within the d shell is computed by cRPA, using the non-interacting GF G_{D}^0 as starting point, and the fully-interacting GF $G_{\mathrm{D}}(\omega)$ in later cycles. An AIM is defined by the energy of the d level and the hybridization function $\Delta_d(\omega)$, the Coulomb interaction U and double counting correction V_{DCC}. The AIM is solved within the OCA, and the correlated self energy $\Sigma_d(\omega)$ is determined. The correlated GF $G_{\mathrm{D}}(\omega)$ and an updated density matrix are determined by the ANT.G self consistency, and new AIM parameters are extracted. When convergence of the charge+U self consistency cycle is reached, the correlated transmission $\mathcal{T}(\omega)$ can be calculated.

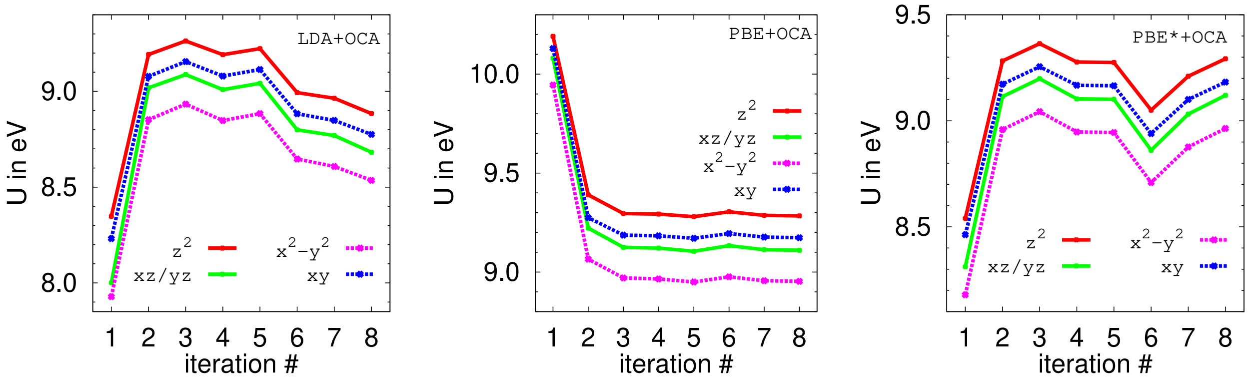

Figure 41: Direct on-site elements of the interaction U for different number of iterations of the charge-U self-consistency cycle. The zeroth order is omitted for better visibility and can be found in Tab. 3.

convergence is not fully reached for LDA+OCA and PBE*+OCA. This is the same order of magnitude as the U values obtained in Sec. 4.2 for HSE and scDFT+U. Convergence seems to be generally more problematic than for the charge self-consistency cycle, particularly if the initial U of the zeroth iteration is very different from the resulting U. The DFT functional only has a small influence on U, where the LDA seems to lead to slightly lower value of U than the PBE functional. The problems associated with cRPA calculations based on the LDA (see Sec. 4.4) do not appear here and are corrected by the addition of the correlated self energy.

The choice of double-counting correction is slightly less problematic here: while for one-shot DFT+OCA the choice of DCC was essential to correctly identify the spin-carrying orbitals (see Sec. 5.1.1), both the standard FLL DCC (see Eq. 74) and the orbital-dependent FLL DCC (see Eq. 75) localize the spin in the z^2 and xy orbitals. This is probably due to the smaller spread of different elements of U, so the orbital-dependence plays a smaller role. The standard FLL DCC will be used throughout this section.The choice of DCC still has a strong influence on the exact occupations and other resulting system properties. This will be discussed in more detail in Sec. 5.3.2.

Fig. 42 presents ϵ_d, occupations n_d of the OCA and the DFT steps and the imaginary part of the hybridization function at the Fermi level $-\mathrm{Im}\Delta(\epsilon_\mathrm{F})$ for different iterations of the charge-U self-consistency cycle. An initial drop in ϵ_d is observed for the first 5 iterations of the charge-U self-consistency. The peak in ϵ_d which was observed in the second iteration of the charge self-consistency cycle (see Fig. 35) is absent here. While ϵ_d seems to converge for PBE+OCA, an increase can be observed in the sixth iteration of LDA+OCA and PBE*+OCA. For the latter, the value of ϵ_d seems to be oscillating, similarly to the oscillations in U, where an decrease in U is associated with an increase in ϵ_d.

The OCA occupation of z^2 and xy initially drops for all functionals and remains nearly constant at 1.02 for all iterations, and only minor oscillations occur. For xz/yz and x^2-y^2, it initially increases for LDA+OCA and PBE*+OCA, and initially decreases for PBE+OCA. The DFT

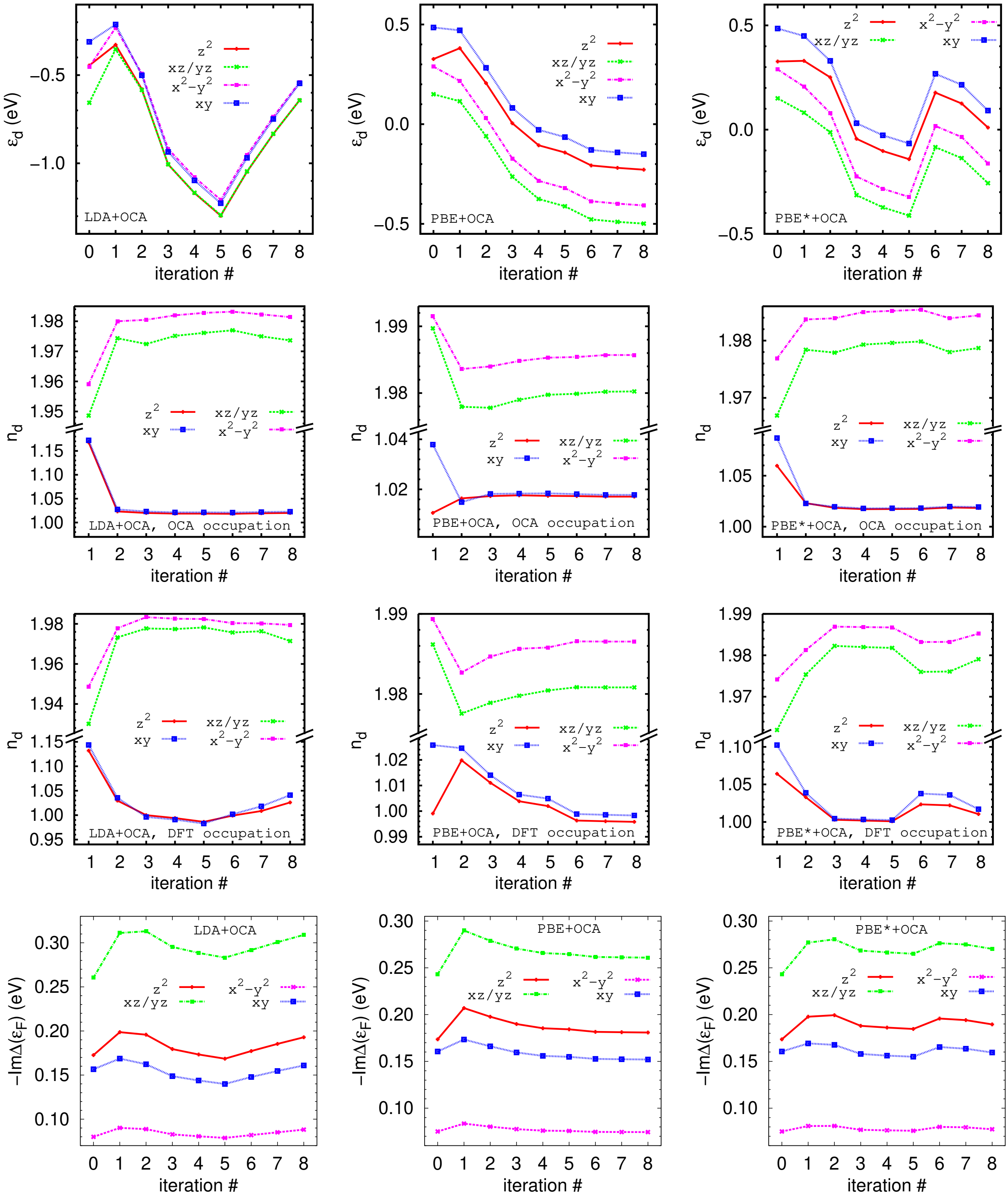

Figure 42: d level positions, OCA occupations, DFT occupations and the imaginary part of the hybridization function at the Fermi level for different iterations of the charge-U self-consistency cycle.

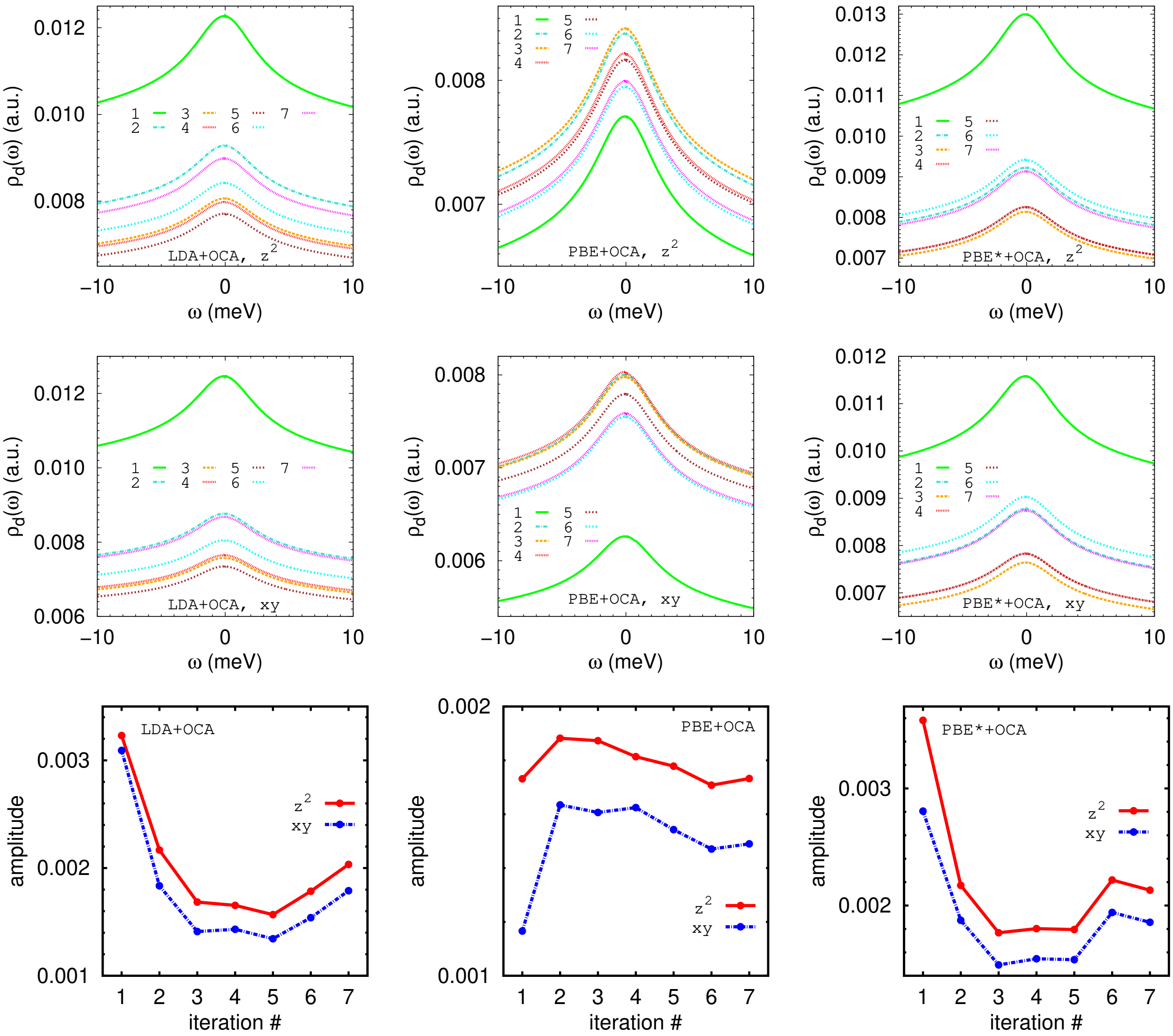

Figure 43: Impurity spectral function for z^2 and xy for a different number of iterations of the charge-U self consistency cycle (the zeroth order results can be found in Fig. 31 and Fig. 33), and the amplitude of the Kondo peak fitted according to Eq. 92.

occupation of z^2 and xy is also close to half-filling, and some oscillations similar to those in ϵ_d occur. It is not yet clear if the OCA and DFT occupations converge to the same value, since convergence is not fully reached. The DFT occupation of the xz/yz and x^2-y^2 orbitals show the same trends as in the OCA step, and have comparable occupations.

The imaginary part of the hybridization function initially increases and subsequently drops in the first iterations for all functionals and orbitals. For LDA+OCA and PBE*+OCA, an increase in the 6th iteration is observed. The hybridization follows the same trends as ϵ_d for all functionals, although changes in the hybridization seem smoother and are slightly less pronounced. This was also observed for the charge self-consistency cycle.

Fig. 43 shows impurity spectral functions for the z^2 and xy orbitals. Other orbitals do not carry a Kondo peak and are not shown. Frota fits according to Eq. 92 were performed in order to compare the Kondo peaks quantitatively. The amplitude of the Frota line shape is plotted in the bottom panels of Fig. 43.

For LDA+OCA and PBE*+OCA, the amplitude of the Kondo peak strongly decreases in the first two iterations, while it increases for PBE+OCA. In further iterations, it does not behave consistently and oscillations are visible. Changes in the amplitude can be explained by changes in the hybridization and in U. For LDA+OCA and PBE*+OCA, the amplitude is inversely proportional to U, and maxima of U can be associated with minima in the amplitude. This is particularly relevant when going from the zeroth to the first order: here, U increases considerably, whereas the size of the Kondo peak diminishes. For PBE+OCA, however, U is nearly constant after the third iteration. Here, the slight decay in amplitude is likely due to the changes in the hybridization. The amplitudes of the Kondo peaks are of the same order of magnitude for all methods after several iterations. This shows that the underlying DFT functional only plays a minor role.

Overall, changes in U and in the hybridization are responsible for changes in the size of the Kondo feature. Note that charge fluctuations seem to play a minor role after the second iteration for all functionals, since the OCA occupation is nearly constant. Kondo peaks are very small for all functionals and far away from the unitary limit. This can be attributed to the very high values of U which result from the charge-U self-consistency.

Fig. 44 presents transmission functions for different iterations of the charge-U self-consistency cycle. In order to compare the transmission functions quantitatively, Fano-Frota fits according to Eq. 93 were performed, by adding a linear and quadratic term to account for the transmission background, in order to determine the transmission amplitudes, q parameters and half-width parameters Γ, as shown in Fig. 44.

The amplitude of the transmission features follows exactly the same trend as the amplitude of the Kondo peak in the z^2 and the xy orbital (see Fig. 43, and note that the nth iteration of the transmission is based on the (n-1)th iteration of the spectral function, so features appearing in the spectral function appear in the subsequent iteration of the transmission). Due to symmetry, the transmission feature is still very likely resulting from the Kondo peak in the z^2 orbital.

For LDA+OCA and PBE*+OCA, a strong drop of q is observed in the second iteration. This can be attributed to the significantly smaller Kondo peak due to an increase of U and decrease of charge fluctuations, so that less direct tunneling through the Kondo peak can occur (see Sec. 3.5). For PBE+OCA, q remains nearly constant. Changes of q after the second iteration are small, and the resulting q values lie closely to each other, although convergence is not reached for LDA+OCA and PBE*+OCA.

The half-width parameter Γ behaves inversely proportional to the amplitude of the Kondo peak. This was also observed and discussed in the charge self-consistency cycle (see Sec. 5.2.2), and is due to the temperature broadening of the Kondo peak.

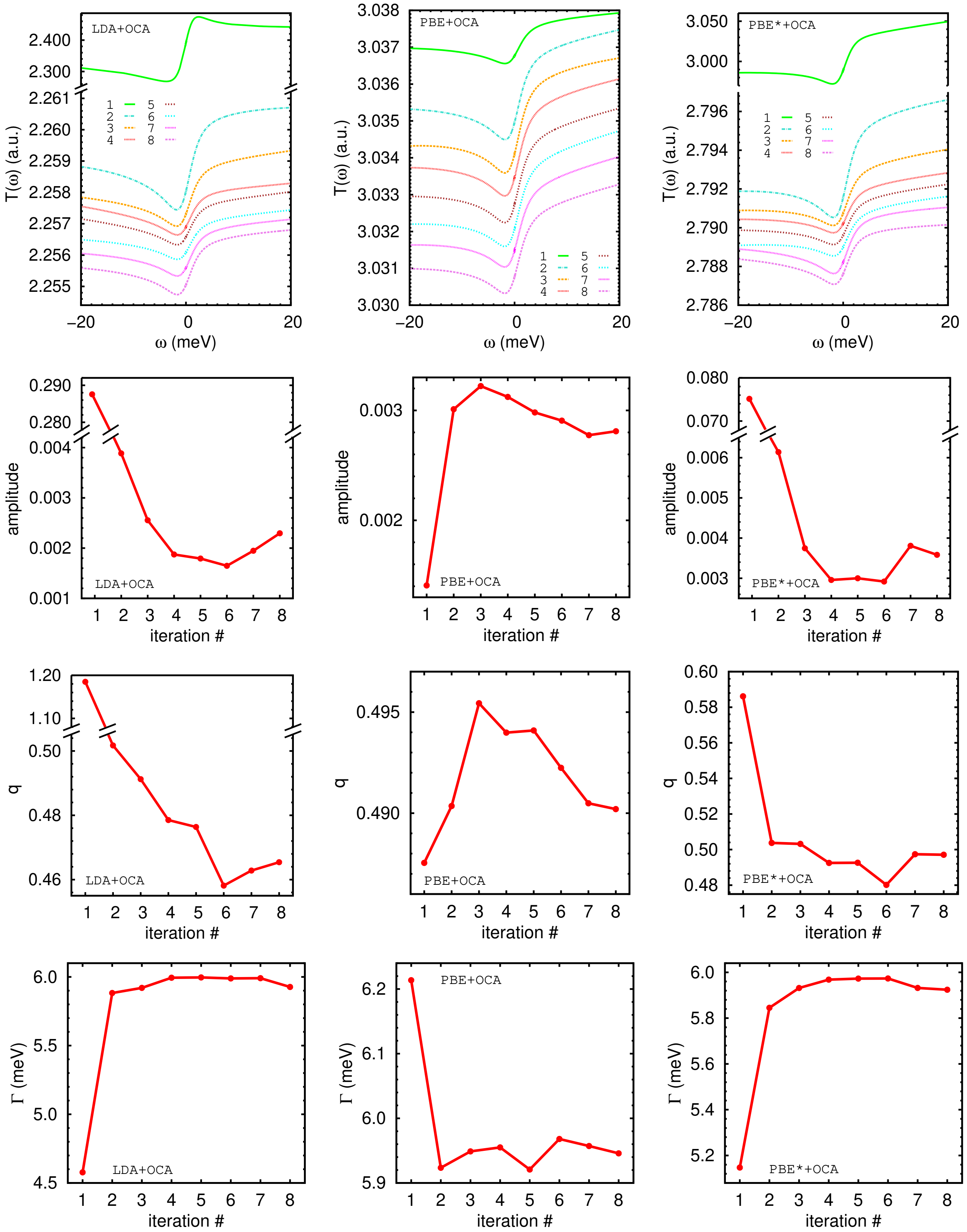

Figure 44: Transmission functions for a different number of iterations of the charge-U self-consistency cycle. Transmission functions have been offset, and linear and quadratic background terms have been subtracted for better visibility. Transmission amplitude, q factor and half-width $\Gamma = 2.54\Gamma_\mathrm{F}$ were obtained by Frota fits according to Eq. 93.

5.3.2 Discussion

The charge-U self-consistency cycle leads to considerable changes in the interaction U, and to changes in the electronic structure similar, but not identical, to those observed in the charge self-consistency cycle of Sec. 5.2. The resulting U parameters are relatively high, and similar to those obtained in Sec. 4.2 for functionals with higher-level correlation. If the initial U of the zeroth iteration is very low, the observed increase in U might be a self-enhancing: a higher value of U pushes the Hubbard band of the respective d levels further away from the Fermi level and leads to smaller Kondo peaks, which reduces screening in the following iteration leading to even higher values of U. A constant increase of U is only observed in the first 3 iterations for LDA+OCA and PBE*+OCA, whereas beyond that, other effects of self-consistency become more important.

The resulting U parameters are much less spread out than those obtained based on the LDA and PBE functionals. This also reduces the differences between different double-counting schemes. While the correct choice of double-counting correction was of crucial importance to find the spin-carrying orbitals for one-shot LDA+OCA and PBE+OCA, both the orbital-dependent and standard FLL DCCs yield a spin-1 state for all methods studied, where the spin is localized in the z^2 and xy orbitals. The choice of DCC is nevertheless important, since it can strongly influence the orbital occupation and, therefore, affect the size and shape of the Kondo peak[70]. To make a conclusive statement about the quantitative differences between different DCCs, a full self-consistent calculation would be necessary for the orbital-dependent FLL DCC, which would pose a significant computational effort. Test OCA calculations employing the orbital-dependent FLL DCC based on the second and seventh iteration of the charge-U self-consistency cycle show that the difference in occupation between the two DCCs is small, potentially owing to the large values of U. The difference between different DCCs is expected to be larger if occupations are further away from particle-hole symmetry.

The high values of U in conjunction with the very small charge fluctuations lead to small Kondo peaks and small transmission features, which are all dip-like, since direct tunneling through the Kondo peak is not very probable.

Convergence of the charge-U self-consistency seems to be much slower than that of the charge self-consistency cycle, particularly if the initial U is very different from its final value. While PBE+OCA converges very quickly, several quantities show oscillations for LDA+OCA and PBE*+OCA, and more iterations would be necessary to see if convergence will eventually be reached. This is problematic due to the very high computational effort, particularly because an AIM has to be solved in each calculation step. Convergence could be accelerated by the introduction of mixing (also see Ref. [240] regarding mixing in the context of self-consistent DFT+DMFT). Its simplest form, linear mixing, usually assures convergence but is typically slow and would also require many calculation steps. More sophisticated mixing schemes exist and are already commonly used to accelerate convergence of many types of electronic structure calculations. The implementation of such a mixing scheme could be a possible way to assure convergence of the charge-U self-consistency cycle without considerably increasing the computational effort.

6 Conclusion and outlook

This thesis studied several aspects of strong electronic correlations in a scanning tunneling spectroscopy setup. To this end, the Co@Cu(001) and Co@Cu(111) adatom systems probed by an STM tip were investigated by a combination of DFT, Green's function based electron transport, the OCA impurity solver and the cRPA.

The first focus of this thesis was to establish a connection between the symmetry of the d orbital carrying a Kondo peak and the resulting Fano-Frota line shape in the transmission feature. For this purpose, individual d orbitals were correlated and the resulting transmission functions calculated. It was found that the line shape strongly depends on which orbital bears the Kondo effect. The transmission resulting from a Kondo peak in the z^2 orbital best reproduces the experimental STS results for Co@Cu(001), while for Co@Cu(111), none of the computed line shapes are in accordance with the experimentally observed dip. This was attributed to the Co@Cu(111) surface state, which plays a deciding role and is not appropriately captured by the finite-cluster calculation used in this thesis. The interference mechanism leading to the Fano-Frota transmission features was explained by a simplified model, taking into account the interaction between one conduction electron level and the correlated d level of the Co atom. The model can correctly describe the calculated line shapes for both systems, with one notable exception, and might make it possible to approximately predict line shapes based on a DFT calculation alone. The temperature dependence of the transmission feature was also studied. It was observed that a smaller Kondo peak due to increasing temperature leads to more dip-like line shapes for all d orbitals. This can be explained by the aforementioned simplified model. The smaller spectral weight of the Kondo peak allows for less direct tunneling through the d level, so that indirect interference effects are more relevant, which overall changes the line shapes towards a dip. It was found that the z^2 orbital is most relevant in a transport situation due to symmetry alone, interacting most strongly with the z^2 and p_z orbitals of the STM tip. The xz/yz orbitals might also be relevant for the transport properties, particularly if the STM tip is not placed exactly on top of the adatom, while the x^2-y^2 and xy orbitals lie in the x-y plane and interact only weakly with the STM tip.

The computation of the partially screened Coulomb interaction U was the second central focus of this work, and the computed U parameters served as input parameters for the AIM defined and solved in the last chapter. The cRPA methodology was introduced and applied for the Co@Cu(001) and Co@Cu(111) systems for different KS-DFT and GKS-DFT functionals and different sizes of the polarization region. The choice of functional plays a strong role on the resulting U. Higher-level correlation like in the HSE functional and in self-consistent DFT+U leads to overall higher and less spread-out U values. The half-filled orbitals are associated with higher direct on-site elements of U than the filled orbitals. The size of the polarization region also has a sizable effect on the resulting U. For PBE and HSE, a drop of U is observed when the polarization region is enlarged, while for LSDA, the opposite is the case: U grows to unphysical values when the polarization region is enlarged. This might be due to the fact that LSDA does not capture the correct spin state of the d shell, and the combination of LSDA and cRPA seems overall problematic for the investigated system. Two simplified models to approximately incorporate polarization effects from outside of the polarization region were proposed. While pre-screening to first order yielded unphysical results, the pre-screening of the direct elements of the Coulomb interaction might be a promising approach to approximately include polarization effects for large systems.

The third and final focus was to achieve an ab-initio description for the Co@Cu(001) system by performing DFT+OCA calculations with different levels of self-consistency, and obtain the signature of the Kondo peak in the transmission function. One-shot DFT+OCA is already capable of producing Kondo peaks and Fano-Frota transmission features, and particularly one-shot LDA+OCA yields Kondo peaks in good agreement with experimental conductance curves. The correct choice of DCC proved to be crucial to find the spin-carrying orbitals. The introduction of charge self-consistency has a considerable effect on the electronic structure of the system. It pushes the d levels to lower energies, reduces charge fluctuations and affects the hybridization function. It does, however, not improve the agreement with experimental conductances. The high value of U and significantly smaller charge fluctuations compared to one-shot DFT+OCA result in small Kondo peaks and dip-like line shapes in the transmission for all functionals. This is not an intrinsic problem of the charge self-consistency, however, and should be remedied by an improved way of determining the interaction U. Lastly, the computation of U was included in the charge-U self-consistency cycle. It results in an overall increase of U, and less anisotropy in its direct elements, similar to results obtained for the HSE functional and self-consistent DFT+U. It also affects the electronic structure similarly to the charge self-consistency cycle, although convergence is more problematic and oscillations occur. The introduction of a mixing scheme might alleviate the slow convergence. While the correct choice of DCC is crucial for one-shot DFT+OCA, it becomes less important when the computation of U is included in the self-consistency cycle due to the smaller anisotropy in U, and both DCCs yield very similar spin states.

The double-counting problem nevertheless remains one of the biggest issues of DFT+OCA and, more generally, DFT+DMFT. An exact expression for the DCC cannot be found, because the most commonly used DFT functionals cannot be represented within standard many-body diagrams[240]. This could only be overcome if the weakly correlated part of the system were described by an (approximate) many-body method like GW or its static approximation COHSEX, although a method like GW+DMFT comes at a very high computational cost.

A Complex and real Fano line shapes

Here we derive the real Fano line shape given by Eq. (91) from its complex representation in Eq. (90):

$$\rho_{\mathrm{FL}}(\omega) = \mathrm{Im}\left[e^{\mathrm{i}\phi_q}\left(\frac{A}{\omega-\omega_0+\mathrm{i}\Gamma}\right)\right] \tag{120}$$

Introducing the abbreviation $\epsilon = (\omega-\omega_0)/\Gamma$, we have

$$\begin{aligned}\rho_{\mathrm{FL}} &= \frac{A}{\Gamma}\cdot\mathrm{Im}\left[(\cos(\phi_q)+\mathrm{i}\sin(\phi_q))\,\frac{\epsilon-\mathrm{i}}{\epsilon^2+1}\right]\\ &= \frac{A}{\Gamma}\left[\frac{-\cos(\phi_q)+\epsilon\sin(\phi_q)}{\epsilon^2+1}\right]\\ &= \frac{A}{\Gamma}\left[\frac{-\cos^2(\frac{\phi_q}{2})+\sin^2(\frac{\phi_q}{2})+2\epsilon\sin(\frac{\phi_q}{2})\cos(\frac{\phi_q}{2})}{\epsilon^2+1}\right]\\ &= \frac{A}{\Gamma}\left[\frac{-1+\tan^2(\frac{\phi_q}{2})+2\epsilon\tan(\frac{\phi_q}{2})}{\epsilon^2+1}\right]\cos^2\left(\frac{\phi_q}{2}\right).\end{aligned} \tag{121}$$

Defining $q \equiv \tan(\phi_q/2)$, we arrive at

$$\rho_{\mathrm{FL}} = \frac{A}{\Gamma}\left[\frac{(q+\epsilon)^2}{\epsilon^2+1}-1\right]\frac{1}{1+q^2}, \tag{122}$$

which is the same as Eq. (91).

B Non-Orthogonal basis sets

This work makes use of non-orthogonal (Gaussian) basis sets. While the use of a Gaussian basis makes the solution of certain integrals when solving the KS equations very simple, it comes at the price of non-orthogonality. Working with a non-orthogonal basis becomes particularly tricky when projections on subspaces are involved. This is the case in this work: Different parts of the system are treated on different levels of approximation, and projections on subspaces are necessary in various situations. It was shown that the correct choice of projection is of crucial importance, and the wrong choice can lead to unphysical results[70;227;228].

This appendix gives a short introduction to non-orthogonal basis sets, and only final results are presented. More details and derivations can be found in the aforementioned literature. Following the notation of Ref. [70], let $\{|\alpha\rangle\}$ be a set of non-orthogonal orbitals spanning a Hilbert space H. The overlap matrix is defined as

$$S_{\alpha\beta} = \langle\alpha|\beta\rangle. \tag{123}$$

The projection operator to a subspace $\hat{P}_{\mathrm{M}}$ in a non-orthogonal basis is

$$\hat{P}_{\mathrm{M}} = \sum_{m,n\in\mathrm{M}} |m\rangle(S_{\mathrm{M}}^{-1})_{mn}\langle n|. \tag{124}$$

An operator $\hat{A}$ projected onto subspace M becomes:

$$\hat{A}_{\mathrm{M}} = \sum_{m,n\in\mathrm{M}} |m\rangle(\mathbf{S}_{\mathrm{M}}^{-1}\mathbf{A}_{\mathrm{M}}\mathbf{S}_{\mathrm{M}}^{-1})_{mn}\langle n| = \sum_{m,n\in\mathrm{M}} |m\rangle(\tilde{\mathbf{A}}_{\mathrm{M}})_{mn}\langle n|, \tag{125}$$

where the nuclear matrix $\tilde{\mathbf{A}}_{\mathrm{M}}$ was defined as $\tilde{\mathbf{A}}_{\mathrm{M}} = \mathbf{S}_{\mathrm{M}}^{-1}\mathbf{A}_{\mathrm{M}}\mathbf{S}_{\mathrm{M}}^{-1}$. When projecting an operator $\hat{A}_{\mathrm{M}}$ from a subspace M to a smaller subspace $\mathrm{M}' \subset \mathrm{M}$, the projection becomes:

$$\hat{A}_{\mathrm{M}'} = \sum_{m',n'\in\mathrm{M}'} |m'\rangle(\mathbf{S}_{\mathrm{M}'}^{-1}\mathbf{S}_{\mathrm{M}'\mathrm{M}}\tilde{\mathbf{A}}_{\mathrm{M}}\mathbf{S}_{\mathrm{M}\mathrm{M}'}\mathbf{S}_{\mathrm{M}'}^{-1})_{mn}\langle n'| = \sum_{m',n'\in\mathrm{M}'} |m'\rangle(\tilde{\mathbf{A}}_{\mathrm{M}'})_{mn}\langle n'|, \tag{126}$$

where $\tilde{\mathbf{A}}_{\mathrm{M}'} = \mathbf{S}_{\mathrm{M}'}^{-1}\mathbf{S}_{\mathrm{M}'\mathrm{M}}\tilde{\mathbf{A}}_{\mathrm{M}}\mathbf{S}_{\mathrm{M}\mathrm{M}'}\mathbf{S}_{\mathrm{M}'}^{-1}$ is the nuclear matrix in subspace M′. This is the only physically reasonable projection[227].

The defining equation for the GF in a non-orthogonal basis is:

$$(E\boldsymbol{S} - \boldsymbol{H})\,\boldsymbol{S}^{-1}\boldsymbol{G}(E) = \boldsymbol{S}. \tag{127}$$

It is convenient to work with the nuclear matrix of the GF $\tilde{\boldsymbol{G}}(E) := \boldsymbol{S}^{-1}\boldsymbol{G}(E)\boldsymbol{S}^{-1}$, which is defined by the simpler equation:

$$(E\boldsymbol{S} - \boldsymbol{H})\,\tilde{\boldsymbol{G}}(E) = \mathbf{1}. \tag{128}$$

The Coulomb interaction in an non-orthogonal basis becomes[119]:

$$V^{e-e} = \frac{1}{2} \sum_{\alpha,\alpha',\beta,\beta',\sigma,\sigma'} \tilde{V}_{\alpha\beta,\alpha'\beta'}\, c^{\dagger}_{\alpha\sigma}c^{\dagger}_{\alpha'\sigma'}c_{\beta'\sigma'}c_{\beta\sigma}, \tag{129}$$

where $\tilde{V}_{\alpha\beta,\alpha'\beta'}$ is the nuclear matrix of Coulomb interaction $V_{\alpha\beta;\alpha'\beta'}$, which is given by:

$$V_{\alpha\beta;\alpha'\beta'} = e^2 \int d^3r_1 \int d^3r_2 \frac{\phi^*_{\alpha}(\vec{r}_1\phi_{\beta}(\vec{r}_1)\phi^*_{\alpha'}(\vec{r}_2)\phi_{\beta'}(\vec{r}_2)}{||\vec{r}_1 - \vec{r}_2||}. \tag{130}$$

C Analytical continuation of the OCA self energy to the Matsubara axis

This appendix presents the correlated self energy on the real axis $\Sigma_d(\omega)$ (Fig. 45), as output by the OCA, and after the analytical continuation to the Matsubara axis $\Sigma_d(\mathrm{i}\omega)$ (Fig. 46), for the z^2 orbital, LDA+OCA and PBE+OCA, respectively, and the tenth iteration of the charge self-consistency cycle (see Sec. 5.2.1). Unphysical artifacts appear close to the energy boundaries for both the real and the imaginary part of the self energy on the real axis. This is very likely an edge effect, and more pronounced for LDA+OCA than for PBE+OCA. This complicates the fit of the flanks of the self energy, which is required for the analytical continuation. The energy range for the flank fit has therefore to be chosen by hand.

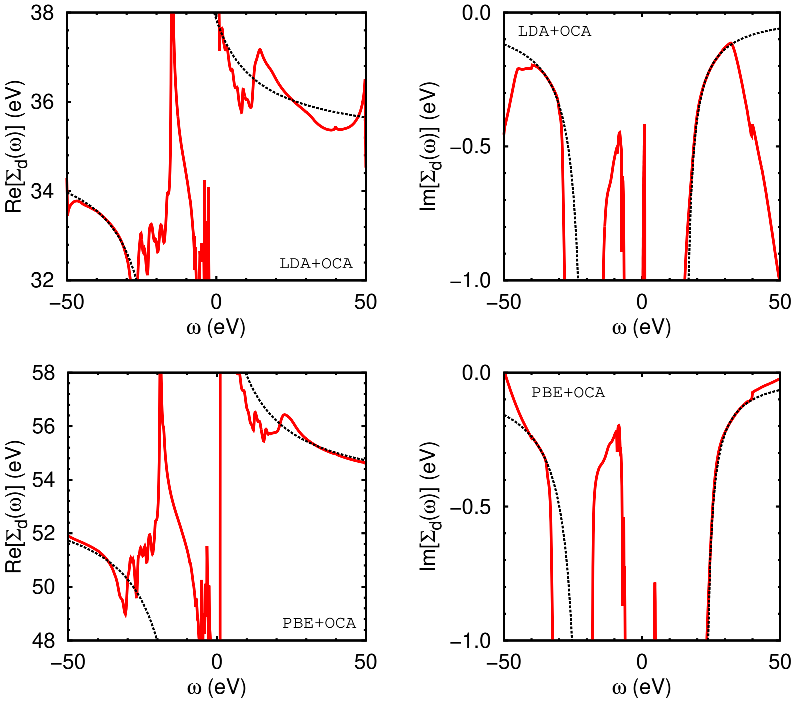

Figure 45: Real and imaginary part of the correlated self energy $\Sigma_d(\omega)$ on the real axis obtained from an OCA calculation (red continuous line), for the z^2 orbital and the tenth iteration of the charge self-consistency cycle for LDA+OCA and PBE+OCA. The flank fits (black dashed line) for the analytical continuation are also shown.

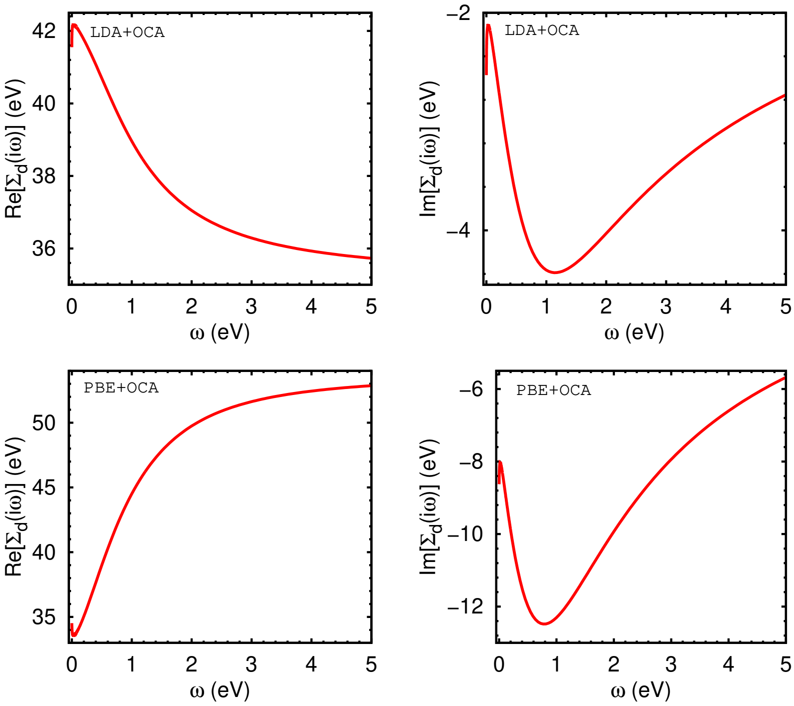

Figure 46: Real and imaginary part of the correlated self energy $\Sigma_d(\mathrm{i}\omega)$ on the Matsubara axis obtained by analytical continuation of $\Sigma_d(\omega)$, for the z^2 orbital and the tenth iteration of the charge self-consistency cycle for LDA+OCA and PBE+OCA.

References

[1] G. Moore. Cramming more components onto integrated circuits. *Electronics*, 38:114, 1965.

[2] R. L. Carroll and C. B. Gorman. The genesis of molecular electronics. *Angew. Chem. Int. Ed.*, 41:4378, 2002.

[3] J. C. Cuevas and E. Scheer. *Molecular Electronics.* WORLD SCIENTIFIC, 2nd edition, 2017.

[4] D. Goldhaber-Gordon, M. Montemerlo, J. Love, G. Opiteck, and J. Ellenbogen. Overview of nanoelectronic devices. *Proc. IEEE*, 85:521, 1997.

[5] C. Joachim, J. Gimzewski, and A. Aviram. Electronics using hybrid-molecularand mono-molecular devices. *Nature*, 408:541, 2000.

[6] X. Wang, Q. Li, J. Xie, Z. Jin, J. Wang, Y. Li, K. Jiang, and S. Fan. Fabrication of ultralong and electrically uniform single-walled carbon nanotubes on clean substrates. *Nano Lett.*, 9(9):3137, 2009.

[7] S. Kobatake, T. Yamada, K. Uchida, N. Kato, and M. Irie. Photochromism of 1,2-bis(2,5-dimethyl-3-thienyl)perfluoro- cyclopentene in a single crystalline phase. *JACS*, 121(11):2380, 1999.

[8] S. van der Molen, J. Liao, T. Kudernac, J. Agustsson, L. Bernard, M. Calame, B. van Wees, B. Feringa, and C. Schönberger. Light-controlled conductance switching of ordered metal-molecule-metal devices. *Nano Lett.*, 9:76, 2009.

[9] S. J. Tans, A. R. M. Verschueren, and C. Dekker. Room-temperature transistor based on a single carbon nanotube. *Nature*, 393:49, 1998.

[10] H. Song, Y. Kim, Y. H. Jang, H. Jeong, M. A. Reed, and T. Lee. Observation of molecular orbital gating. *Nature*, 462:1039, 2009.

[11] M. Elbing, R. Ochs, M. Koentopp, M. Fischer, C. von Hänisch, F. Weigend, F. Evers, H. B. Weber, and M. Mayor. A single-molecule diode. *Proc. Natl. Acad. Sci.*, 102(25):8815, 2005.

[12] I. Díez-Pérez, J. Hihath, Y. Lee, L. Yu, L. Adamska, M. A. Kozhushner, I. I. Oleynik, and N. Tao. Rectification and stability of a single molecular diode with controlled orientation. *Nature Chemistry*, 1:635, 2009.

[13] A. Batra, P. Darancet, Q. Chen, J. S. Meisner, J. R. Widawsky, J. B. Neaton, C. Nuckolls, and L. Venkataraman. Tuning rectification in single-molecular diodes. *Nano Lett.*, 13(12):6233, 2013.

[14] D. Gatteschi, R. Sessoli, and J. Villain. *Molecular Nanomagnets*. Oxford University Press, 2006.

[15] W. Liang, M. Bockrath, D. Bozovic, J. H. Hafner, M. Tinkham, and H. Park. Fabry - perot interference in a nanotube electron waveguide. *Nature*, 411:665, 2001.

[16] J. Kong, E. Yenilmez, T. W. Tombler, W. Kim, H. Dai, R. B. Laughlin, L. Liu, C. S. Jayanthi, and S. Y. Wu. Quantum interference and ballistic transmission in nanotube electron waveguides. *Phys. Rev. Lett.*, 87:106801, 2001.

[17] C. M. Guédon, H. Valkenier, T. Markussen, K. S. Thygesen, J. C. Hummelen, and S. J. van der Molen. Observation of quantum interference in molecular charge transport. *Nat. Nanotechnol.*, 7:305, 2012.

[18] B. J. van Wees, H. van Houten, C. W. J. Beenakker, J. G. Williamson, L. P. Kouwenhoven, D. van der Marel, and C. T. Foxon. Quantized conductance of point contacts in a two-dimensional electron gas. *Phys. Rev. Lett.*, 60:848, 1988.

[19] N. Agraït, A. L. Yeyati, and J. M. van Ruitenbeek. Quantum properties of atomic-sized conductors. *Phys. Rep.*, 377(2):81, 2003.

[20] I. Žutić, J. Fabian, and S. Das Sarma. Spintronics: Fundamentals and applications. *Rev. Mod. Phys.*, 76:323, 2004.

[21] S. S. P. Parkin, K. P. Roche, M. G. Samant, P. M. Rice, R. B. Beyers, R. E. Scheuerlein, E. J. O'Sullivan, S. L. Brown, J. Bucchigano, D. W. Abraham, Y. Lu, M. Rooks, P. L. Trouilloud, R. A. Wanner, and W. J. Gallagher. Exchange-biased magnetic tunnel junctions and application to nonvolatile magnetic random access memory (invited). *J. Appl. Phys.*, 85(8):5828, 1999.

[22] J.-F. Tremblay. Riding on flat panels. *Chemical & Engineering News Archive*, 84(26):13, 2006.

[23] J. J. Palacios, P. Tarakeshwar, and D. M. Kim. Metal contacts in carbon nanotube field-effect transistors: Beyond the schottky barrier paradigm. *Phys. Rev. B*, 77:113403, 2008.

[24] C. P. Collier, E. W. Wong, M. Belohradský, F. M. Raymo, J. F. Stoddart, P. J. Kuekes, R. S. Williams, and J. R. Heath. Electronically configurable molecular-based logic gates. *Science*, 285(5426):391, 1999.

[25] V. Percec, M. Glodde, T. K. Bera, Y. Miura, I. Shiyanovskaya, K. D. Singer, V. S. K. Balagurusamy, P. A. Heiney, I. Schnell, A. Rapp, H.-W. Spiess, S. D. Hudson, and H. Duan. Self-organization of supramolecular helical dendrimers into complex electronic materials. *Nature*, 419:384, 2002.

[26] G. Binnig, H. Rohrer, C. Gerber, and E. Weibel. Surface studies by scanning tunneling microscopy. *Phys. Rev. Lett.*, 49:57, 1982.

[27] N. M. A. 2019. Press release nobel prize in physics, 1986. Retrieved Mon. 11 Feb 2019.

[28] K. Oura, V. Lifshits, A. Saranin, A. Zotov, and M. Katayama. *Surface Science: An Introduction.* Advanced Texts in Physics. Springer Berlin Heidelberg, 2003.

[29] J. Li, W.-D. Schneider, R. Berndt, and B. Delley. Kondo scattering observed at a single magnetic impurity. *Phys. Rev. Lett.*, 80:2893, 1998.

[30] V. Madhavan, W. Chen, T. Jamneala, M. F. Crommie, and N. S. Wingreen. Tunneling into a single magnetic atom: Spectroscopic evidence of the Kondo resonance. *Science*, 280(5363):567, 1998.

[31] H. C. Manoharan, C. P. Lutz, and D. M. Eigler. Quantum mirages formed by coherent projection of electronic structure. *Nature*, 403(6769):512, 2000.

[32] N. Knorr, M. A. Schneider, L. Diekhöner, P. Wahl, and K. Kern. Kondo effect of single co adatoms on cu surfaces. *Phys. Rev. Lett.*, 88:096804, 2002.

[33] K. Nagaoka, T. Jamneala, M. Grobis, and M. F. Crommie. Temperature dependence of a single Kondo impurity. *Phys. Rev. Lett.*, 88:077205, 2002.

[34] A. J. Heinrich, J. A. Gupta, C. P. Lutz, and D. M. Eigler. Single-atom spin-flip spectroscopy. *Science*, 306(5695):466, 2004.

[35] A. Zhao, Q. Li, L. Chen, H. Xiang, W. Wang, S. Pan, B. Wang, X. Xiao, J. Yang, J. G. Hou, and Q. Zhu. Controlling the Kondo effect of an adsorbed magnetic ion through its chemical bonding. *Science*, 309(5740):1542, 2005.

[36] M. F. Crommie. Manipulating magnetism in a single molecule. *Science*, 309(5740):1501, 2005.

[37] V. Iancu, A. Deshpande, and S.-W. Hla. Manipulation of the Kondo effect via two-dimensional molecular assembly. *Phys. Rev. Lett.*, 97:266603, 2006.

[38] N. Néel, J. Kröger, L. Limot, K. Palotas, W. A. Hofer, and R. Berndt. Conductance and Kondo effect in a controlled single-atom contact. *Phys. Rev. Lett.*, 98:016801, 2007.

[39] W. de Haas, J. de Boer, and G. van dën Berg. The electrical resistance of gold, copper and lead at low temperatures. *Physica*, 1(7–12):1115, 1934.

[40] M. P. Sarachik, E. Corenzwit, and L. D. Longinotti. Resistivity of mo-nb and mo-re alloys containing 1 *Phys. Rev.*, 135:A1041, 1964.

[41] J. Kondo. Resistance minimum in dilute magnetic alloys. *Progr. Theor. Phys.*, 32(1):37, 1964.

[42] I. Fernández-Torrente, K. J. Franke, and J. I. Pascual. Vibrational Kondo effect in pure organic charge-transfer assemblies. *Phys. Rev. Lett.*, 101:217203, 2008.

[43] K. Capelle and V. L. C. Jr. Density functionals and model hamiltonians: Pillars of many-particle physics. *Phys. Rep.*, 528(3):91, 2013.

[44] N. F. Mott and R. Peierls. Discussion of the paper by de boer and verwey. *Proc. Phys. Soc.*, 49(4S):72, 1937.

[45] N. F. Mott. The basis of the electron theory of metals, with special reference to the transition metals. *Proc. Phys. Soc. Sec. A*, 62(7):416, 1949.

[46] P. Coleman. Heavy Fermions: electrons at the edge of magnetism. *arXiv e-prints*, pages cond–mat/0612006, 2006.

[47] G. Kotliar and J. Liu. Superexchange mechanism and d-wave superconductivity. *Phys. Rev. B*, 38:5142, 1988.

[48] P. W. Anderson, P. A. Lee, M. Randeria, T. M. Rice, N. Trivedi, and F. C. Zhang. The physics behind high-temperature superconducting cuprates: the plain vanilla version of RVB. *J. Phys. Condens. Matter*, 16(24):R755, 2004.

[49] A. Garg, M. Randeria, and N. Trivedi. Strong correlations make high-temperature superconductors robust against disorder. *Nat. Phys.*, 4:762, 2008.

[50] A. Posazhennikova, B. Bayani, and P. Coleman. Conductance of a spin-1 quantum dot: The two-stage Kondo effect. *Phys. Rev. B*, 75:245329, 2007.

[51] N. Roch, S. Florens, V. Bouchiat, W. Wernsdorfer, and F. Balestro. Quantum phase transition in a single-molecule quantum dot. *Nature*, 453(7195):633, 2008.

[52] J. Nygard, D. H. Cobden, and P. E. Lindelof. Kondo physics in carbon nanotubes. *Nature*, 408(6810):342, 2000.

[53] P. Jarillo-Herrero, J. Kong, H. S. van der Zant, C. Dekker, L. P. Kouwenhoven, and S. De Franceschi. Orbital Kondo effect in carbon nanotubes. *Nature*, 434(7032):484, 2005.

[54] A. A. Houck, J. Labaziewicz, E. K. Chan, J. A. Folk, and I. L. Chuang. Kondo effect in electromigrated gold break junctions. *Nano Lett.*, 5(9):1685, 2005.

[55] W. Feng, Q. Liu, C. Zhou, X. Lai, B. Li, and A. Zhao. Preserved Kondo effect of small cobalt atomic chains on ru(0001) surface. *New J. Phys.*, 18(12):123011, 2016.

[56] V. Iancu, A. Deshpande, and S.-W. Hla. Manipulating Kondo temperature via single molecule switching. *Nano Lett.*, 6(4):820, 2006.

[57] A. F. Otte, M. Ternes, K. von Bergmann, S. Loth, H. Brune, C. P. Lutz, C. F. Hirjibehedin, and A. J. Heinrich. The role of magnetic anisotropy in the Kondo effect. *Nat Phys*, 4(11):847, 2008.

[58] V. Alexandrov, P. Coleman, and O. Erten. Kondo breakdown in topological Kondo insulators. *Phys. Rev. Lett.*, 114:177202, 2015.

[59] O. Erten, P. Ghaemi, and P. Coleman. Kondo breakdown and quantum oscillations in smb$_6$. *Phys. Rev. Lett.*, 116:046403, 2016.

[60] K. Hagiwara, Y. Ohtsubo, M. Matsunami, S.-i. Ideta, K. Tanaka, H. Miyazaki, J. E. Rault, P. L. Fèvre, F. Bertran, A. Taleb-Ibrahimi, R. Yukawa, M. Kobayashi, K. Horiba, H. Kumigashira, K. Sumida, T. Okuda, F. Iga, and S.-i. Kimura. Surface Kondo effect and non-trivial metallic state of the Kondo insulator ybb12. *Nat. Commun.*, 7:12690, 2016.

[61] S. Y. Savrasov and G. Kotliar. Spectral density functionals for electronic structure calculations. *Phys. Rev. B*, 69:245101, 2004.

[62] P. Wahl, L. Diekhöner, M. A. Schneider, L. Vitali, G. Wittich, and K. Kern. Kondo temperature of magnetic impurities at surfaces. *Phys. Rev. Lett.*, 93:176603, 2004.

[63] J. Merino and O. Gunnarsson. Simple model for scanning tunneling spectroscopy of noble metal surfaces with adsorbed Kondo impurities. *Phys. Rev. B*, 69:115404, 2004.

[64] J. Merino and O. Gunnarsson. Role of surface states in scanning tunneling spectroscopy of (111) metal surfaces with Kondo adsorbates. *Phys. Rev. Lett.*, 93:156601, 2004.

[65] L. Vitali, R. Ohmann, S. Stepanow, P. Gambardella, K. Tao, R. Huang, V. S. Stepanyuk, P. Bruno, and K. Kern. Kondo effect in single atom contacts: The importance of the atomic geometry. *Phys. Rev. Lett.*, 101:216802, 2008.

[66] N. Néel, J. Kröger, and R. Berndt. Kondo effect of a co atom on cu(111) in contact with an iron tip. *Phys. Rev. B*, 82:233401, 2010.

[67] D.-J. Choi, M. V. Rastei, P. Simon, and L. Limot. Conductance-driven change of the Kondo effect in a single cobalt atom. *Phys. Rev. Lett.*, 108:266803, 2012.

[68] C.-Y. Lin, A. H. Castro Neto, and B. A. Jones. First-principles calculation of the single impurity surface Kondo resonance. *Phys. Rev. Lett.*, 97:156102, 2006.

[69] P. P. Baruselli, R. Requist, A. Smogunov, M. Fabrizio, and E. Tosatti. Co adatoms on cu surfaces: Ballistic conductance and Kondo temperature. *Phys. Rev. B*, 92:045119, 2015.

[70] D. Jacob. Towards a full ab initio theory of strong electronic correlations in nanoscale devices. *J. Phys. Condens. Matter*, 27(24):245606, 2015.

[71] E. Schrödinger. Quantisierung als Eigenwertproblem. *Ann. Phys. (Leipzig)*, 79:361, 1926.

[72] M. Born and R. Oppenheimer. Zur Quantentheorie der Molekeln. *Ann. Phys. (Leipzig)*, 389(20):457, 1927.

[73] E. Fermi. Un Metodo Statistico per la Determinazione di alcune Prioprietà dell'Atomo. *Rend. Accad. Naz. Lincei*, 6:602, 1927.

[74] L. Thomas. The calculation of atomic fields. *Math. Proc. Cambridge Philos. Soc.*, 23:542, 1927.

[75] W. Kohn. Nobel lecture: Electronic structure of matter—wave functions and density functionals. *Rev. Mod. Phys.*, 71(5):1253, 1999.

[76] P. Hohenberg and W. Kohn. Inhomogeneous electron gas. *Phys. Rev.*, 136(3B):B864, 1964.

[77] M. Levy. Electron densities in search of hamiltonians. *Phys. Rev. A*, 26(3):1200, 1982.

[78] E. Lieb. *Physics as Natural Philosophy: Essay in Honor of Laszlo Tisza on His 76th Birthday.* 1982.

[79] M. Levy. Universal variational functionals of electron densities, first-order density matrices, and natural spin-orbitals and solution of the v-representability problem. *Proc. Natl. Acad. Sci.*, 76(12):6062, 1979.

[80] U. von Barth and L. Hedin. A local exchange-correlation potential for the spin polarized case. *J. Phys. C*, 5(13):1629, 1972.

[81] A. K. Rajagopal and J. Callaway. Inhomogeneous electron gas. *Phys. Rev. B*, 7(5):1912, 1973.

[82] E. Runge and E. K. U. Gross. Density-functional theory for time-dependent systems. *Phys. Rev. Lett.*, 52(12):997, 1984.

[83] W. Kohn and L. J. Sham. Self-consistent equations including exchange and correlation effects. *Phys. Rev.*, 140(4A):A1133, 1965.

[84] D. M. Ceperley and B. J. Alder. Ground state of the electron gas by a stochastic method. *Phys. Rev. Lett.*, 45(7):566, 1980.

[85] C. J. Slater. *The Self-Consistent Field for Molecular and Solids*, volume 4 of *Quantum Theory of Molecular and Solids.* McGraw-Hill, New York, 1974.

[86] S. H. Vosko, L. Wilk, and M. Nusair. Accurate spin-dependent electron liquid correlation energies for local spin density calculations: a critical analysis. *Can. J. Phys.*, 58(8):1200, 1980.

[87] J. P. Perdew and S. Kurth. *A Primer in Density Functional Theory.* Springer, Berlin, 2003.

[88] S. K"ummel and L. Kronik. Orbital-dependent density functionals: Theory and applications. *Rev. Mod. Phys.*, 80:3, 2008.

[89] J. P. Perdew, K. Burke, and M. Ernzerhof. Generalized gradient approximation made simple. *Phys. Rev. Lett.*, 77(18):3865, 1996.

[90] A. D. Becke. Density-functional exchange-energy approximation with correct asymptotic behavior. *Phys. Rev. A*, 38(6):3098, 1988.

[91] C. Lee, W. Yang, and R. G. Parr. Development of the colle-salvetti correlation-energy formula into a functional of the electron density. *Phys. Rev. B*, 37(2):785, 1988.

[92] J. P. Perdew, A. Ruzsinszky, J. Tao, V. N. Staroverov, G. E. Scuseria, and G. I. Csonka. Prescription for the design and selection of density functional approximations: More constraint satisfaction with fewer fits. *J. Chem. Phys.*, 123(6):062201, 2005.

[93] V. Sahni, J. Gruenebaum, and J. P. Perdew. Study of the density-gradient expansion for the exchange energy. *Phys. Rev. B*, 26(8):4371, 1982.

[94] T. Grabo, T. Kreibich, and E. Gross. Optimized effective potential for atoms and molecules. *Molecular Engineering*, 7:27, 1997.

[95] A. D. Becke. A new mixing of hartree-fock and local density-functional theories. *J. Chem. Phys.*, 98(2):1372, 1993.

[96] A. D. Becke. Density-functional thermochemistry. III. the role of exact exchange. *J. Chem. Phys.*, 98(7):5648, 1993.

[97] C. Adamo and V. Barone. Toward reliable density functional methods without adjustable parameters: The pbe0 model. *J. Chem. Phys.*, 110(13):6158, 1999.

[98] M. Ernzerhof and G. E. Scuseria. Assessment of the Perdew–Burke–Ernzerhof exchange-correlation functional. *J. Chem. Phys.*, 110(11):5029, 1999.

[99] J. Heyd, G. E. Scuseria, and M. Ernzerhof. Hybrid functionals based on a screened Coulomb potential. *J. Chem. Phys.*, 118(18):8207, 2003.

[100] P. J. Stephens, F. J. Devlin, C. F. Chabalowski, and M. J. Frisch. Ab initio calculation of vibrational absorption and circular dichroism spectra using density functional force fields. *J. Phys. Chem.*, 98(45):11623, 1994.

[101] A. D. Becke. Density-functional thermochemistry. IV. a new dynamical correlation functional and implications for exact-exchange mixing. *J. Chem. Phys.*, 104(3):1040, 1996.

[102] A. Seidl, A. Görling, P. Vogl, J. A. Majewski, and M. Levy. Generalized Kohn-Sham schemes and the band-gap problem. *Phys. Rev. B*, 53(7):3764, 1996.

[103] P. J. Hay, R. L. Martin, J. Uddin, and G. E. Scuseria. Theoretical study of CeO_2 and Ce_2O_3 using a screened hybrid density functional. *J. Chem. Phys.*, 125(3):034712, 2006.

[104] I. de P. R. Moreira, F. Illas, and R. L. Martin. Effect of fock exchange on the electronic structure and magnetic coupling in nio. *Phys. Rev. B*, 65:155102, 2002.

[105] V. I. Anisimov, J. Zaanen, and O. K. Andersen. Band theory and Mott insulators: Hubbard U instead of stoner *I*. *Phys. Rev. B*, 44:943, 1991.

[106] V. I. Anisimov, I. V. Solovyev, M. A. Korotin, M. T. Czyżyk, and G. A. Sawatzky. Density-functional theory and nio photoemission spectra. *Phys. Rev. B*, 48:16929, 1993.

[107] A. I. Liechtenstein, V. I. Anisimov, and J. Zaanen. Density-functional theory and strong interactions: Orbital ordering in Mott-Hubbard insulators. *Phys. Rev. B*, 52:R5467, 1995.

[108] V. I. Anisimov, F. Aryasetiawan, and A. I. Lichtensteinb. First-principles calculations of the electronic structure and spectra of strongly correlated systems: the LDA+U method. *J. Phys. Condens. Matter*, 9(4):767, 1997.

[109] M. Levy, J. P. Perdew, and V. Sahni. Exact differential equation for the density and ionization energy of a many-particle system. *Phys. Rev. A*, 30:2745, 1984.

[110] A. Görling. Density-functional theory for excited states. *Phys. Rev. A*, 54:3912, 1996.

[111] J. F. Janak. Proof that $\frac{\partial e}{\partial n_i} = \epsilon$ in density-functional theory. *Phys. Rev. B*, 18:7165, 1978.

[112] T. Körzdörfer, S. Kümmel, N. Marom, and L. Kronik. When to trust photoelectron spectra from Kohn-Sham eigenvalues: The case of organic semiconductors. *Phys. Rev. B*, 79(20):201205, 2009.

[113] T. Körzdörfer and S. Kümmel. Single-particle and quasiparticle interpretation of Kohn-Sham and generalized Kohn-Sham eigenvalues for hybrid functionals. *Phys. Rev. B*, 82(15):155206, 2010.

[114] T. Körzdörfer. On the relation between orbital-localization and self-interaction errors in the density functional theory treatment of organic semiconductors. *J. Chem. Phys.*, 134:094111, 2011.

[115] G. Stefanucci and S. Kurth. Towards a description of the Kondo effect using time-dependent density-functional theory. *Phys. Rev. Lett.*, 107:216401, 2011.

[116] J. P. Bergfield, Z.-F. Liu, K. Burke, and C. A. Stafford. Bethe ansatz approach to the Kondo effect within density-functional theory. *Phys. Rev. Lett.*, 108:066801, 2012.

[117] F. Evers and P. Schmitteckert. Broadening of the derivative discontinuity in density functional theory. *Phys. Chem. Chem. Phys.*, 13:14417–14420, 2011.

[118] E. N. Economou. *Green's Functions in Quantum Physics*. Springer, Berlin, Heidelberg, 2006.

[119] K. S. Thygesen. Electron transport through an interacting region: The case of a nonorthogonal basis set. *Phys. Rev. B*, 73:035309, 2006.

[120] P. Phillips. *Advanced Solid State Physics*. Cambridge University Press, 2 edition, 2012.

[121] P. Coleman. *Introduction to Many-Body Physics*. Cambridge University Press, 2015.

[122] R. Baer and D. Neuhauser. Many-body scattering formalism of quantum molecular conductance. *Chem. Phys. Lett.*, 374(5–6):459, 2003.

[123] R. Baer, T. Seideman, S. Ilani, and D. Neuhauser. Ab initio study of the alternating current impedance of a molecular junction. *J. Chem. Phys.*, 120(7):3387, 2004.

[124] J. Taylor, H. Guo, and J. Wang. Ab initio modeling of quantum transport properties of molecular electronic devices. *Phys. Rev. B*, 63(24):245407, 2001.

[125] M. Brandbyge, J.-L. Mozos, P. Ordejón, J. Taylor, and K. Stokbro. Density-functional method for nonequilibrium electron transport. *Phys. Rev. B*, 65(16):165401, 2002.

[126] S.-H. Ke, H. U. Baranger, and W. Yang. Models of electrodes and contacts in molecular electronics. *J. Chem. Phys.*, 123(11):114701, 2005.

[127] D. Jacob and J. J. Palacios. Critical comparison of electrode models in density functional theory based quantum transport calculations. *J. Chem. Phys.*, 134(4):044118, 2011.

[128] A. R. Rocha, V. M. García-Suárez, S. Bailey, C. Lambert, J. Ferrer, and S. Sanvito. Spin and molecular electronics in atomically generated orbital landscapes. *Phys. Rev. B*, 73:085414, 2006.

[129] H. A. Bethe. Statistical theory of superlattices. *Proc. Roy. Soc. London A: Math. Phys. Eng. Sci.*, 150(871):552, 1935.

[130] J. J. Palacios, A. J. Pérez-Jiménez, E. Louis, and J. A. Vergés. Fullerene-based molecular nanobridges: A first-principles study. *Phys. Rev. B*, 64:115411, 2001.

[131] J. J. Palacios, A. J. Pérez-Jiménez, E. Louis, E. SanFabián, and J. A. Vergés. First-principles approach to electrical transport in atomic-scale nanostructures. *Phys. Rev. B*, 66:035322, 2002.

[132] D. A. Papaconstantopoulos. *Handbook of the band structure of elemental solids.* New York: Plenum Press, 1986.

[133] R. Landauer. Spatial variation of currents and fields due to localized scatterers in metallic conduction. *IBM J. Res. Develop.*, 1(3):223, 1957.

[134] R. Landauer. Electrical resistance of disordered one-dimensional lattices. *Philos. Mag.*, 21(172):863, 1970.

[135] M. Büttiker. Four-terminal phase-coherent conductance. *Phys. Rev. Lett.*, 57:1761, 1986.

[136] M. Di Ventra. *Electrical Transport in Nanoscale Systems.* UK: Cambridge University Press, 2008.

[137] D. Jacob. *Spin Transport in Nanocontacts and Nanowires.* PhD thesis, Universidad de Alicante, 2007.

[138] C. Caroli, R. Combescot, D. Lederer, P. Nozieres, and D. Saint-James. A direct calculation of the tunnelling current. ii. free electron description. *J. Phys. C: Solid State Phys.*, 4(16):2598, 1971.

[139] Y. Meir and N. S. Wingreen. Landauer formula for the current through an interacting electron region. *Phys. Rev. Lett.*, 68:2512, 1992.

[140] J. H. de Boer and E. J. W. Verwey. Semi-conductors with partially and with completely filled 3 d -lattice bands. *Proc. Phys. Soc.*, 49(4S):59, 1937.

[141] C. Zener. Interaction between the d-shells in the transition metals. ii. ferromagnetic compounds of manganese with perovskite structure. *Phys. Rev.*, 82:403, 1951.

[142] J. Friedel. Metallic alloys. *Il Nuovo Cimento (1955-1965)*, 7(2):287, 1958.

[143] P. W. Anderson. Localized magnetic states in metals. *Phys. Rev.*, 124:41, 1961.

[144] A. Hewson. *The Kondo Problem to Heavy Fermions.* Cambridge University Press, Cambridge, 1997.

[145] J. R. Schrieffer and P. A. Wolff. Relation between the Anderson and Kondo hamiltonians. *Phys. Rev.*, 149:491, 1966.

[146] S. M. Cronenwett, T. H. Oosterkamp, and L. P. Kouwenhoven. A tunable Kondo effect in quantum dots. *Science*, 281(5376):540, 1998.

[147] L. H. Yu and D. Natelson. The Kondo effect in c60 single-molecule transistors. *Nano Lett.*, 4(1):79, 2004.

[148] M. Karolak, G. Ulm, T. Wehling, V. Mazurenko, A. Poteryaev, and A. Lichtenstein. Double counting in {LDA} + dmft—the example of nio. *J. Elec. Spec. Rel. Phen.*, 181(1):11, 2010. Proceedings of International Workshop on Strong Correlations and Angle-Resolved Photoemission Spectroscopy 2009.

[149] M. T. Czyżyk and G. A. Sawatzky. Local-density functional and on-site correlations: The electronic structure of la_2cuo_4 and $lacuo_3$. *Phys. Rev. B*, 49:14211, 1994.

[150] D. Jacob, M. Soriano, and J. J. Palacios. Kondo effect and spin quenching in high-spin molecules on metal substrates. *Phys. Rev. B*, 88:134417, 2013.

[151] K. G. Wilson. The renormalization group: Critical phenomena and the Kondo problem. *Rev. Mod. Phys.*, 47:773, 1975.

[152] R. Bulla, T. A. Costi, and T. Pruschke. Numerical renormalization group method for quantum impurity systems. *Rev. Mod. Phys.*, 80:395, 2008.

[153] N. Kawakami and A. Okiji. Exact expression of the ground-state energy for the symmetric Anderson model. *Phys. Lett. A*, 86(9):483, 1981.

[154] P. Wiegmann. Towards an exact solution of the Anderson model. *Phys. Lett. A*, 80(2):163, 1980.

[155] P. B. Vigman. Exact solution of s-d exchange model at T = 0. *ZhETF Pisma Redaktsiiu*, 31:392, 1980.

[156] N. Andrei. Diagonalization of the Kondo hamiltonian. *Phys. Rev. Lett.*, 45:379, 1980.

[157] E. Gull, A. J. Millis, A. I. Lichtenstein, A. N. Rubtsov, M. Troyer, and P. Werner. Continuous-time monte carlo methods for quantum impurity models. *Rev. Mod. Phys.*, 83:349, 2011.

[158] M. Caffarel and W. Krauth. Exact diagonalization approach to correlated fermions in infinite dimensions: Mott transition and superconductivity. *Phys. Rev. Lett.*, 72:1545, 1994.

[159] A. Liebsch and H. Ishida. Temperature and bath size in exact diagonalization dynamical mean field theory. *J. Phys. Condens. Matter*, 24(5):053201, 2012.

[160] H. Ishida and A. Liebsch. Coulomb blockade and Kondo effect in the electronic structure of Hubbard molecules connected to metallic leads: A finite-temperature exact-diagonalization study. *Phys. Rev. B*, 86:205115, 2012.

[161] M. Granath and H. U. R. Strand. Distributional exact diagonalization formalism for quantum impurity models. *Phys. Rev. B*, 86:115111, 2012.

[162] S. Motahari, R. Requist, and D. Jacob. Kondo physics of the Anderson impurity model by distributional exact diagonalization. *Phys. Rev. B*, 94:235133, 2016.

[163] K. Haule, S. Kirchner, J. Kroha, and P. Wölfle. Anderson impurity model at finite Coulomb interaction u: Generalized noncrossing approximation. *Phys. Rev. B*, 64:155111, 2001.

[164] N. Grewe and H. Keiter. Diagrammatic approach to the intermediate-valence compounds. *Phys. Rev. B*, 24:4420, 1981.

[165] P. Coleman. New approach to the mixed-valence problem. *Phys. Rev. B*, 29:3035, 1984.

[166] D. Jacob, K. Haule, and G. Kotliar. Dynamical mean-field theory for molecular electronics: Electronic structure and transport properties. *Phys. Rev. B*, 82:195115, 2010.

[167] T. Pruschke and N. Grewe. The Anderson model with finite Coulomb repulsion. *Z. Phys. B*, 74(4):439, 1989.

[168] T. A. Costi, J. Kroha, and P. Wölfle. Spectral properties of the Anderson impurity model: Comparison of numerical-renormalization-group and noncrossing-approximation results. *Phys. Rev. B*, 53:1850, 1996.

[169] V. Vildosola, L. V. Pourovskii, L. O. Manuel, and P. Roura-Bas. Reliability of the one-crossing approximation in describing the Mott transition. *J. Phys. Condens. Matter*, 27(48):485602, 2015.

[170] A. Rüegg, E. Gull, G. A. Fiete, and A. J. Millis. Sum rule violation in self-consistent hybridization expansions. *Phys. Rev. B*, 87:075124, 2013.

[171] D. Jacob, K. Haule, and G. Kotliar. Kondo effect and conductance of nanocontacts with magnetic impurities. *Phys. Rev. Lett.*, 103:016803, 2009.

[172] Y. Meir, N. S. Wingreen, and P. A. Lee. Low-temperature transport through a quantum dot: The Anderson model out of equilibrium. *Phys. Rev. Lett.*, 70:2601, 1993.

[173] N. S. Wingreen and Y. Meir. Anderson model out of equilibrium: Noncrossing-approximation approach to transport through a quantum dot. *Phys. Rev. B*, 49:11040, 1994.

[174] G. Cohen, E. Gull, D. R. Reichman, and A. J. Millis. Green's functions from real-time bold-line Monte Carlo calculations: Spectral properties of the nonequilibrium Anderson impurity model. *Phys. Rev. Lett.*, 112:146802, 2014.

[175] M. Plihal and J. W. Gadzuk. Nonequilibrium theory of scanning tunneling spectroscopy via adsorbate resonances: Nonmagnetic and Kondo impurities. *Phys. Rev. B*, 63:085404, 2001.

[176] V. Madhavan, W. Chen, T. Jamneala, M. F. Crommie, and N. S. Wingreen. Local spectroscopy of a Kondo impurity: Co on au(111). *Phys. Rev. B*, 64:165412, 2001.

[177] O. Újsághy, J. Kroha, L. Szunyogh, and A. Zawadowski. Theory of the Fano resonance in the stm tunneling density of states due to a single Kondo impurity. *Phys. Rev. Lett.*, 85:2557, 2000.

[178] A. Schiller and S. Hershfield. Theory of scanning tunneling spectroscopy of a magnetic adatom on a metallic surface. *Phys. Rev. B*, 61:9036, 2000.

[179] S. Frank and D. Jacob. Orbital signatures of Fano-Kondo line shapes in stm adatom spectroscopy. *Phys. Rev. B*, 92:235127, 2015.

[180] U. Fano. Effects of configuration interaction on intensities and phase shifts. *Phys. Rev.*, 124:1866, 1961.

[181] H. O. Frota and L. N. Oliveira. Photoemission spectroscopy for the spin-degenerate Anderson model. *Phys. Rev. B*, 33:7871, 1986.

[182] H. O. Frota. Shape of the Kondo resonance. *Phys. Rev. B*, 45:1096, 1992.

[183] H. Prüser, M. Wenderoth, P. E. Dargel, A. Weismann, R. Peters, T. Pruschke, and R. G. Ulbrich. Long-range Kondo signature of a single magnetic impurity. *Nat Phys*, 7(3):203, 2011.

[184] H. Prüser, M. Wenderoth, A. Weismann, and R. G. Ulbrich. Mapping itinerant electrons around Kondo impurities. *Phys. Rev. Lett.*, 108:166604, 2012.

[185] W. J. Hehre, R. F. Stewart, and J. A. Pople. Self-consistent molecular-orbital methods. i. use of gaussian expansions of slater-type atomic orbitals. *J. Chem. Phys.*, 51(6):2657, 1969.

[186] J. B. Collins, P. von R. Schleyer, J. S. Binkley, and J. A. Pople. Self-consistent molecular orbital methods. xvii. geometries and binding energies of second-row molecules. a comparison of three basis sets. *J. Chem. Phys.*, 64(12):5142, 1976.

[187] P. J. Hay and W. R. Wadt. Ab initio effective core potentials for molecular calculations. potentials for the transition metal atoms sc to hg. *J. Chem. Phys.*, 82(1):270, 1985.

[188] W. R. Wadt and P. J. Hay. Ab initio effective core potentials for molecular calculations. potentials for main group elements na to bi. *J. Chem. Phys.*, 82(1):284, 1985.

[189] P. J. Hay and W. R. Wadt. Ab initio effective core potentials for molecular calculations. potentials for k to au including the outermost core orbitals. *J. Chem. Phys.*, 82(1):299, 1985.

[190] N. D. Lang and A. R. Williams. Core holes in chemisorbed atoms. *Phys. Rev. B*, 16:2408, 1977.

[191] L. Hedin and A. Johansson. Polarization corrections to core levels. *J. Phys. B*, 2(12):1336, 1969.

[192] S. Massidda, R. Resta, M. Posternak, and A. Baldereschi. Polarization and dynamical charge of zno within different one-particle schemes. *Phys. Rev. B*, 52:R16977, 1995.

[193] F. Aryasetiawan and O. Gunnarsson. 3*d*. *Phys. Rev. B*, 54:17564, 1996.

[194] More specifically, we obtain 1.80 ev for the z^2-orbital, 1.78 ev for the xz- and yz-orbitals, 1.81 ev for the $x^2 - y^2$-orbital and 2.59 ev for the xy-orbital.

[195] The background is calculated by calculating the transmission function without adding the self-energy but pushing the respective d level away from the fermi level.

[196] H. G. Luo, T. Xiang, X. Q. Wang, Z. B. Su, and L. Yu. Fano resonance for Anderson impurity systems. *Phys. Rev. Lett.*, 92:256602, 2004.

[197] R. Žitko and T. Pruschke. Many-particle effects in adsorbed magnetic atoms with easy-axis anisotropy: the case of fe on the cun/cu(100) surface. *New J. Phys.*, 12(6):063040, 2010.

[198] M. F. Crommie, C. P. Lutz, and D. M. Eigler. Imaging standing waves in a two-dimensional electron gas. *Nature*, 363(6429):524, 1993.

[199] A. Bogicevic, S. Ovesson, P. Hyldgaard, B. I. Lundqvist, H. Brune, and D. R. Jennison. Nature, strength, and consequences of indirect adsorbate interactions on metals. *Phys. Rev. Lett.*, 85:1910, 2000.

[200] O. Jeandupeux, L. Bürgi, A. Hirstein, H. Brune, and K. Kern. Thermal damping of quantum interference patterns of surface-state electrons. *Phys. Rev. B*, 59:15926, 1999.

[201] J. Kügel, M. Karolak, J. Senkpiel, P.-J. Hsu, G. Sangiovanni, and M. Bode. Relevance of hybridization and filling of 3d orbitals for the Kondo effect in transition metal phthalocyanines. *Nano Lett.*, 14(7):3895, 2014.

[202] S. Karan, D. Jacob, M. Karolak, C. Hamann, Y. Wang, A. Weismann, A. I. Lichtenstein, and R. Berndt. Shifting the voltage drop in electron transport through a single molecule. *Phys. Rev. Lett.*, 115:016802, 2015.

[203] F. Aryasetiawan, T. Miyake, and R. Sakuma. *The LDA+DMFT approach to strongly correlated materials*, volume 1 of *Schriften des Forschungszentrums Jülich : Modeling and Simulation.* 2011.

[204] J. Hubbard and B. H. Flowers. Electron correlations in narrow energy bands. *Proc. Royal Soc. Lond. A*, 276(1365):238, 1963.

[205] O. Gunnarsson, O. K. Andersen, O. Jepsen, and J. Zaanen. Density-functional calculation of the parameters in the Anderson model: Application to mn in cdte. *Phys. Rev. B*, 39:1708, 1989.

[206] W. E. Pickett, S. C. Erwin, and E. C. Ethridge. Reformulation of the LDA + u method for a local-orbital basis. *Phys. Rev. B*, 58:1201, 1998.

[207] M. Cococcioni and S. de Gironcoli. Linear response approach to the calculation of the effective interaction parameters in the LDA + U method. *Phys. Rev. B*, 71:035105, 2005.

[208] H. J. Kulik, M. Cococcioni, D. A. Scherlis, and N. Marzari. Density functional theory in transition-metal chemistry: A self-consistent Hubbard u approach. *Phys. Rev. Lett.*, 97:103001, 2006.

[209] H. J. Kulik and N. Marzari. Systematic study of first-row transition-metal diatomic molecules: A self-consistent dft+u approach. *J. Chem. Phys.*, 133(11), 2010.

[210] D. Bohm and D. Pines. A collective description of electron interactions. i. magnetic interactions. *Phys. Rev.*, 82:625, 1951.

[211] D. Pines and D. Bohm. A collective description of electron interactions: Ii. collective vs individual particle aspects of the interactions. *Phys. Rev.*, 85:338, 1952.

[212] D. Bohm and D. Pines. A collective description of electron interactions: Iii. Coulomb interactions in a degenerate electron gas. *Phys. Rev.*, 92:609, 1953.

[213] M. Gell-Mann and K. A. Brueckner. Correlation energy of an electron gas at high density. *Phys. Rev.*, 106:364, 1957.

[214] M. Springer and F. Aryasetiawan. Frequency-dependent screened interaction in ni within the random-phase approximation. *Phys. Rev. B*, 57:4364, 1998.

[215] T. Kotani. Ab initio random-phase-approximation calculation of the frequency-dependent effective interaction between 3d electrons: Ni, fe, and mno. *J. Phys. Condens. Matter*, 12(11):2413, 2000.

[216] F. Aryasetiawan, M. Imada, A. Georges, G. Kotliar, S. Biermann, and A. I. Lichtenstein. Frequency-dependent local interactions and low-energy effective models from electronic structure calculations. *Phys. Rev. B*, 70:195104, 2004.

[217] F. Aryasetiawan, K. Karlsson, O. Jepsen, and U. Schönberger. Calculations of Hubbard u from first-principles. *Phys. Rev. B*, 74:125106, 2006.

[218] T. Miyake and F. Aryasetiawan. Screened Coulomb interaction in the maximally localized Wannier basis. *Phys. Rev. B*, 77:085122, 2008.

[219] T. Miyake, F. Aryasetiawan, and M. Imada. *Ab initio* procedure for constructing effective models of correlated materials with entangled band structure. *Phys. Rev. B*, 80:155134, 2009.

[220] K. Karlsson, F. Aryasetiawan, and O. Jepsen. Method for calculating the electronic structure of correlated materials from a truly first-principles LDA $+ u$ scheme. *Phys. Rev. B*, 81:245113, 2010.

[221] E. Şaşıoğlu, C. Friedrich, and S. Blügel. Effective Coulomb interaction in transition metals from constrained random-phase approximation. *Phys. Rev. B*, 83:121101, 2011.

[222] B.-C. Shih, Y. Zhang, W. Zhang, and P. Zhang. Screened Coulomb interaction of localized electrons in solids from first principles. *Phys. Rev. B*, 85:045132, 2012.

[223] Y. Nomura, M. Kaltak, K. Nakamura, C. Taranto, S. Sakai, A. Toschi, R. Arita, K. Held, G. Kresse, and M. Imada. Effective on-site interaction for dynamical mean-field theory. *Phys. Rev. B*, 86:085117, 2012.

[224] L. Vaugier, H. Jiang, and S. Biermann. Hubbard u and hund exchange j in transition metal oxides: Screening versus localization trends from constrained random phase approximation. *Phys. Rev. B*, 86:165105, 2012.

[225] R. Sakuma and F. Aryasetiawan. First-principles calculations of dynamical screened interactions for the transition metal oxides mo (m=mn, fe, co, ni). *Phys. Rev. B*, 87:165118, 2013.

[226] B. Amadon, T. Applencourt, and F. Bruneval. Screened Coulomb interaction calculations: crpa implementation and applications to dynamical screening and self-consistency in uranium dioxide and cerium. *Phys. Rev. B*, 89:125110, 2014.

[227] D. D. O'Regan, M. C. Payne, and A. A. Mostofi. Subspace representations in ab initio methods for strongly correlated systems. *Phys. Rev. B*, 83:245124, 2011.

[228] M. Soriano and J. J. Palacios. Theory of projections with nonorthogonal basis sets: Partitioning techniques and effective hamiltonians. *Phys. Rev. B*, 90:075128, 2014.

[229] The geometries were provided by Dr. Michael Karolak by private communication.

[230] G. Kresse and J. Hafner. Ab initio molecular dynamics for liquid metals. *Phys. Rev. B*, 47:558, 1993.

[231] V. I. Anisimov, A. I. Poteryaev, M. A. Korotin, A. O. Anokhin, and G. Kotliar. First-principles calculations of the electronic structure and spectra of strongly correlated systems: dynamical mean-field theory. *J. Phys. Condens. Matter*, 9(35):7359, 1997.

[232] A. I. Lichtenstein and M. I. Katsnelson. ***Ab initio*** calculations of quasiparticle band structure in correlated systems: Lda++ approach. *Phys. Rev. B*, 57:6884, 1998.

[233] G. Kotliar, S. Y. Savrasov, K. Haule, V. S. Oudovenko, O. Parcollet, and C. A. Marianetti. Electronic structure calculations with dynamical mean-field theory. *Rev. Mod. Phys.*, 78:865, 2006.

[234] K. Held, G. Keller, V. Eyert, D. Vollhardt, and V. I. Anisimov. Mott-hubbard metal-insulator transition in paramagnetic V_2O_3: An $lda+dmft$(QMC) study. *Phys. Rev. Lett.*, 86:5345, 2001.

[235] S. Y. Savrasov, G. Kotliar, and E. Abrahams. Correlated electrons in δ-plutonium within a dynamical mean-field picture. *Nature*, 410:793, 2001.

[236] K. Held, A. K. McMahan, and R. T. Scalettar. Cerium volume collapse: Results from the merger of dynamical mean-field theory and local density approximation. *Phys. Rev. Lett.*, 87:276404, 2001.

[237] D. Jacob and G. Kotliar. Orbital selective and tunable Kondo effect of magnetic adatoms on graphene: Correlated electronic structure calculations. *Phys. Rev. B*, 82:085423, 2010.

[238] M. Karolak, D. Jacob, and A. I. Lichtenstein. Orbital Kondo effect in cobalt-benzene sandwich molecules. *Phys. Rev. Lett.*, 107:146604, 2011.

[239] L. V. Pourovskii, B. Amadon, S. Biermann, and A. Georges. Self-consistency over the charge density in dynamical mean-field theory: A linear muffin-tin implementation and some physical implications. *Phys. Rev. B*, 76:235101, 2007.

[240] F. Lechermann. *DMFT: From Infinite Dimensions to Real Materials.* Verlag des Forschungszentrum Jülich, 2018.

[241] J. Minár, L. Chioncel, A. Perlov, H. Ebert, M. I. Katsnelson, and A. I. Lichtenstein. Multiple-scattering formalism for correlated systems: A kkr-dmft approach. *Phys. Rev. B*, 72:045125, 2005.

[242] H. Park, A. J. Millis, and C. A. Marianetti. Computing total energies in complex materials using charge self-consistent dft + dmft. *Phys. Rev. B*, 90:235103, 2014.

[243] F. Lechermann, A. Georges, A. Poteryaev, S. Biermann, M. Posternak, A. Yamasaki, and O. K. Andersen. Dynamical mean-field theory using Wannier functions: A flexible route to electronic structure calculations of strongly correlated materials. *Phys. Rev. B*, 74:125120, 2006.

[244] M. Aichhorn, L. Pourovskii, and A. Georges. Importance of electronic correlations for structural and magnetic properties of the iron pnictide superconductor lafeaso. *Phys. Rev. B*, 84:054529, 2011.

[245] M. Aichhorn, L. Pourovskii, V. Vildosola, M. Ferrero, O. Parcollet, T. Miyake, A. Georges, and S. Biermann. Dynamical mean-field theory within an augmented plane-wave framework: Assessing electronic correlations in the iron pnictide lafeaso. *Phys. Rev. B*, 80:085101, 2009.

[246] K. Haule, C.-H. Yee, and K. Kim. Dynamical mean-field theory within the full-potential methods: Electronic structure of ceirin$_5$, cecoin$_5$, and cerhin$_5$. *Phys. Rev. B*, 81:195107, 2010.

[247] S. Bhandary, E. Assmann, M. Aichhorn, and K. Held. Charge self-consistency in density functional theory combined with dynamical mean field theory: k-space reoccupation and orbital order. *Phys. Rev. B*, 94:155131, 2016.

[248] Note that the maximum amplitude of the Kondo peak at $T = 0$ K is only determined by the hybridization[144]; changes in the hybridization for different iterations are relatively small, however, so that this effect does not play a mayor role.

List of abbreviations

AIM	Anderson impurity model
a.u.	arbitrary units
cRPA	constrained random phase approximation
CTQMC	continuous time quantum Monte Carlo
DCC	double counting correction
DFT	density functional theory
DMFT	dynamical mean field theory
DOS	density of states
Eq.	equation
FF	Fano-Frota
Fig.	figure
FL	Fano-Lorentz
FLL	fully localized limit
GF	Green's function
GGA	generalized gradient approximation
GKS	generalized Kohn Sham
HFA	Hartree-Fock approximation
HOMO	highest occupied molecular orbital
KS	Kohn Sham
LDA	local density approximation
LSDA	local spin density approximation
mAIM	multi-orbital Anderson impurity model
NCA	none crossing approximation
OCA	one crossing approximation
OEP	optimized effective potential
PBE	Perdew-Becke-Ernzerhof functional
PP	pseudoparticle
Ref.	reference
RPA	random phase approximation
sAIM	single-orbital Anderson impurity model
sc	self-consistent
Sec.	section
STM	scanning tunneling microscopy
STS	scanning tunneling spectroscopy
SVWN	Slater-Vosko-Wilk-Nusair
Tab.	table
TDDFT	time-dependent density functional theory
ZBA	zero bias anomaly

Eidesstattliche Erklärung

Hiermit erkläre ich, dass ich meine Dissertation selbstständig und ohne fremde Hilfe verfasst und keine anderen als die von mir angegebenen Quellen und Hilfsmittel zur Erstellung meiner Dissertation verwendet habe. Den benutzten Werken wörtlich oder inhaltlich entnommene Stellen sind als solche gekennzeichnet.

Ort, Datum	Sebastian Frank

Acknowledgments

This thesis would not have been possible without a great deal of help and assistance of many individuals, who supported me in one way or another during my time in Halle.

First and foremost I would like to thank my supervisor, Dr. David Jacob, for his continuous support, inspiration, guidance and enthusiasm. Your door always stood open to me for spontaneous discussions, which were always enjoyable and enlightening.

My sincere gratitude to Prof. Dr. Eberhard Gross, for providing a great scientific environment in the theory group of the MPI, for all his support, and also for making the visit to San Sebastian during the final year of this thesis possible.

I am thankful to my colleagues at the MPI for the friendly atmosphere, intense scientific discussions, even intenser kicker matches and many delicious cakes in the kitchen. Thanks to Ina for all administrative assistance. To my officemate and fellow PhD student Sareh, thank you for the great familiar atmosphere in the office, and for the many scientific and non-scientific discussions, and also to Vika for many visits, and hilarious stories; thanks to both of you for being such great friends.

I would also like to thank my WG and all of my friends for bearing with me, particularly during the final stretches of this thesis, for moral support, funny moments and intense conversations, so I could rest my mind outside the world of research.

Finally, I want to thank my family, and most importantly my parents, for their unparalleled love, help and support, particularly during the difficult first years in Halle. You always encouraged and believed in me to find my way, by giving me the proverbial roots and wings.

Curriculum Vitae

Personal information

Name: Sebastian Frank

Date of birth: 01/01/1986

Place of birth: Eisenach, Germany

Education

June 2012 to now	PhD candidate at the Max-Planck Institute of Microstructure Physics and the Martin-Luther University Halle-Wittenberg; PhD thesis on ”The role of electronic correlations in scanning tunneling spectroscopy of adatoms”, supervised by Dr. David Jacob and Prof. Dr. E.K.U. Gross
November 2008 to November 2012	Elite Study Program Macromolecular Science at the University of Bayreuth (grade ”very good”)
September 2011 to November 2011	Internship at the UNESP in Botucatu, São Paulo, Brazil; research project on ”Modelling of proton energy-deposition in tissue”, supervised by Prof. J. Mesa Hormaza
July 2011	Diploma degree at the University of Bayreuth (grade "with distinction"); diploma thesis on ”Molecular Switching and Electronical Response”, supervised by Prof. S. Kümmel, Theoretical Physics IV
February 2009 to June 2009	Semester abroad at the University of Canterbury, Christchurch, New Zealand; research project with Prof. M.F. Reid on ”Modelling of Excited State Absorption of Lanthanide Ions in Crystals”
since October 2005	Academic studies of physics/biophysics at the University of Bayreuth, Germany
June 2004	Abitur at the Philipp-Melanchthon-Gymnasium Gerstungen (grade: 1.0)

List of publications

1. Michael F. Reid, Liusen Hu, Sebastian Frank, Chang-Kui Duan, Shangda Xia and Min Yin. Spectroscopy of High-Energy States of Lanthanide Ions. Eur. J. Inorg. Chem., 2010:2649, 2010.
2. Sebastian Frank and David Jacob. Orbital signatures of Fano-Kondo line shapes in STM adatom spectroscopy. Phys. Rev. B, 92:235127, 2015.